Investigation of Near Wake Flow Structure of a Horizontal Axis Wind Turbine Using Particle Image Velocimetry

Kevin Tom

A Thesis

in

The Department

of

Mechanical and Industrial Engineering

Faculty of Engineering and Computer Science

Presented in Partial Fulfillment of the Requirements
for the Degree of Master of Applied Science (Mechanical Engineering) at
Concordia University
Montreal, Quebec, Canada.

September 2010

CONCORDIA UNIVERSITY

School of Graduate Studies

This is to certify that the thesis prepared

By: Kevin Tom

Entitled: Investigation of Near Wake Flow Structure of a Horizontal Axis Wind Turbine Using Particle Image Velocimetry

and submitted in partial fulfillment of the requirements for the degree of

Master of Applied Science (Mechanical Engineering)

complies with the regulations of the University and meets the accepted standards with respect to originality and quality.

Signed by the final Examining Committee:

Dr. Mamoun Medraj	Chair
Dr. Samuel Li (External, BCEE)	Examiner
Dr. Wahid S. Ghaly	Examiner
Dr. Hoi Dick Ng	Co-supervisor
Dr. Kamran Siddiqui (UWO)	Co-supervisor

Approved by Dr. Martin D. Pugh
Chair of Department or Graduate Program Director

October 8, 20_10 Dr. Robin Drew
Dean of Faculty

ABSTRACT

Investigation of Near Wake Flow Structure of a Horizontal Axis Wind Turbine Using Particle Image Velocimetry

Kevin Tom

An experimental study was conducted to investigate the mean and turbulent flow characteristics in the near wake region of a model horizontal axis wind turbine (HAWT), with the rotor diameter D = 0.15 m. State-of-the-art particle image velocimetry (PIV) technique was utilized to measure two dimensional velocity fields in horizontal planes, which extended between 0.15 D upstream to 0.7 D downstream. Measurements were taken at three vertical positions (z = 0.185 m, 0.135 m, and 0.05 m) to account for wake perturbations from the blades, support tower and blades, and the tower itself. The wind speed was varied to give a tip speed ratio (λ) range of 3.5 - 4.25 and chord Reynolds number between 1900 - 2500.

A phase averaging algorithm was developed according to the rotor's angular configuration to compute various phase-averaged flow quantities. Results are presented in ensemble-averaged and phase-averaged forms. Results of phase averaged velocity deficit determined regions of accelerated flow adjacent to individual blades, and a localized region of lower momentum due to flow separation. The correlation between blade-trailing vorticity strength, and the increase in turbulence was confirmed through profiles of turbulence intensity. The profiles of Reynolds stress showed significant enhancement immediately downstream of blades and tower indicating the enhanced production of turbulent kinetic energy (TKE). The wavenumber spectra of both streamwise and crosswind velocity components were examined. The result provided the first quantitative estimate of the scales at which energy is injected into the turbulence by the blades and tower. An inertial subrange was observed at all heights, and it was determined that the tower redistributed TKE to a wider range of scales.

Acknowledgements

First and foremost, it was a great privilege to have worked under the supervision of both Dr. Kamran Siddiqui and Dr. Hoi Dick Ng. They helped me become not only a better scholar, but more importantly, to grow as an individual. The completion of this journey would not have been possible without their approval of conducting research in this field, total commitment, guidance and confidence in my abilities.

I would like to thank Dr. Nasiruddin Shaikh for his expertise and hands on experience for the duration of the experiments. A small token of appreciation to my fellow office colleague, Othman Smadi, whether it was about his CFD simulations, helpful tips about a course, or family life, always had time for interesting and insightful discussions.

I would like to extend my sincere gratitude to my parents for their unwavering support, both emotionally and financially, during these past few years. I am also grateful to my siblings, particularly my sister, Jen, who brightened my most arduous days with laughs and light hearted moments. Last but not least, a credit goes out to some of my closest friends who took the time to read passages of this thesis and provide much needed perspective.

Table of Contents

List of figures

List of tables

Nomenclature

Greek symbols

Γ	*Circulation* $[m^2\ s^{-1}]$
$\phi_{ij}(\vec{\kappa})$	*3-D wavenumber spectrum*
δ_{ij}	*Kronecker delta*
ε	*Dissipation rate* $[m^2\ s^{-3}]$
κ	*Wavenumber* $[rad\ m^{-1}]$
η	*Kolmogorov length scale [m]*
λ	*Tip speed ratio*
θ	*Phase angle*
ρ	*Density* $[kg\ m^{-3}]$
μ	*Dynamic viscosity* $[kg\ m^{-1}\ s^{-1}]$
ν	*Kinematic viscosity* $[m^2\ s^{-1}]$
ν_T	*Eddy viscosity* $[m^2\ s^{-1}]$
ζ	*Vorticity* $[s^{-1}]$
τ_η	*Kolmogorov time scale [s]*

Roman alphabet

a	*Axial induction factor*
C_P	*Performance coefficient*
C_T	*Thrust coefficient*
c	*Blade chord length [m]*
D	*Diameter [m]*
d_p	*Particle diameter [m]*
$F_{ii}(\kappa)$	*1-D wavenumber spectrum* $[m^3 s^{-2}]$
f	*Frequency* $[s^{-1}]$
I_∞	*Freestream turbulence intensity*
I_u	*Streamwise turbulence intensity*
I_v	*Crosswind turbulence intensity*

I_u^+	*Added streamwise turbulence intensity*
k	*Turbulent kinetic energy [$m^2 s^{-2}$]*
R	*Rotor radius [m]*
Re_c	*Chord Reynolds number*
$R_{ij}(r_i)$	*2-point, 1-time autocorrelation tensor*
U_∞	*Freestream velocity [$m s^{-1}$]*
$\langle U \rangle$	*Mean streamwise velocity [$m s^{-1}$]*
$\tilde{U}$	*Instantaneous velocity [$m s^{-1}$]*
u_i	*Turbulent fluctuations [$m s^{-1}$]*
$\langle -u_i u_j \rangle$	*Specific Reynolds stress [$m^2 s^{-2}$]*
V	*Crosswind Velocity [$m s^{-1}$]*

Subscripts

i, j	*Directional vectors*
∞	*Freestream value*

Chapter 1: Introduction

Presently, the ushering-in of green energy as a clean energy source to reduce society's dependence on depleting fossil fuels (i.e. crude oil, natural gas, and coal) has never been fiercer. Along with mounting concerns over the latter's negative environmental footprint, it is not surprising that renewable sources of energy are slowly gaining popularity. The ability of wind turbines, monolithic structures mated to elegantly designed airfoil blades, to convert kinetic energy in the wind into mechanical energy, in the form of shaft torque, which in turn drives the generator to produce electrical energy, is nothing short of an engineering marvel [1].

In the period beginning from 1995, when the world's concerted wind power capacity was a paltry 4844 MW, industry experts predicted that the incumbent technology would perennially expand, until 2005, by 25 percent with a 40 percent cumulative drop in cost to consumers [2]. According to EWEA's 2008 year-end report on globally operated wind turbines in service, the figure surged to 120790 MW [3], comfortably exceeding previous forecasts.

Despite the marked level of progress achieved by the wind energy sector, an area of research that continues to garner widespread attention is the behaviour in the near wake. This region normally extends between 1 to 3 rotor diameters downstream, and its importance lies with turbulence production in shaping the development of the wake deficit [4-6]. Moreover, the unsteady nature of the flow possesses implications on wind turbine design such as shelf life, power output, and noise [7]. Before proceeding with a literature review of near wake measurements, it is worthwhile to discuss core engineering disciplines that govern wake evolution: fluid mechanics and its sub branch, aerodynamics.

1.1 Treatment of a Simplified Wind Turbine Wake Using Conservation Laws

In the domain of the atmospheric boundary layer, wind turbine tip velocities, even at the large scales, are slow enough (Mach number < 0.3) to be assumed incompressible. The governing equations are continuity and Navier Stokes equations, expressed in tensor notation as,

$$\frac{\partial u_i}{\partial x_i} = 0, \tag{1.1}$$

$$\frac{\partial u_i}{\partial t} + u_j \frac{\partial u_i}{\partial x_j} = -\frac{1}{\rho}\frac{\partial p}{\partial x_i} + \nu \frac{\partial^2 u_i}{\partial x_j \partial x_j}, \tag{1.2}$$

where p is taken as a modified pressure term including an external force [8]. The analytical solution for the rotor wake can be obtained by modelling the wind turbine as a semi-porous, frictionless disc (see Figure 1.1), through a control volume (CV) analysis. Following a similar approach as Hansen [9], enforcing a reasonable assumption that the freestream (station 1) and wake (station 4) flows are steady, irrotational and inviscid, Eq. 1.2 is simplified to the well known Bernoulli's equation,

$$\frac{\partial \frac{1}{2} u_j^2}{\partial x_i} = -\frac{1}{\rho}\frac{\partial p}{\partial x_i}. \tag{1.3}$$

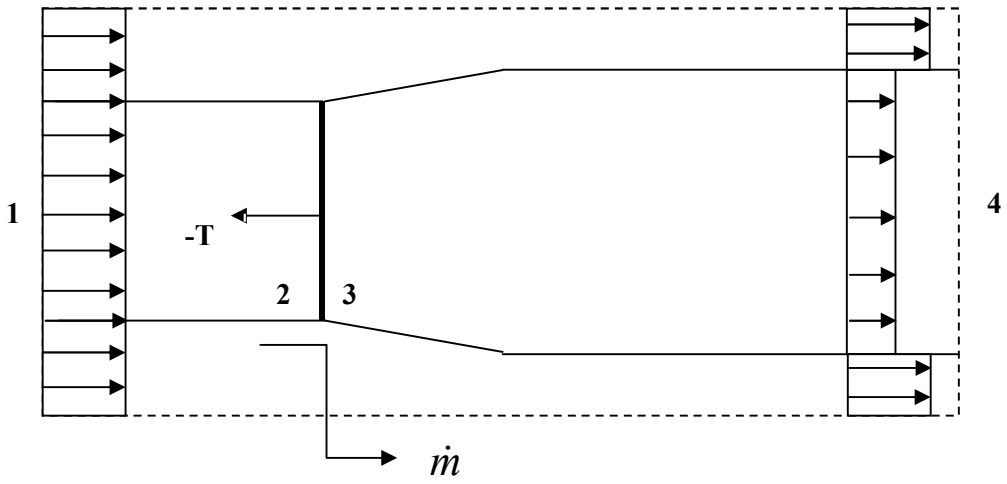

Figure 1.1: Control volume about an actuator disc.

When the oncoming flow passes through the rotor plane, it experiences both a drop in pressure and velocity, with the latter behaviour made obvious by the broadening of streamlines. To relate the rotor thrust, T, to a change in momentum inside the CV, a balance must be performed on each of the control surfaces. First, begin by invoking Eq. 1.1 to solve the mass flow rate, $\dot{m}$,

$$\dot{m} = \rho A_1 U_1 = \rho A_2 U_2 = \rho A_4 U_4 . \tag{1.4}$$

Also, U_2 (or U_3) can be related to U_1 by introducing the axial induction factor, a,

$$U_2 = U_1(1-a) , \tag{1.5}$$

which is an indication of the wake deficit and the amount of thrust generated by the rotor. Returning to the momentum balance and substituting results of Eq. 1.4, leads to the following equation [9],

$$\begin{aligned} \sum F_{ext} = -T &= -\rho A_1 U_1^2 + \rho A_4 U_4^2 , \\ T &= \rho A_4 U_4 (U_1 - U_4) . \end{aligned} \tag{1.6}$$

In order for $T = f(a)$, Eq. 1.1 is initiated between stations 3 and 4 and proceed by substituting Eq. 1.5 into Eq. 1.6 [9],

$$A_4 U_4 = A_2 U_2 , \tag{1.7 (a)}$$

$$T = \rho A_2 U_1 (U_1 - U_4)(1-a) . \tag{1.7 (b)}$$

As a matter of convenience, Eq. 1.3 is applied between stations 1-2 and 3-4 (recall that Bernoulli's equation is invalid across a rotating object [10]),

$$\frac{p_1}{\rho} + \frac{U_1^2}{2} = \frac{p_2}{\rho} + \frac{U_2^2}{2} , \tag{1.8 (a)}$$

$$\frac{p_3}{\rho} + \frac{U_3^2}{2} = \frac{p_4}{\rho} + \frac{U_4^2}{2} . \tag{1.8 (b)}$$

Upon adding the two, one arrives at a correlation relating pressure drop to U_1 and U_4 [9],

$$\Delta P_{23} = 0.5\rho(U_1^2 - U_4^2) . \tag{1.9}$$

Multiplication of Eq. 1.9 by the rotor area and equating it to Eq. 1.7 (b) renders an expression for U_4 in terms of a [9],

$$U_4 = U_1(1-2a)\,. \tag{1.10}$$

Wind turbines are typically specified by two non-dimensionalized specifications: C_T and C_P, the thrust and power (i.e. analogous to efficiency) coefficients, respectively expressed as [9],

$$C_T = \frac{T}{0.5\rho A_2 U_1^2}\,,$$

$$C_T = 4a(1-a)\,, \tag{1.11 (a)}$$

$$C_P = \frac{P_{23}}{0.5\rho A_2 U_1^3}\,,$$

$$C_P = 4a(1-a)^2\,, \tag{1.11 (b)}$$

where $P_{23} = T \cdot U_2$.

The thrust coefficient signifies the loading on commercial wind turbines. According to Magnus and Smedman [11], low C_T implies that the machine operates less effectively at high wind velocities, but more power is available, and vice versa. More importantly, a theoretical conclusion concerning C_P comes to light by solving $dC_P/da = 0$; specifically, for a = 1/3, C_P amounts to 16/27. That is, theoretically wind turbines can seize only 59.3 percent of the airstream's kinetic energy entering its plane. This impasse is universally known as Betz's law, named after Albert Betz, who first discovered the value in 1926 under the context of momentum-energy theory [2]. Although industry design codes are based on momentum theory coupled to airfoil section data, they break down during periods when the turbine operates at high loads [12], as shown in Figure 1.2. These limitations in wake models and numerical simulations of wind turbines have spurred on near-wake research involving wind tunnels to improve our understanding of its fundamental structure.

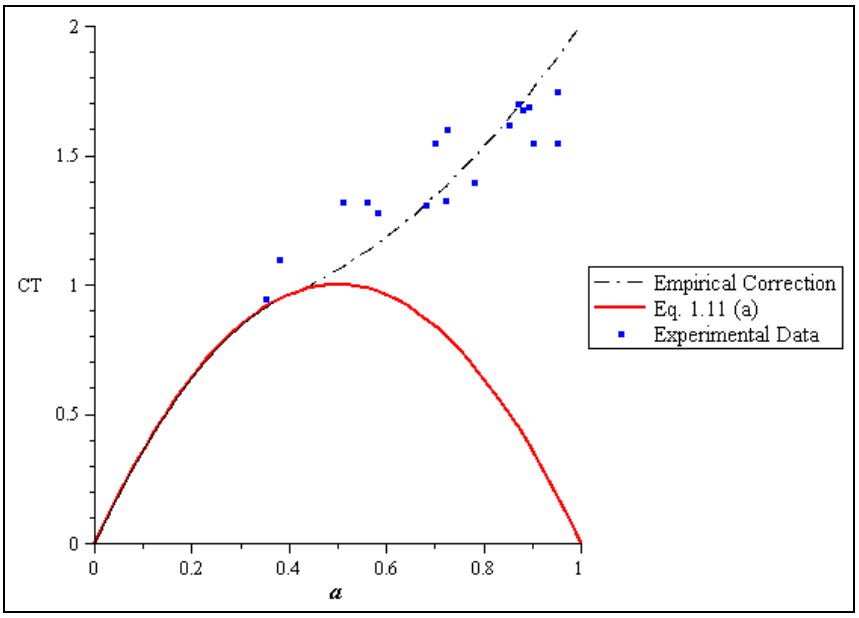

Figure 1.2: Thrust coefficient profiles as a function of axial induction factor. Eq. 1.11 (a) is modified to mend its breakdown during high axial thrust, adapted from [12].

1.2 Vortex Structure of Near-Wake Region

Aerodynamic principles that describe lift generation on wings of an aircraft transitions naturally to afford invaluable wisdom to the helical vortex-wake system generated downstream of a wind turbine, as shown in Figure 1.3. First, when the inflow with velocity, U_∞, contacts the stagnation point on the blade's bottom surface, the integrated difference in the pressure field, arising as a by-product from the Kutta condition enforced at the trailing edge, between suction (i.e. top) and pressure (i.e. bottom) surfaces, creates lift (component that produces torque) and drag forces. Secondly, the high pressure flow seeks to curl towards the suction surface at the tip, while the low pressure flow is inclined to move inboard towards the blade root. Simultaneous convective (by the incident flow) and rotational processes induce, for a lack of a better term, a "roll-up" of the just mentioned fluid behaviour into tip vortices. As the rotor gradually spins to an angular frequency, Ω, thrust imparted by the blades induces counter-rotation within the wake.

In order to unify our understanding of circulation (Γ), reference to Helmholtz's vortex theorems (suitable for inviscid, incompressible flows) and Prandtl's lifting line theory is obliged. Prandtl formulated that an aerodynamic body can be replaced by a vortex filament, with strength Γ, comprised of a stationary bound vortex and a pair of trailing tip vortices; otherwise known as a horseshoe vortex. Lift forces, per unit span, on the bound vortex may then be calculated from Kutta-Joukowski's theorem [13],

$$L = \rho U_{\infty} \Gamma \,. \tag{1.12}$$

The trailing vortices follow from Helmholtz's postulate that a vortex filament must extend to the boundaries of the fluid, or be dissipated at a solid surface (i.e. ground, airport tarmac); it cannot end in the fluid. Instead of using just one horseshoe vortex, a lift line superimposes an infinite number, each with successively weaker strengths, $d\Gamma$, to form a continuous distribution of bound circulation. Moreover, the previous discrete tip vortex pair transforms into a vorticity sheet.

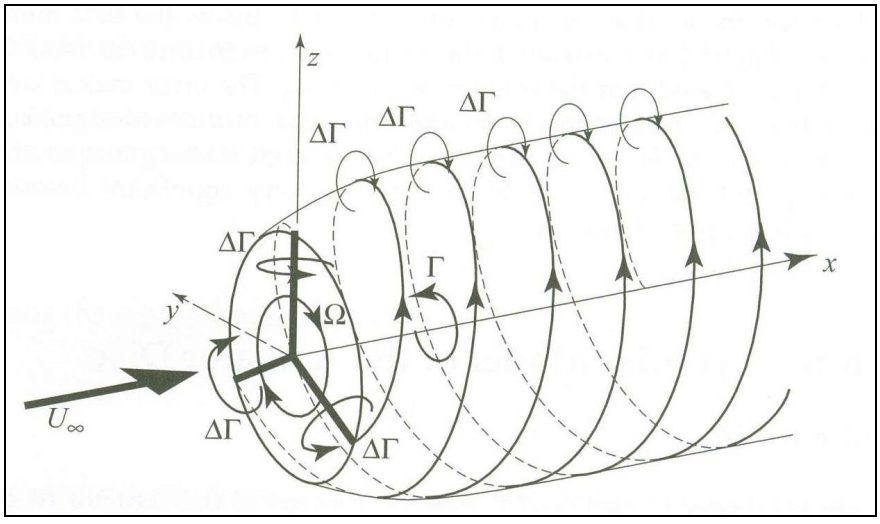

Figure 1.3: Helical vortex structure, reproduced from [14].

The manner that the wake develops downstream, including the stability and strength of the vortex system, is defined in terms of a non-dimensional parameter called tip speed ratio (λ) [15],

$$\lambda = \frac{\Omega R}{U_\infty}. \qquad 1.13$$

It is a measure of the rotor's angular velocity relative to the freestream air. A wake can fall under two states: turbulent and windmill wake states, as depicted in Figure 1.4. Within the framework of a turbulent wake (Figure 1.4 a), its occurrence is predicated on comparatively higher λ and C_T, Whale *et al* [15] state that a significant expansion of the diffused vortex sheet transpires because of an augmented blockage effect, with its boundaries outlined by a series of tip vortex cores.

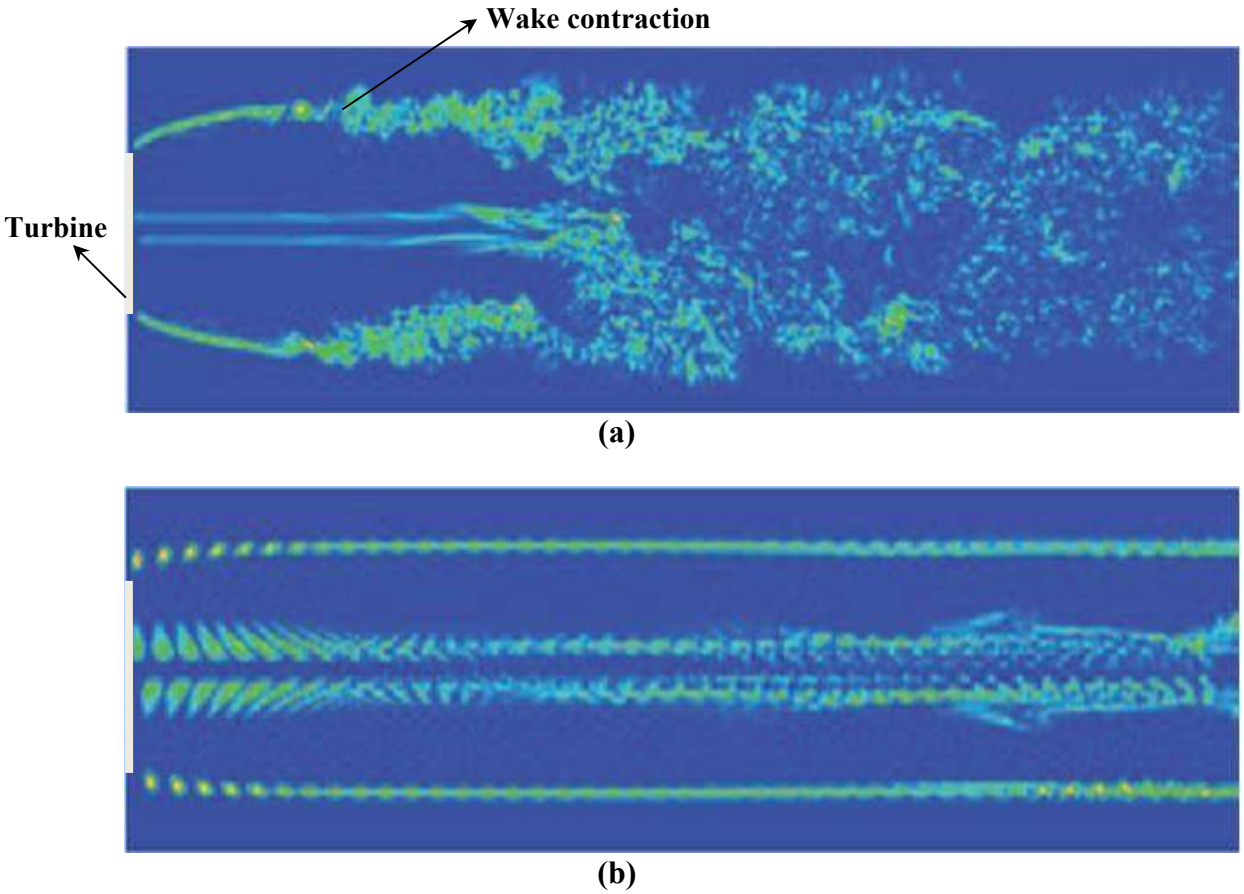

Figure 1.4: Wake development behind a wind turbine using numerical simulations; reproduced from [16]. **(a)** Turbulent wake state; λ = 11.78 **(b)** Windmill wake state; λ = 5.05.

The turbulent wake begins to contract 3-5 radii downstream of the blade due to the recovery of velocity deficit [14-17], defined as,

$$\text{Velocity Deficit} \equiv 1 - \frac{\langle U \rangle}{U_\infty}, \tag{1.14}$$

where $\langle\ \rangle$ denotes time averaging. One of the fundamental properties of turbulent flows is its tendency to enhance diffusion, or mixing. Under current circumstances, wake recovery is brought about by a transfer of momentum, as shown by the arrows in Figure 1.5. Squeezing of vorticity within the shear layer, where velocity gradients are high, causes the tip and root vortices to break down into smaller eddies [8].

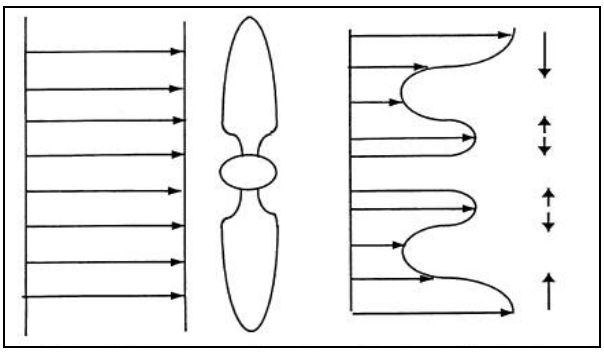

Figure 1.5: Momentum transfer towards blade midsection and hub with uniform velocity profile; from [18].

Turbines operating in proximity to their cut-out wind speed (i.e. low λ) produce a more stable wake flow downstream of the rotor plane [2]. Figure 1.4 (b) clarifies the traits associated with a windmill wake state. In clear contrast to a turbulent wake, the expansion of the boundaries is less evident and progresses uniformly rather than contract. Furthermore, tip and root vortices are expected to travel downstream in individual vortex tubes, attributed to a decrease in C_T. One variable that enumerates the level of turbulence in a flow is the turbulence intensity,

$$I_{u_i} = \frac{\left\langle u_i^2 \right\rangle^{1/2}}{U_\infty}. \tag{1.15}$$

Eq. 1.15 signifies the ratio between the root mean square (RMS) value of the velocity fluctuations to freestream velocity. Note, however, the agent that generates the turbulence in the

two wake states could not be more different. According to several studies [19, 20, 21], during periods of windmill operation, turbine blades are susceptible to deep stall due to severe angles of attack, with turbulence stemming from flow separation across the entire blade span.

1.3 Near-Wake Measurements of a Wind Turbine

A vast amount of theoretical and experimental studies to unravel the complex processes and structure of the near-wake comes in three varieties: full scale, scaled-down model rotors investigated in wind tunnels (i.e. controlled environment), and numerical simulations. The most desirable, of course, is to establish full size field measurements; however, numerous difficulties impede such endeavours such as costs, instrumentation, topography, stochastic nature of the wind, and repeatability. Available relevant discourses of the first kind are discussed, but focus is primarily centered on wind tunnel experiments of scaled-down turbines and numerical schemes.

Savino and Nyland [22], used smoke grenades to visualize the near-wake flow of a downwind (blades are attached to the nacelle behind support tower), 38 m diameter, two bladed, rotor. They observed very little wake expansion at various wind speeds, and argued that tip vortices dissipated within 2D downstream during cut-in (i.e. minimum velocity for turbine to produce power). Particle image velocimetry (PIV; explored at great length in Chapter 2) visualization experiments were carried out in a laboratory setup on a 2-bladed, model propeller by Whale and Anderson [17, 23]. The tests were conducted with λ varying from 3-12, and tip chord Reynolds number range of 6000-35000, defined as,

$$\mathrm{Re}_c = \frac{U_\infty c}{\nu}. \qquad 1.16$$

Velocity vector maps displayed a sinusoidal pattern during windmill operation, consistent with the behaviour of a helical trajectory at the wake boundaries. Moreover, vorticity contour maps

clearly identified an increase in intensity, credited to the heavily induced velocities from the rotor, as the wake transitioned into a more turbulent state.

Grant *et al* [24] focused on the extent of wake expansion behind a model turbine, consisted of 4-digit NACA series airfoils, using both PIV and a prescribed vortex panel method. Their numerical procedure predicted considerably higher growth than experimental observations (0.1R versus 0.06R), suggesting the discrepancy was caused by wall effects. Infield *et al* [25] used PIV to compute tip vortex circulation (by integrating vorticity around a closed curve) as a function of wake position. They discovered that tip vortices failed to completely roll up at specific blade positions, resulting in a steep drop in circulation. An extensive study on the tip vortex structure was performed by Grant and Parkin [26]. Their analysis, assisted by PIV, revealed several intriguing phenomena: tip vortex circulation varies as a function of phase angle, vorticity decreases as the vortex core ages (measured in turbine revolutions), and its formation is primarily and secondarily influenced by wake expansion angle and the helical vortex sheet, respectively.

Whale *et al* [20] focused on identifying scale effects on normalized, cross-wake profiles of mean velocity and turbulence intensity at similar λ numbers. PIV experiments on the 1:100 replica revealed near axisymmetric U/U_∞ curves, with minima at center which decreases with increasing λ. They observed that the turbulence intensity is highest around centerline which increases with λ. Figure 1.6 shows the discrepancies measured between full size and model rotors. Possible causes that the authors postulate are wake meandering, kinematic dissimilarity (even though tip speeds are comparable, $\mathrm{Re_c}$ is a factor of 1000 smaller), and a change in characteristic turbulence scales by terrain artifacts that are different to those formed experimentally.

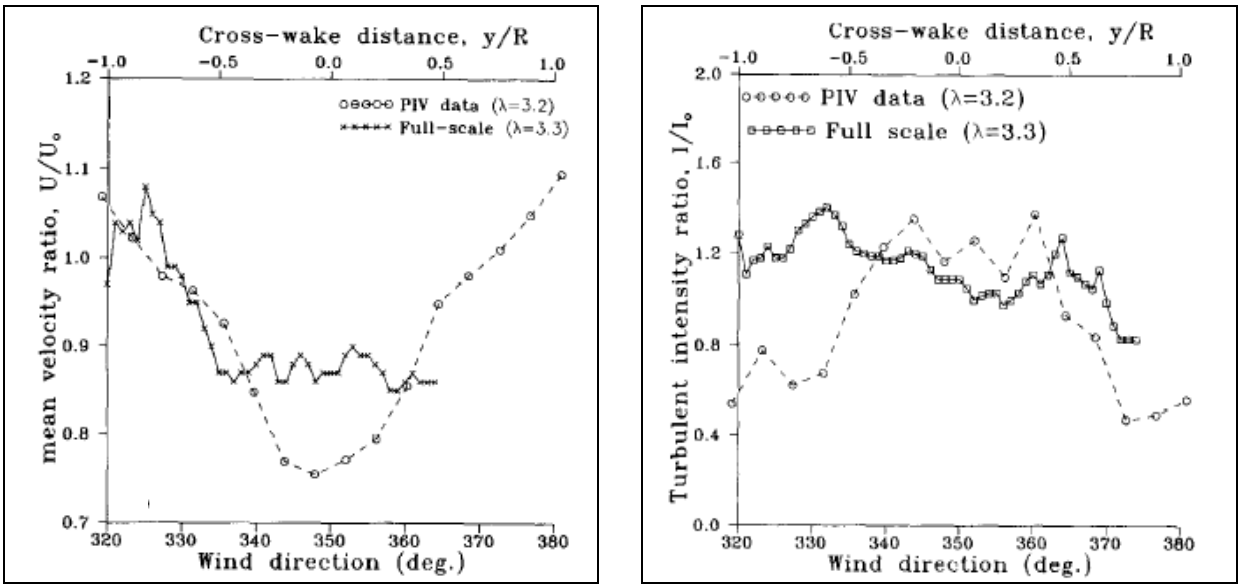

(a) **(b)**

Figure 1.6: Normalized wake profiles 1.1*D* downstream comparing full scale to model rotors, adapted from [20]. **(a)** Mean velocity **(b)** Turbulence intensity.

Hossain *et al* [27] argued that relatively thicker boundary layers, appearing in lower Re flows, influence the wake structure more profoundly. While their results at scale model reflected a greater dissipation of turbulence, their full size rotor (10:1 ratio; measuring 0.5 m in diameter) indicated a lack in separation of geometric scale.

Whale *et al* [15] tackled the issue analytically (in addition to PIV) by modelling the wake with an unsteady, inviscid (to simulate high Re condition), vortex panel method. With the exceptions of coalescing behaviour between vortices observed in PIV images and abnormally strong root vortices (i.e. viscous dissipation is absent in inviscid flow), the panel method agreed reasonably well in trends such as vorticity strength and tip vortex pitch (axial distance traversed per rotor revolution), both in terms of λ. Regrettably, their explanation of higher tip vortex pitch at scale measurements appears inconsistent with their presented data.

Phase-locked averaging (PLA), a method used in hot wire anemometry (HWA) to approximate the 3-dimensional flow field as seen by an observer attached to the reference blade,

measurements have been reported by a number of studies. The early work was by Ebert and Wood [19] who measured the three components of velocity and also computed the turbulent kinetic energy (TKE), k, about θ from 0-270 degrees at λ of 2 and 4. They observed a decrease in TKE by an order of magnitude at $\lambda = 4$, but concluded that more work would be required to explain the circumferential movement of turbulence at the said tip speed. Ebert and Wood [28] investigated in detail the hub vortex structure and argued that it may be possible to model it as a cylindrical vortex sheet. Furthermore, they corroborate similar trends in tip vortex pitch as observed in previous studies, such as [15].

PLA tangential velocities within the near-wake were investigated by Massouh and Dobrev [29]. Contrary to Figure 1.3, Figure 1.7 (a) illustrates that there are 2 distinct motions involved: Wake rotation in the same direction as the rotor is induced by the viscous drag (surfacing from the blade's boundary layer), while counter rotation is induced by the bound vortex. Periodicity of the flow stands at 120 degrees, inferred from Figure 1.7 (b), and it appears that the contribution of the viscous drag on tangential velocity is rather infrequent.

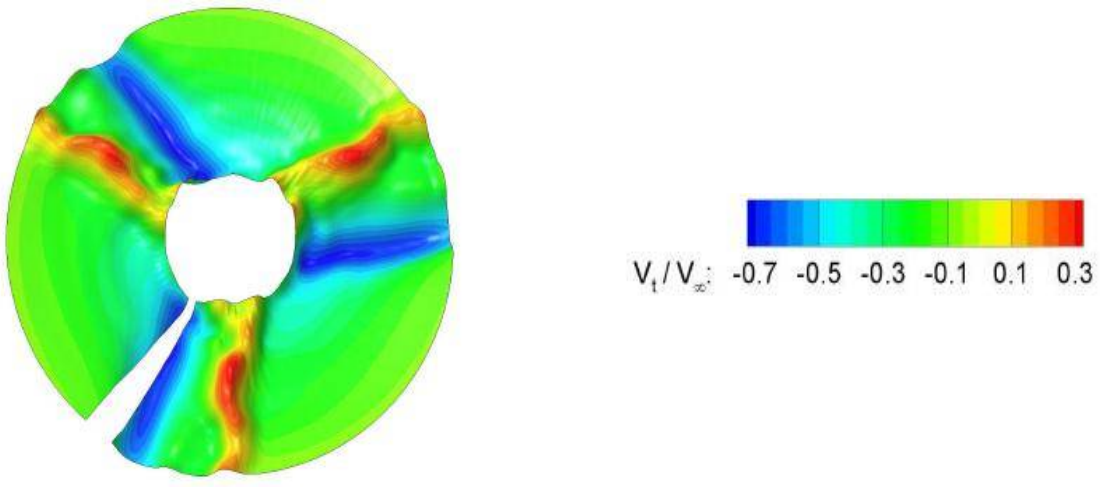

(a)

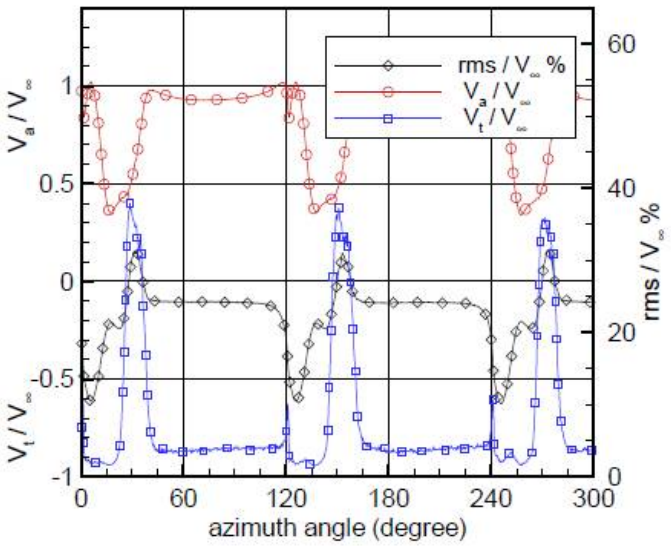

(b)

Figure 1.7: Aspects of tangential velocity in the near-wake of a 3-bladed, model wind turbine, from [29] **(a)** Contour diagram 0.02*D* downstream **(b)** PLA data 0.02*D* downstream.

1.3.1 Role of Turbulence

The essential role turbulence undertakes in the near-wake development cannot be overemphasized, as its ramifications on power generation (i.e. overestimation by up to 10 percent if ignored) and blade stresses are absolutely critical. Since turbulence is inherently random in nature, mathematical models are required to simulate flow specific processes or quantities. Moreover, statistical (such as turbulence intensity) and spectral tools are commonly employed to aid in its description.

Hot wire measurements of longitudinal turbulence intensity, specific Reynolds stress ($\langle -u_i u_j \rangle$) and TKE spectra were presented by Papaconstantinou and Bergeles [30]. In stark contrast to [20], the authors demonstrated that turbulence intensity was inversely proportional to λ with peaks at blade tip and root at several downstream positions. Similar trends were also observed by [19]. The quantity that links the mean flow to the fluctuations, through momentum

transfer, is the Reynolds stress. Portrayed graphs of $\langle -u_x u_y \rangle$ exhibited maximum amplitude at radial positions near the tip (negative peak) and root (positive peak), while zero elsewhere; unsurprising given these are regions of high shear. Referring to the frequency spectra, they determined that energy spikes occurred more often going from root to tip and at multiples of the rotor's angular frequency. As expected, the decrease in energy content further downwind is attributed to viscous dissipation.

Field measurements of turbulence include studies by Helmis *et al* [31] and Papadopoulos *et al* [32], who investigated the effects of turbine generated turbulence. The former's approach was to present trends in velocity ratios based on ambient turbulence when the turbine was either parked or running, and strove to explain the correlation between these parameters to the tower shadow (i.e. footprint of support tower on the near wake). Whereas the latter study focused on the non-diagonal elements of the Reynolds stress tensor (technically 6, but the matrix is symmetric), and deviation in frequency spectra with height and U_∞. The single shear stress term containing both transverse components reflected the least amount of momentum transfer from the outer edges of the wake due to the turbine. Careful consideration of the spectral curves substantiates one of turbulent flow theory's central paradigms: the energy cascade.

Connell [33] previously discussed the effects of a rotating frame of reference on the wind speed spectrum; chiefly, energy contained within a band of intermediate frequencies are transferred, or reallocated, to an even narrower range of higher frequencies equal to $f \cdot \lambda$. Considerable features of added turbulence intensity, Reynolds stress, and spectra were published by Chamorro and Porté-Agel [34] of a model turbine immersed in boundary layer flow. Although the local isotropy hypothesis was not explicitly accredited, the authors dealt with its

most fundamental consequence in their spectral density plots, a sample of which is rendered in Figure 1.8.

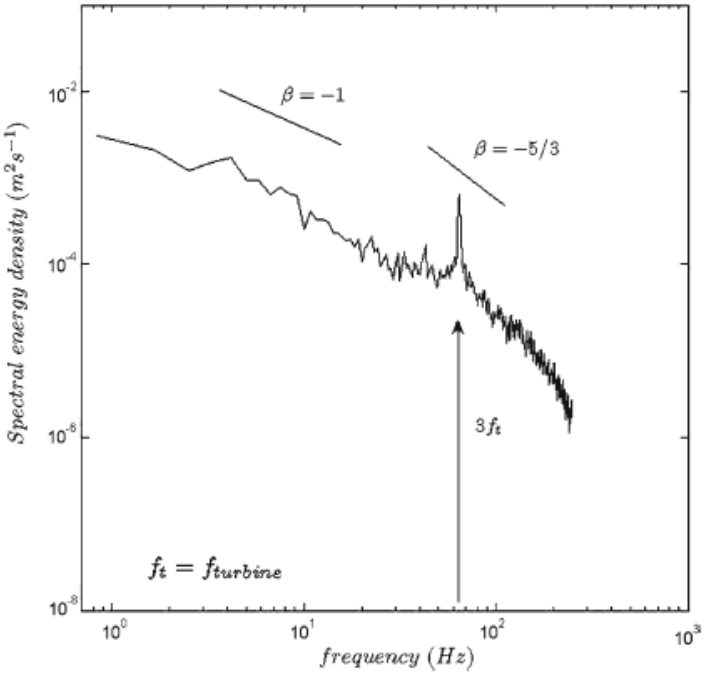

Figure 1.8: Power spectrum measured at top blade tip at 1 diameter downstream with an overlay of Kolmogorov's spectrum; reproduced from [35].

Serving as the focal point, the superimposed -5/3 slope (celebrated as the Kolmogorov -5/3 spectrum) characterizes the width of the inertial subrange, a spectrum of length scales situated between the energy containing and dissipative ranges [35]. Especially noteworthy is that the statistical motions in the inertial subrange are uniquely determined by the dissipation rate, ε, and independent of v [36]. It was further determined that this region grew with downstream distance.

As parallel computing becomes more efficient and powerful, it is only a matter of time before computational fluid dynamics (CFD) is utilized during design and implementation rather than as a validation tool. Most numerical studies fall under the latter category and involve the k-ε turbulence closure model to compare velocity deficits from field reports, such as [37, 38]. By incorporating a better physical understanding of the energy cascade, Kasmi and Masson [39]

verified turbulence intensity and velocity ratios from a number of wind turbine sites with an enhanced version of the *k-ε* model. Gómez-Elvira *et al* [40] present anisotropic relations of the Reynolds stress in order to model atmospheric turbulence effects on the wake with good agreement to other studies. Jimenez *et al* [41] studied the anisotropic turbulence using large-eddy simulation (LES). A portion of their findings on full wake added turbulence intensity, Figure 1.9 (a), is compared to an assortment of past experiments, both model and full-scale.

It can be clearly seen that the model under predicts the behaviour until the far wake, where all curves and data points converge. The correlation coefficient $\langle u_x u_z \rangle / U_\infty^2$ is displayed in Figure 1.9 (b), which corresponds to the sole horizontal plane parallel to the flow. Noted features are the symmetry despite a log-law incident flow, its close approximation to field data, and the maxima corresponding to the shear layer as previously noted in [19, 30].

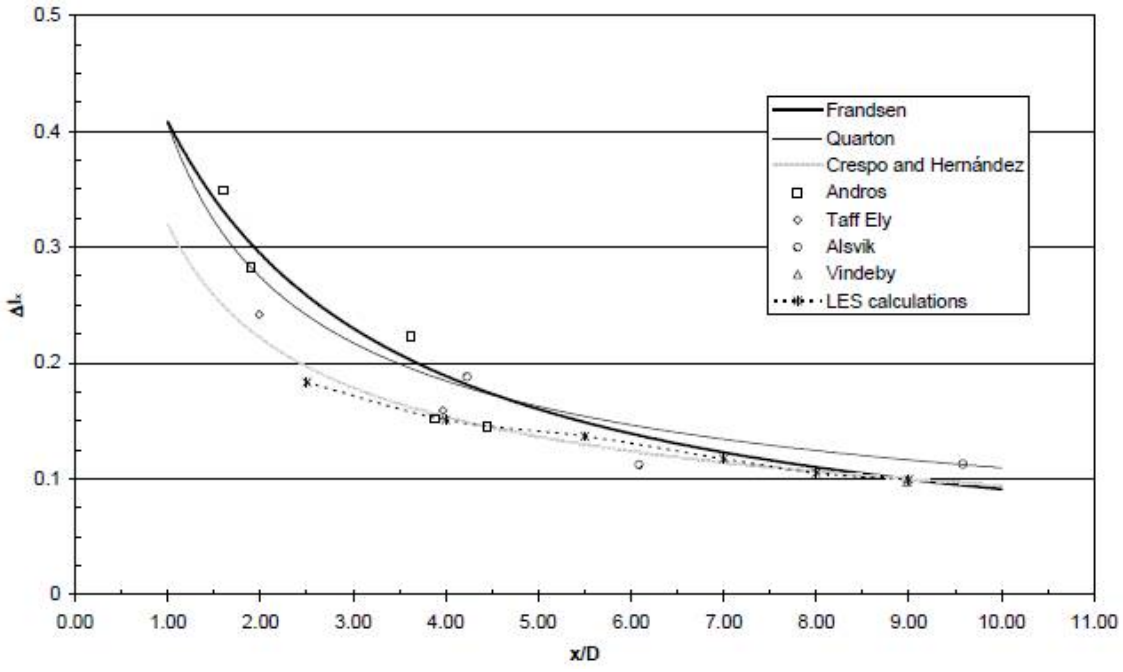

(a)

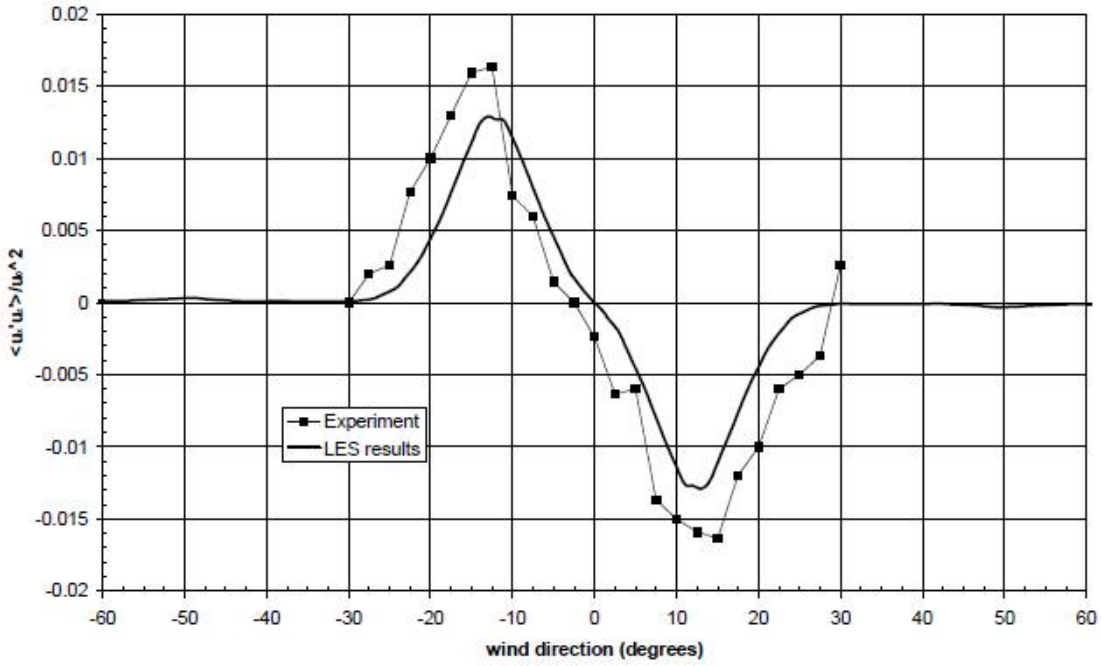

(b)

Figure 1.9: LES results from [41]. **(a)** Added turbulence intensity at hub height as a function of streamwise distance **(b)** Normalized Reynolds stress in the horizontal plane, $\langle u_x u_z \rangle / U_\infty^2$.

1.4 Motivation

One feature consistent with a rotating wind turbine is the blade-determined periodicity of the flow. Studies detailing various wake parameters as a function of phase are few and far between, relying solely on data that have been averaged over many revolutions. The deficiency with the above method is that information of the spatial structure is lost when velocities and velocity gradients are smoothed out. While experiments with phase averaging exist, the quantities investigated are limited to velocity components and TKE, as in [19, 29].

In past research, measurements of power spectra relied exclusively on hot-wire probes due to their superior temporal resolution. As such, it was convenient to display the results on a frequency scale, and observe behaviour localized around the turbine's rotation rate. However, such analyses overlook the spatial scales of turbulence, which is poorly understood in the near-

wake. This issue can be tackled effectively by examining the wavenumber spectra as a function of phase or as an ensemble average. In doing so, it is quite hopeful that further insight on the energy cascade can be extracted.

Furthermore, only three previously known studies discussed prevalent issues in the near-wake delimited by 1 diameter downstream [19, 30, 42]. It serves as an impetus to discuss this zone more deeply where turbulence intensities and production of TKE is highest. Although rotor effects are indeed of primary importance, documentation of the support tower's influence on the unsteadiness of the flow is often neglected to simplify the analysis [20, 31, 32].

1.5 Objectives

The present research is focused on the investigation of near-wake characteristics within one rotor diameter downstream of a scaled turbine in a laboratory setup using state-of-the-art, PIV technique. The endeavour is to uniquely approach both mean and turbulent flow quantities not only through ensemble averages, but as a function of phase as well. Taking into account that wavenumbers are essentially the inverse of a wavelength, an immediate application is to determine the most energetic range of turbulent eddy sizes. In the context of three horizontal measurement planes, the flow is further evaluated by considering the effect of the rotor, support tower, and a combination of both.

1.6 Layout

In chapter 2, specifications of the model wind turbine are outlined, followed by an overview of the PIV technique. This leads into the experimental setup and procedure, and then a discussion about the phase averaging method. Chapter 3 focuses on the in-plane components of mean velocity at each of the three heights. Ensemble averaged results are presented first, which are

subsequently used to compare against phase averaged data. Chapter 4 discusses a number of turbulent flow parameters as a function of phase: turbulence intensities, spanwise distribution of Reynolds stress, and axial distribution of streamwise and crosswind wavenumber spectra. Chapter 5 concludes the thesis in three stages. First, provide a general overview on the thesis contribution to near-wake research on wind turbines. Second, offer remarks on the experimental limitations and their consequences. Third, deliberate on topics that can advance the present work.

Chapter 2: Experimental Setup and Techniques

The first premise of this chapter is to provide, in a succinct manner, the handcrafted specifications of a scaled three-bladed horizontal axis wind turbine model (hereinafter referred to as HAWT). This HAWT is devoid of electrical components because this study is focused on understanding near wake fluid dynamics for which the electrical components are not very crucial as they do not play any significant role in influencing the near-wake flow behaviour. The tip speed ratios obtained during the experiments with the scale model HAWT in this study are within the same range as in the field. Sicot *et* al [43] suggests matching of the tip speed ratios between the wind turbines operating in the field and scaled rotors in the lab to be the minimum requirement for lab testing.

2.1 Design of the Wind Turbine

The scaled HAWT model employed in the present study is comprised of the following parts: a set of three wooden carved blades, turbine shaft, and cylindrical post acting as the support tower. From a visual standpoint, the model rotor is a simplified version when compared to its counterparts seen in praxis [1]: lacking are a true hub, and nacelle - motor, stator and rotor, generator, pitching mechanism, and braking system. However, the aforementioned simplifications are justified by facilitating an uninhibited, proper analysis of the complexities inherent in the rotating wake.

2.1.1 Rotor Blade

Instructions and specifications on carving a plank of wood into aerodynamic blades is provided by Piggott [44]; his procedure is met with several exceptions: birch instead of pine due to cost, scaling factor ratio of 1:15.4 (original blade length of 1150 mm) to obtain an acceptable blockage ratio (8.7%), and an altered pseudo-airfoil profile. Beginning with a stock rectangular

birch block, it is cut and sanded down to a piece having a length, width, and height of 75 mm x 10 mm x 3.33 mm, respectively.

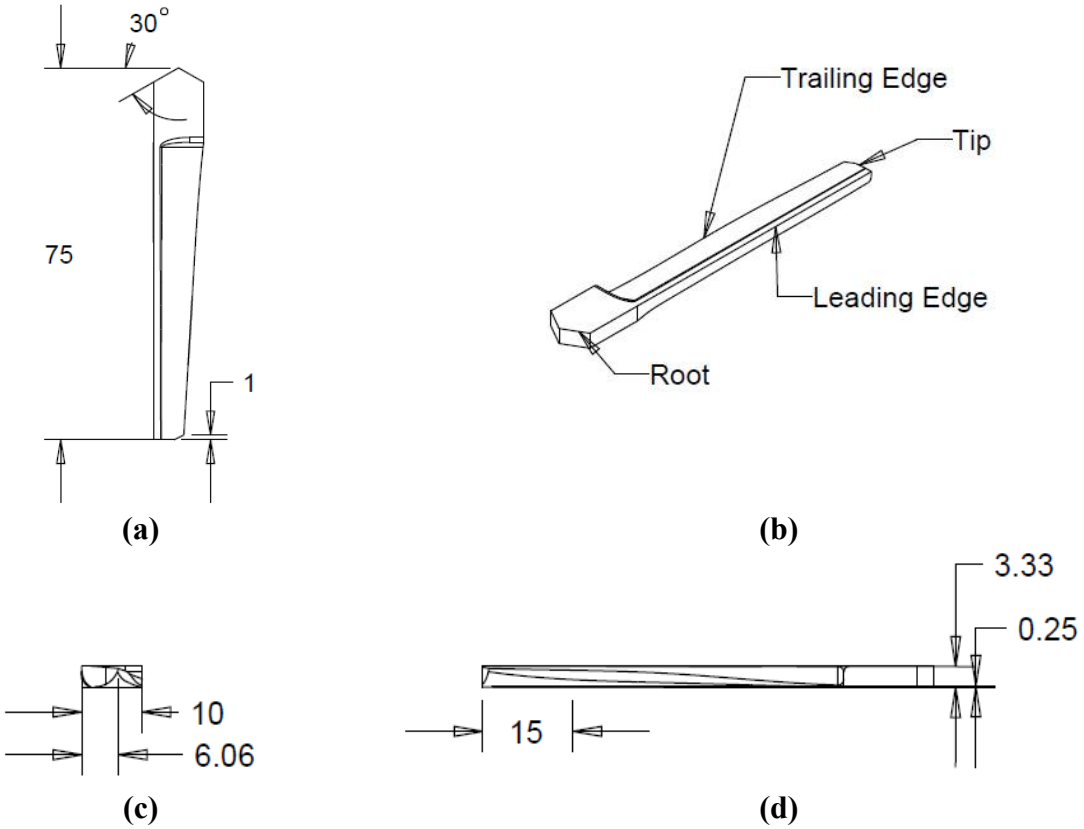

Figure 2.1: Drawing of wooden blade with measurements recorded in mm. **(a)** Top view **(b)** Isometric view **(c)** Front view **(d)** Right-side view.

Next, one of the longest sides is labelled as the trailing edge and the other as the leading edge, depicted in Figure 2.1 (b). Subsequently, illustrated in Figure 2.1 (d), the trailing edge is marked into 5 equal divisions, each measuring 15 mm. A taper ratio (defined as tip span/root span) of approximately 60 percent (see Figure 2.1 c) is applied to the trailing edge beginning from tip to the fourth division, as shown in Figure 2.1 (a). Achieving the desired twist is carefully done, using a dremel equipped with a sanding tool, by decreasing the thickness from 3.33 mm at the tip to 0.25 mm at the fourth division. The final sanding operation arrives at the airfoil profile displayed in Figure 2.2. Lastly, the 30^{o} cuts (see Figure 2.1 a) enable a set of blades to attach to one another via a strong adhesive.

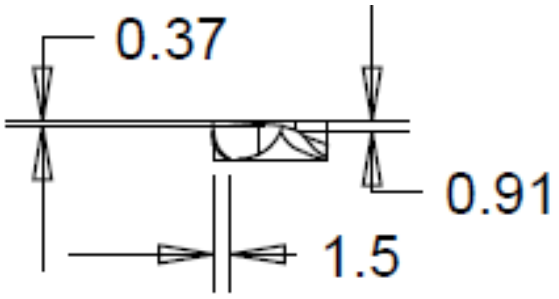

Figure 2.2: Airfoil section seen from tip.

2.1.2 The Shaft

The model turbine shaft is constructed from a stock, birch dowel rod by sawing off the necessary length. A steel washer is then mated to one end of the shortened rod providing an important service: increases the surface area on which the shaft is bonded to the rotor blade assembly. The major dimensions are demarcated in Figure 2.3 (a), with rod length measuring 36.5 mm and a diameter of 6.35 mm; the steel washer has D_{outer} = 15 mm.

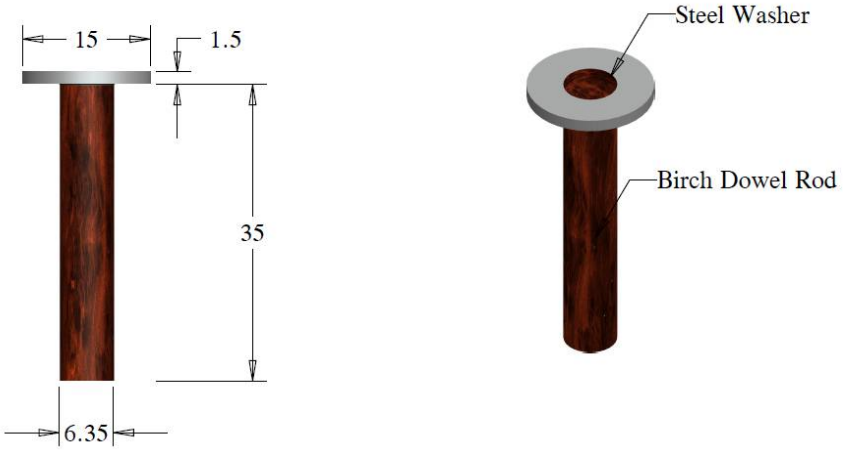

(a) **(b)**

Figure 2.3: Rotor shaft drawing with dimensions in [mm]. **(a)** Front view **(b)** Isometric view

2.1.3 The Tower

Once more, the base support anchoring the assembled blades and shaft is made of birch wood. Chosen height of the structure is equivalent to the rotor diameter, 150 mm, and stock D = 16 mm. A center hole is slowly drilled through the front face of the rod with a 6.35 mm (1/4”)

wood drill bit followed by minor sanding with the dremel, increasing the diameter by 1 mm as depicted in Figure 2.4 (b). Subsequently, a 9.525 mm (3/8”) hole is counterbored to a depth of 4 mm on each face, shown in Fig. 2.4 (a), to accommodate two RBI-168zz metal shielded bearings to eliminate the possibility of shaft-tower friction. Its major dimensions, an inner and outer diameter of 6.35 mm and 9.525 mm, respectively, are given in Figure 2.5:

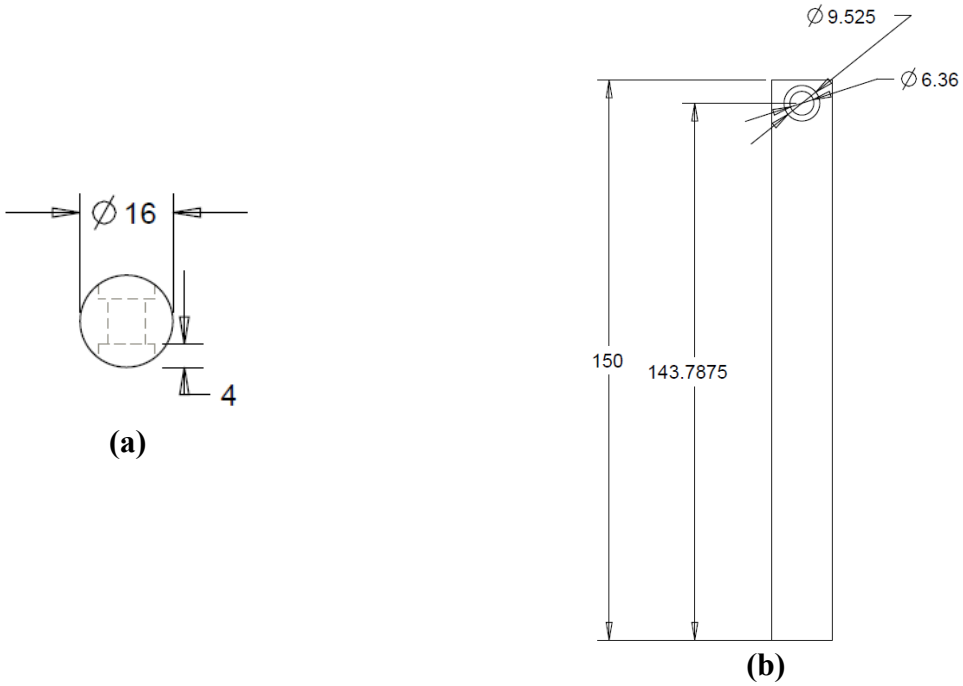

Figure 2.4: Tower drawing, measurements recorded in [mm]. **(a)** Top view **(b)** Front view

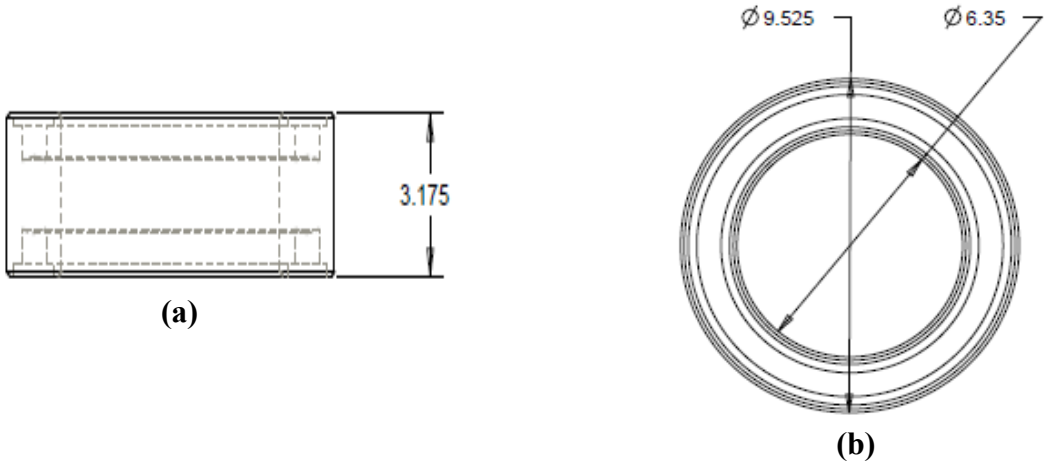

Figure 2.5: RBI-168zz metal shielded bearing drawings, measurements are in mm. **(a)** Top view **(b)** Front view.

2.2 Particle Image Velocimetry (PIV) Technique

PIV is an optical technique to remotely measure flow velocities simultaneously at many points in a plane. It has considerable advantages over point-wise measuring-devices (i.e. hot wire, Laser Doppler Velocimetry), chief amongst them being high spatial resolution of in-plane vectors [45]. This explains the reason that a wide number of experimental analyses on wind turbine wakes involve PIV [for example, 15, 17, 20, 23-27, 29, 46, 47]. A typical PIV system consists of a laser as a light source, optics to form the light sheet, a camera to acquire images, a pulse generator to control the timing of laser pulses and a computer to record and process images (see Figure 2.6). In the PIV technique, the fluid under investigation is seeded with tiny particles to accurately follow the flow. A laser pulse illuminates the measurement plane and the camera records the position of particles at that instant. A short time later, a second laser pulse illuminates the same plane again and another image of the position is recorded. The velocity field is obtained by dividing the particle displacement by the time delay between the two images. Detailed description of the tracer particles and functionality of individual components are provided in the following sections.

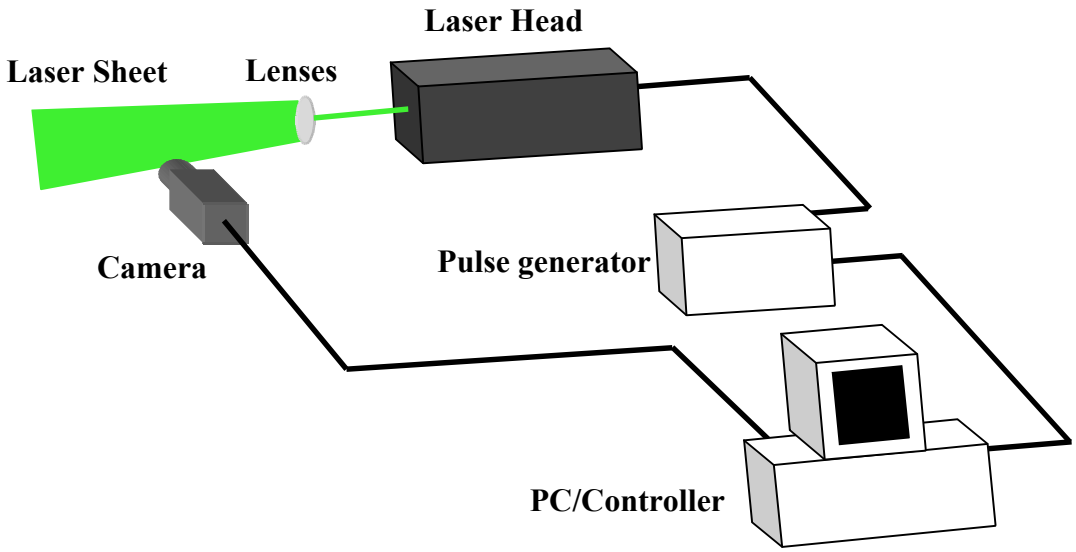

Figure 2.6: Basic configuration of a PIV system.

2.2.1 Tracer Particles

As the PIV technique measures the velocity of seeded particles, it is very crucial that these tracer particles accurately follow the flow. This is only possible if they are either neutrally or near-neutrally buoyant. Furthermore, the tracer particles must scatter enough light so that they can be properly detected by the camera. Unfortunately, both attributes are adversely proportional (to each other) and are controlled by particle diameter, d_p. Siddiqui and Nabavi [48] present the particle response time as a test to reflect its tendency to achieve velocity equilibrium,

$$\tau_p = \frac{(\gamma - 1) d_p^2}{18\nu}, \qquad 2.1$$

where τ_p is response time, γ is the ratio of particle to fluid density, and ν is the kinematic viscosity of the fluid. If the particle response time is at least a hundred times smaller than the flow's Kolmogorov time scale, then d_p is adequate. As such, the general rule of thumb for acceptable d_p in wind turbine flow applications should be identifiable in microns (10^{-6} m).

2.2.2 Pulse Generator Synchronization

Successful recording of an image pair, for particle velocity determination, necessitates synchronization between the double-pulse laser emission and camera frame. A signal generator in the image acquisition software synchronizes the camera frame with the laser pulses via a 15 Hz signal. That is, both images of an image pair are synchronized with the laser pulses in the synchronization sequence. Figure 2.7 elucidates the image acquisition process. The camera's sensor records the first image near the end of the first frame, while the second image is acquired shortly after the beginning of the second camera frame. This approach is called Frame Straddling. The temporal separation between the two images, which is user-adjustable, is called the time delay (Δt). Ramasamy and Leishman [49] discussed that Δt for rotor wake flows must be set sufficiently small to reduce errors due to flow acceleration, curvature effects, and particle

displacement estimations. Typical time delays are on the order of 10^{-6} seconds to render minimum and maximum particle velocities of suitable accuracy.

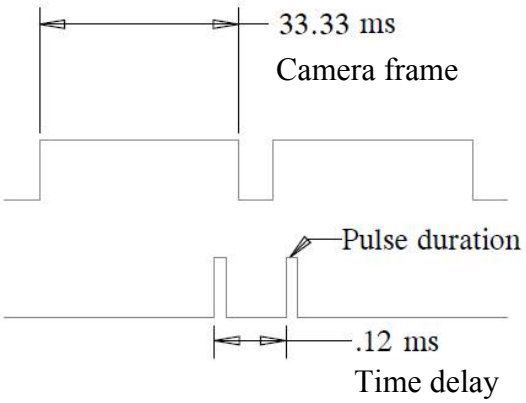

Figure 2.7: Camera frame and laser pulse synchronizatıon; one cycle shown as reference (times are not drawn to scale). The circuit is based on camera frame rate of 30 Hz.

2.2.3 Image Processing

Ascertaining velocity fields from the seeded flow requires image pairs to be statistically analyzed via cross-correlation. From basic statistical theory, the cross correlation of two stationary, random variables (f and g) is defined as,

$$\rho_{fg}(\tau) = \frac{R_{fg}(\tau)}{\left[\left\langle \sigma_f^2 \right\rangle \times \left\langle \sigma_g^2 \right\rangle\right]^{1/2}} = \frac{\left\langle f(t) \times g(t+\tau) \right\rangle}{\left[\left\langle \sigma_f^2 \right\rangle \times \left\langle \sigma_g^2 \right\rangle\right]^{1/2}}, \qquad 2.2$$

where stationarity denotes that the random variable's statistical properties are invariant to a time-shift, τ; $R_{fg}(\tau)$ is the cross covariance; σ^2 is the variance [50].

Figure 2.8 illustrates a general Fast Fourier Transform (FFT) cross-correlation process to output the resulting vector. Since particles generally shift in the direction of flow from first to second image, the pair is divided into small square grids, known appropriately as interrogation windows. Subsequently, interrogation windows from the first image are mapped onto the corresponding search region in the second image, where digital cross correlation scrutinizes the particle shifts with a predefined displacement tolerance (i.e. $1/4$ of an interrogation window).

Depending on the spatial resolution sought after, a variety of interrogation window sizes, in square pixels (i.e. 24^2, 32^2, 64^2), are available. Also, it is common to have a doubling in window size in the search region in the second frame.

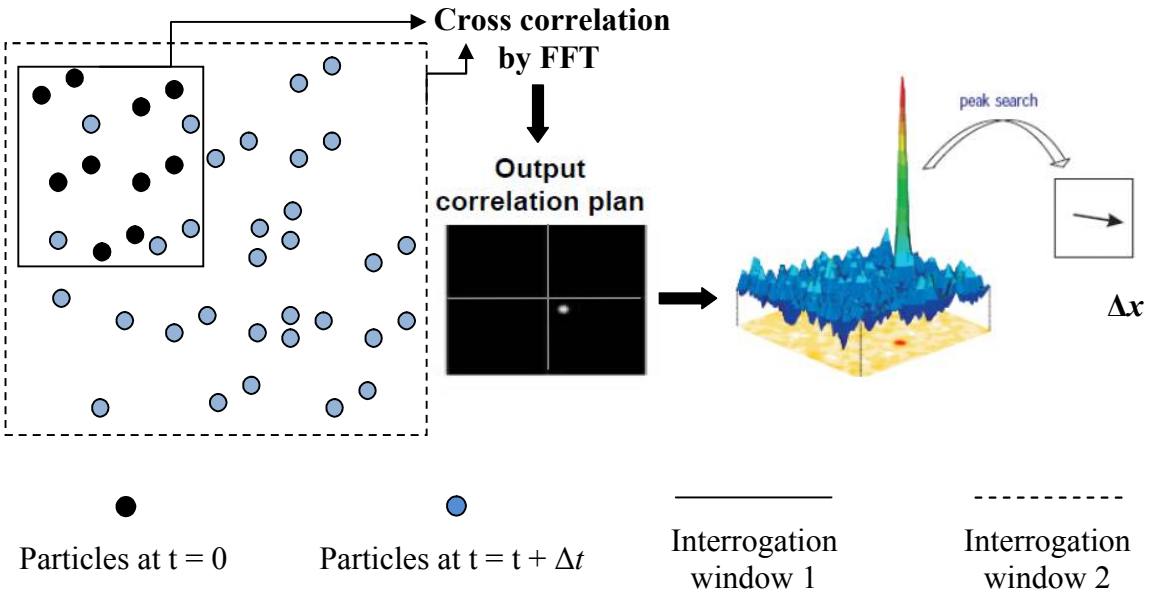

Figure 2.8: General FFT cross correlation method for PIV image analysis, adapted from [50].

When the frames are correlated at the initial location, the cross-correlation between the interrogation window and same size region in the search window gives the first correlation coefficient. The correlation coefficients' plane is obtained by mapping the interrogation window in the search region while simultaneously performing cross-correlation. The peak in the correlation plane provides the average particle shift in that interrogation window. The accurate coordinates of the correlation peak are obtained by using one of the sub-pixel curve fitting schemes, such as bilinear or three-point Gaussian [49]. Consequently, a single resultant vector is representative of the mean particle displacement (Δx) of all seed particles within the window. Lastly, the pixel displacement is converted into units of velocity through the camera's magnification factor, M, as shown in the following equation,

$$\tilde{U} = \frac{M\Delta x}{\Delta t}, \qquad 2.3$$

where M has units of [length/pixel]; Δx in pixels; and the time delay is in seconds [25].

2.3 Experimental Apparatus and Procedure

The experiments were conducted in a wind tunnel located in the fluid dynamics lab at the Concordia University. The wind tunnel is of closed circuit design, with a test section having dimensions of 0.45 m x 0.45 m in cross-section and 3.5 m long. The blockage ratio for the scaled HAWT is 8.7 percent. The fan is powered by a 1.5 HP electric motor, mated to a stepped frequency drive, delivers wind speeds from 0 to 5 m/s [51]. A flow straightener distanced 1.72 m away from the turbine provides uniform flow. Access to the tunnel's interior is possible by removing the series of plexiglass panels that make up its top cover. The model turbine is screwed onto a separate, thin piece of particle board, which is subsequently duct-taped onto the tunnel surface.

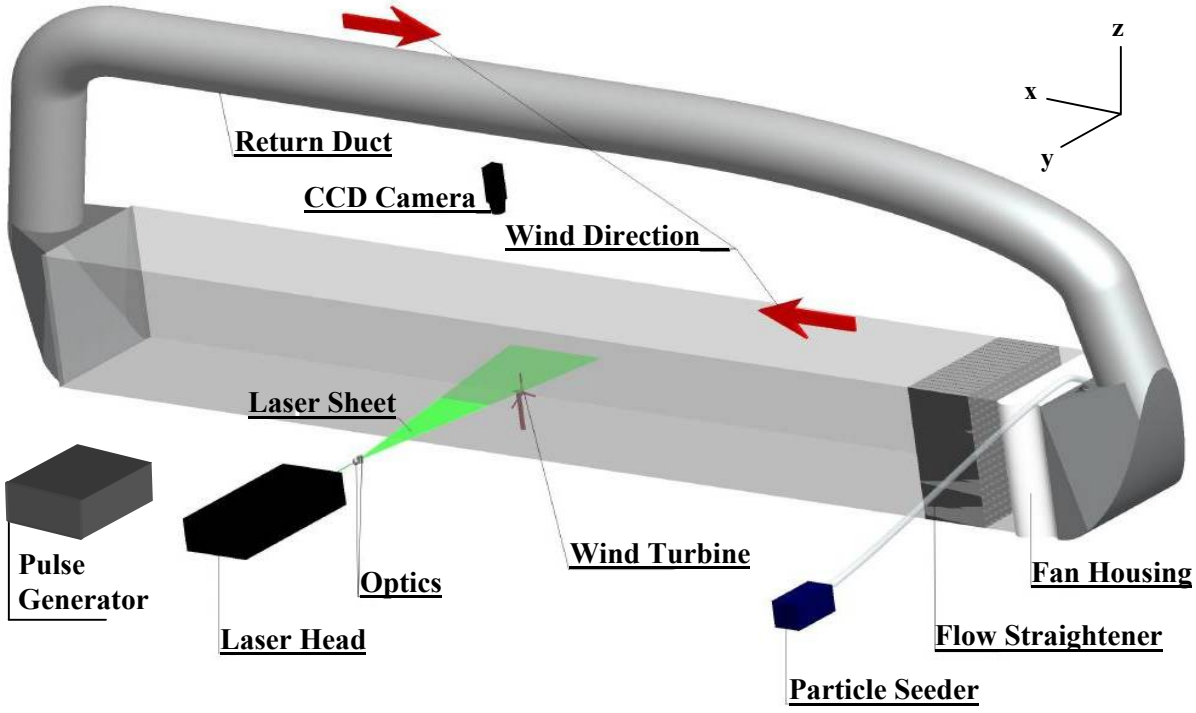

Figure 2.9: Experimental setup including the PIV system.

The PIV system used in the present study, shown in Figure 2.9, is comprised of a NWR Solo PIV 120 XT laser as light source, four channel BNC delay generator, JAI CV-M2 CCD camera, and optical lenses. The 120XT is a 120 mJ/pulse dual cavity Nd:YAG laser with a maximum repetition rate of 15 Hz at a wavelength of 532 nm. The laser is synchronized via the BNC delay generator where the time delay is set equal to 120 μs. A pair of optical lenses, one spherical and the other cylindrical, are used to form a thin, horizontal laser sheet at measured heights of 0.05 m, 0.135 m and 0.185 m, above the tunnel floor.

Images are captured by the JAI CV-M2 digital CCD camera at a resolution of 1600 x 1200 pixels. Picture magnification is handled by pairing the camera to a 50 mm, f/2.8 Linos lens. Figure 2.10 shows a lever arm mechanism that allows in-plane panning and translating of the camera, while out of plane rotation is controlled by the attached end plate. Once the lens' aperture and sharpness are adjusted, several snapshots are taken with a ruler placed flush along the laser sheet (switched to low power) as seen in Figure 2.11. They later serve as calibration images during the post processing phase to convert from pixel scale to a length scale.

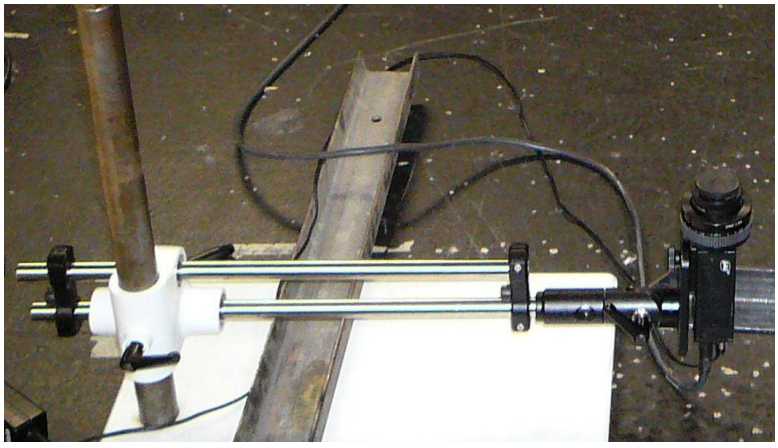

Figure 2.10: CCD camera positioning structure.

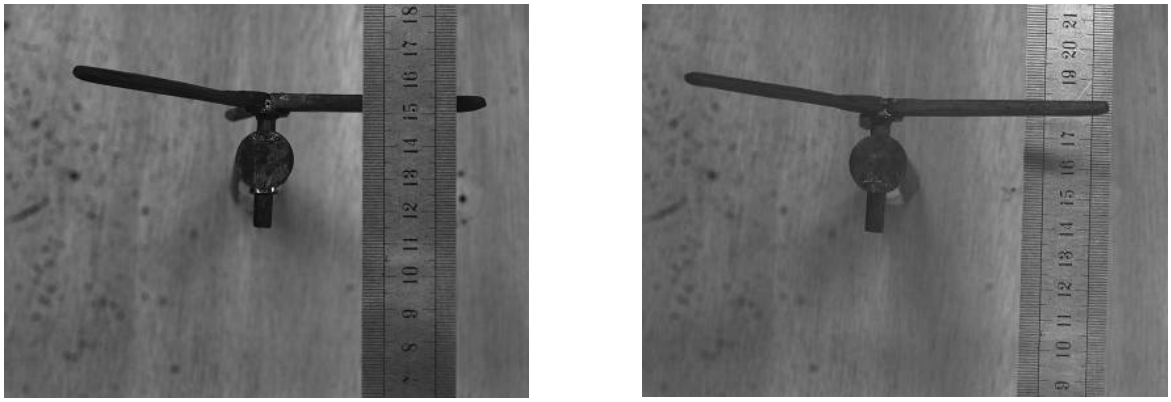

Figure 2.11: Calibration images to determine lens magnification (left: 0.185 m; right: 0.135 m).

The camera is connected to a PC installed with the video recording software, VideoSavant® (I O Industries, London Ontario) in which the program is set in a manner such that the camera records a total of 1800 images at a rate of 30 Hz. At all three heights, the flow is seeded with an oil based substance, 2-Ethylhexyl Sebacate, having an average d_p of 1 μm. The seeding is introduced into the tunnel by an aerosol generator through a 1" hole in the diffuser. From Eq. 2.1, its response time is found to be equal to 2.64 μs, with d_p = 1 μm; γ = 714, and ν = 15E-6 m^2/s. Comparing this value to an estimated Kolmorogov time scale (τ_η) of 1.31 ms, the particle response time is approximately 500 times quicker. Thus, it is rightfully concluded that the 2-Ethylhexl Sebacate particles properly track the flow.

The operating conditions are summarized in Table 2.1. An external handheld anemometer (Airflow TA-5) was utilized to register an equivalent freestream velocity to the frequency drive output. A total of 8 runs were completed: 4 and 3.5 m/s at 0.185 m, while all three wind speeds were tested at 0.135 m and 0.05 m.

Table 2.1: Operating conditions at various fan speeds

Fan Frequency [Hz]	U_∞ ***[m/s]***	λ	$\mathbf{Re_c}$
50	4	4.24	2533
45	3.52	3.47	2229
40	3.22	3.54	1900

Despite the lack of a tachometer to measure rotor frequency, the tip speed ratios at various fan speeds were computed by an alternate approach using PIV images. The details of this approach are as follows. Select an image from any image pair and take note of the blade to light sheet intersection; mark this as t = 0 (i.e. reference image). Begin cycling through image pairs and count the number of revolutions the reference blade makes within a phase margin of $\pm$ 5°. Knowing the pulse rate is 15 Hz, or an image pair occurring every 66.66 ms, the rotor's angular frequency is deduced by dividing through the total number of revolutions with the time span covered in tallied image pairs. Once the necessary values are unveiled, the tip speed ratio is calculated from Eq. 1.13, with R = 0.075 m. The chord Reynolds number is computed from Eq. 1.16 using the chord at mid span as the characteristic length (typical practice due to irregular airfoil section), with c = 0.0095 m; kinematic viscosity of air, v, approximated as 15E-6 m^2/s. The values of chord Reynolds number for the present experiments are also given in Table 2.1.

2.3.1 Post Processing

The velocity fields are obtained by cross-correlating the image pairs obtained from the PIV measurements. An in-house code in Heurisko environment is used to obtain the velocity fields. For cross-correlation, the interrogation window size is set equal to 24 × 24 pixels and the search window size is set equal to 48 × 48 pixels. A 50% overlap is set to increase the nominal resolution of the velocity field. This resulted in a total of 12610 velocity vectors with the spatial resolution of 1.21 mm × 1.21 mm. Raw instantaneous velocity fields at two heights are shown in Figure 2.12. The plots exhibit random spurious vectors in some regions while significantly large number of spurious vectors is present at other locations. The regions with large number of erroneous vectors are the areas where the turbine blade or the post created a shadow (see Figure 2.13 a). Since the PIV technique relies on the illumination of the tracer particles, in the shadow

regions, no particles are illuminated, as a result the cross-correlation picks up noise as the correlation peak and resulted in spurious vectors.

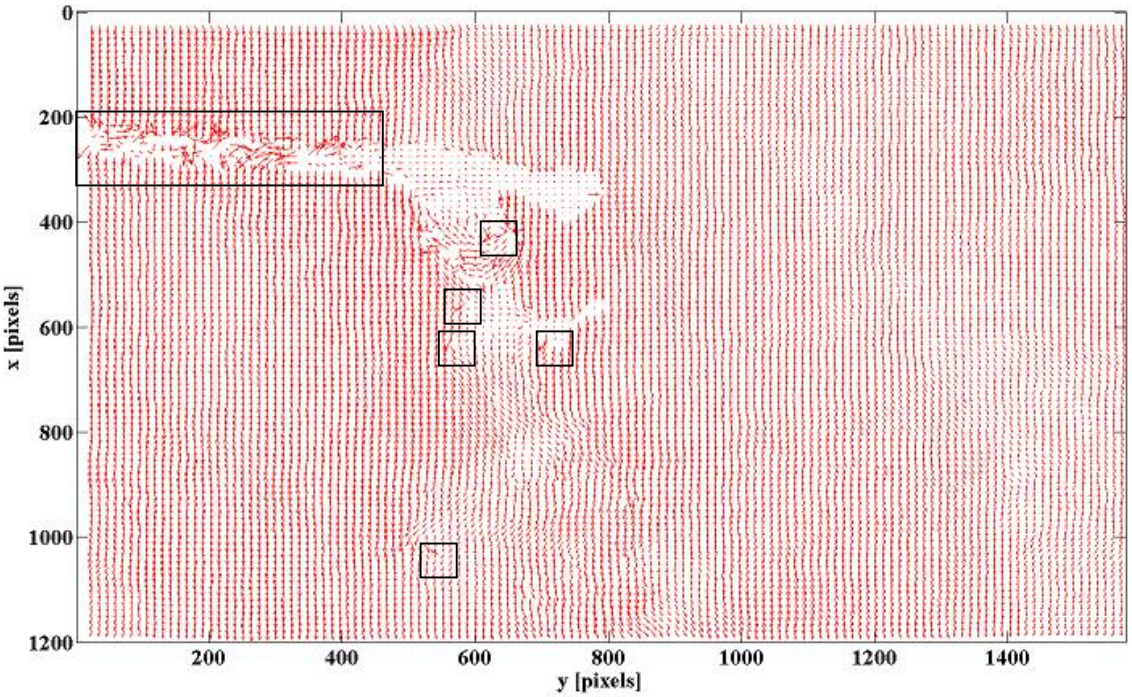

(a)

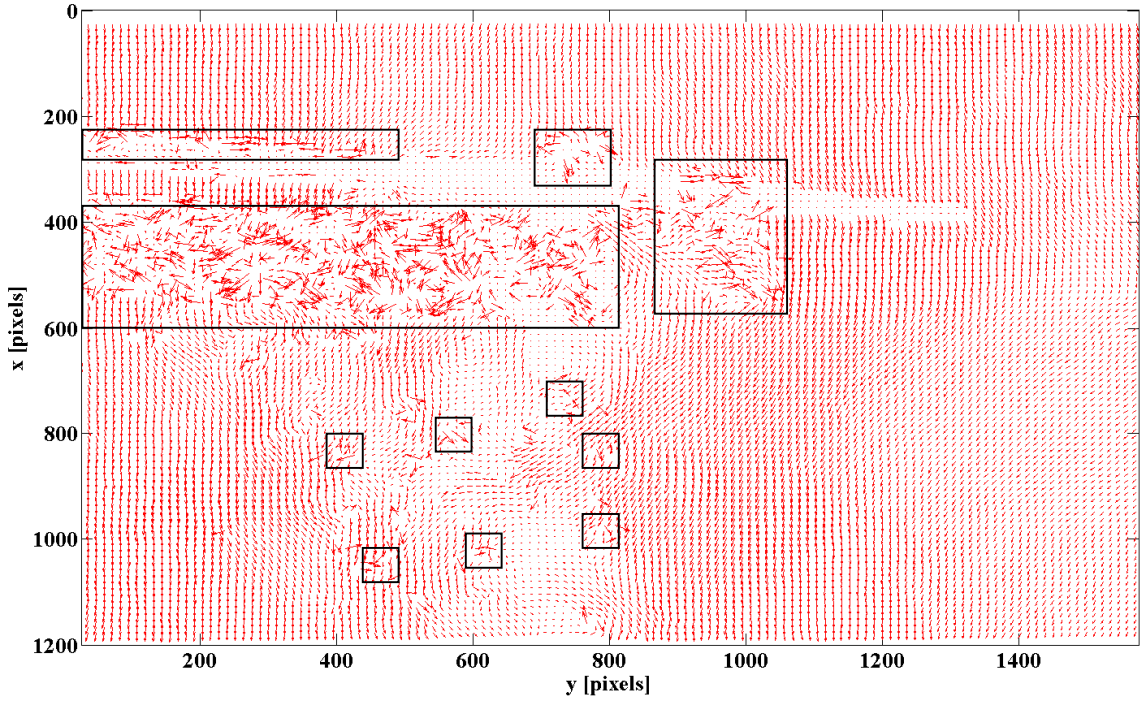

(b)

Figure 2.12: Raw instantaneous PIV velocity vectors with encased regions of erroneous vectors at measurement height of **(a)** 0.185 m **(b)** 0.135 m.

These vectors must be removed so that they do not introduce errors in the computation of flow properties. In order to rectify the latter issue, two additional MATLAB® algorithms are required in tandem to detect the shadow regions and to exclude any data in these regions from further analysis. Introduced by Rasouli, Hangan, and Siddiqui [52] as a mean to mitigate unnecessary data loss in digital photographs, the first algorithm reads in the set of 1800 greyscale images and outputs them into binary format (Figure 2.13 b) by removing all objects exceeding a precise contrast level that defines either the shadowed region or bright spots. All newly formed binary images along with their PIV files are then called upon, one by one, into the second code to serve as filters: a conditional statement scans for cells containing a 1 (ubiquitous for white) on the binary image and proceeds to assign a 'NaN' (Not a Number) to the PIV data if true. That is, all vectors in the shadow regions are excluded from further analysis.

Three actions are taken by the second algorithm for velocity vectors in the valid regions: one is to correct the spurious vectors using the local median test, the second shifts all vectors such that their midpoint intersects the nodal point of the interrogation window (i.e. center) using Adaptive Gaussian Interpolation, and finally the vectors are converted into units of velocity along with computation of its derivatives. In stage one, for a given vector, a median value is calculated from the eight neighbouring vectors (or five if the vector under interest lies on the edge). Both the magnitude and angle of the given vector are evaluated against the median value. If both fit within certain limits in relation to the median vector, the considered vector is unmodified; otherwise, it is replaced by the median (see Figure 2.14). The local median test is described in detail in Siddiqui *et al* [53].

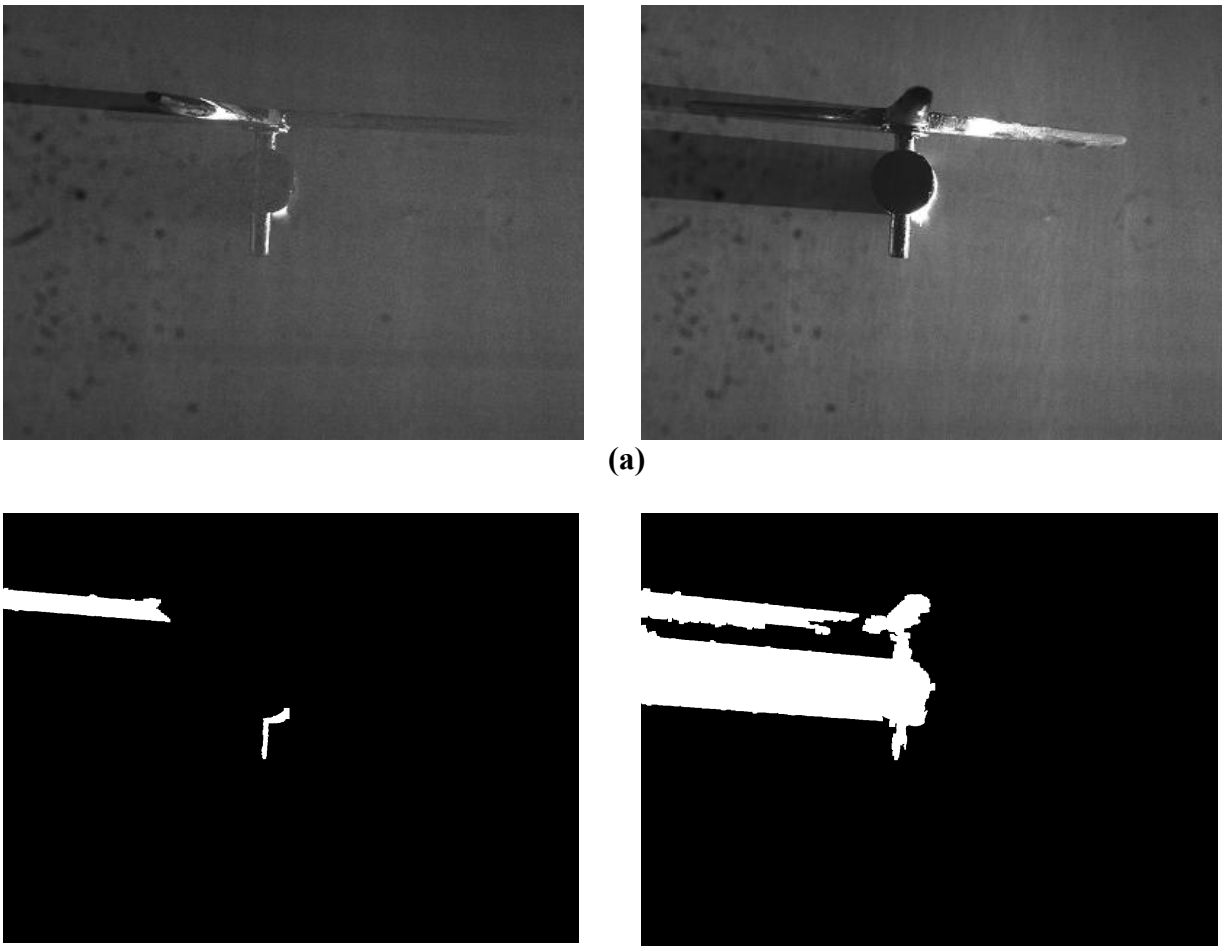

Figure 2.13: Creation of the threshold image for spurious vector removal (left: 0.185 m; right: 0.135 m) **(a)** original images recorded by camera **(b)** binary images.

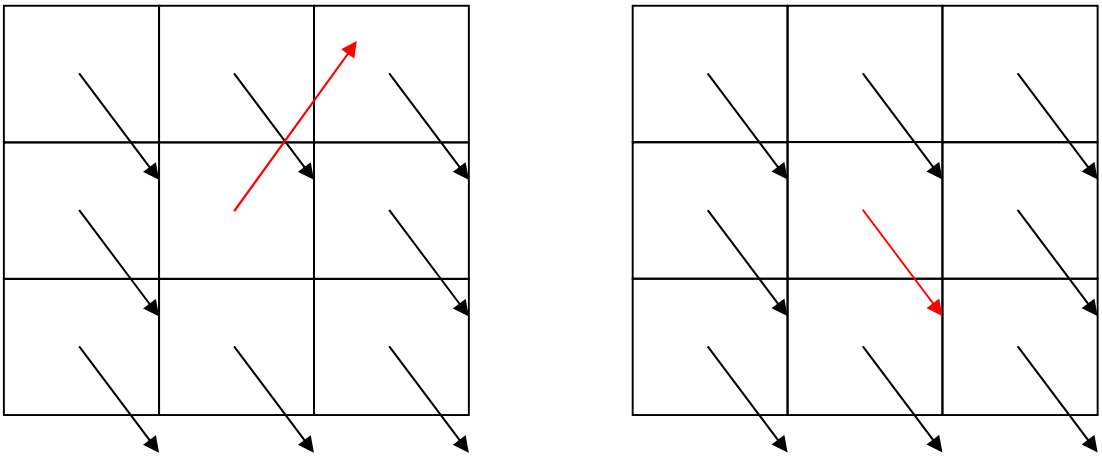

Figure 2.14: Spurious vector (red color) correction using the median value of neighbouring vectors (left: before correction; right: after correction).

Heurisko's cross correlation algorithm, which situates a mean displacement vector's base at an interrogation window's nodal point, presents serious drawbacks for data post processing. Firstly, the distance between each velocity vector changes because its magnitude is measured from the midpoint; in short, book keeping for velocity gradients becomes a nuisance. Secondly, time averaging would not be possible because the vector associated with one particular node point is not guaranteed to be at the same spatial location in subsequent fields. Charged with the task of rearranging every vector in stage two is a tool known as Adaptive Gaussian Window interpolation. Consolidating all measures up to this point, the spurious vectors are corrected with each of the 12610 velocity vectors contacting the node point at their midpoints. Showcased in Figure 2.15 are the finalized instantaneous velocity fields after implementing the magnification factors, extracted from Figure 2.12. To wrap up the algorithm, a central difference scheme is utilized to compute the velocity gradients.

2.3.2 Uncertainty Analysis of the PIV Velocity Data

Factors inherent within the post-processing phase contribute to the total error in the computation of the velocity vectors. These include velocity gradients, particle diameter, out of plane motions, peak locking (associated with the sub pixel determination of the correlation peak), and AGW interpolation [54]. The results of Prasad *et al* [55] and Cowen and Monismith [54] have been used to estimate the uncertainty in the velocity measurements. Table 2.2 summarizes the error at each of the measured heights. The detailed uncertainty analysis is presented in Appendix A.

Table 2.2: Uncertainty in velocity measurements at all heights

Measurement Height [m]	Uncertainty in Velocity Measurements [%]
0.185	5
0.135	5.2
0.05	6.4

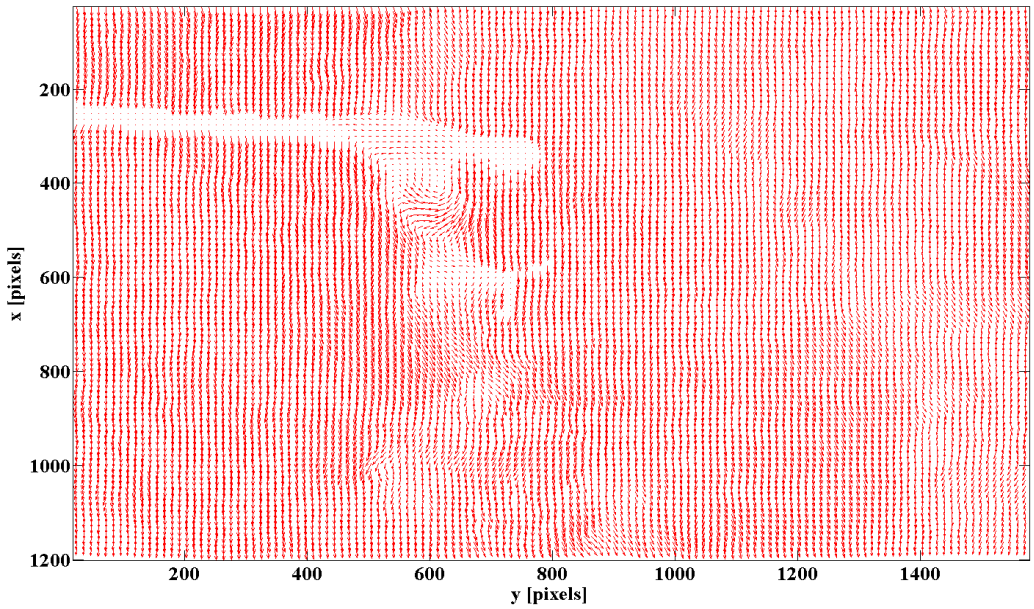

(a)

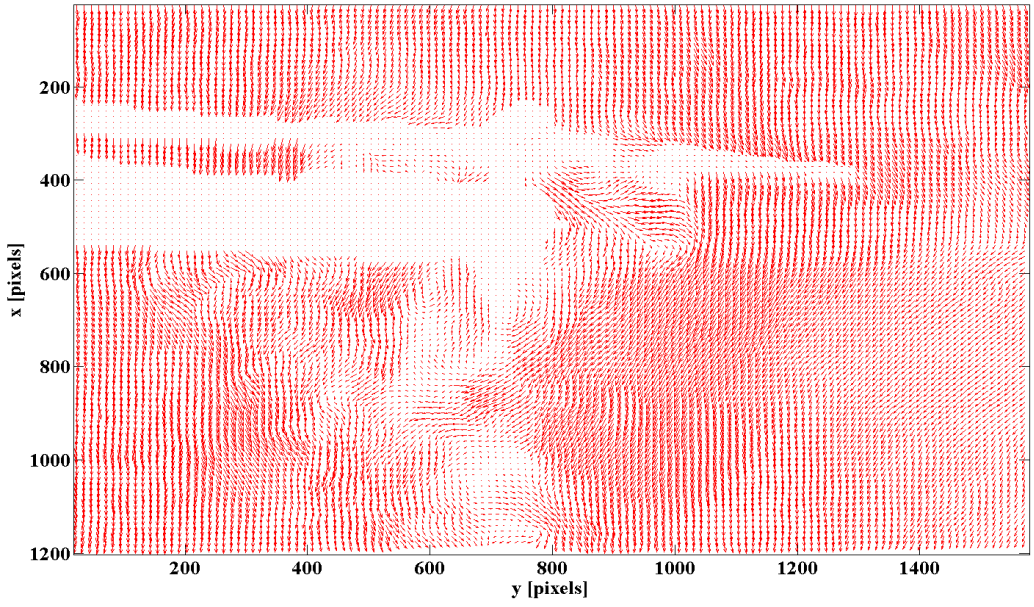

(b)

Figure 2.15: Corrected instantaneous velocity field of the images shown in Figure 2.12, respectively **(a)** 0.185 m **(b)** 0.135 m.

2.3.3 Phase Averaging

In order to compute both the mean and turbulent characteristics of the flow for in-depth analysis, the method of phase averaging is used. The central idea behind this technique is to isolate rotor configurations from the PIV image into a series of phase partitions, or bins. Flow properties are summed and subsequently averaged by the phase criteria of the bin. Figure 2.16 presents a flowchart detailing the step by step procedure of the phase averaging algorithm utilized at the measured height of 0.185 m. The main aspects of the algorithm are described below.

If one recalls the conditioning algorithm to begin removing spurious vectors from the raw PIV vector plots, the first three stages in the phase averaging code – loading the greyscale image, followed by its conversion into black and white, and subsequent scanning of a predetermined region for white patches – are indeed similar. When the scan is completed, a counter that keeps track of the number of white pixels and their locations, occurring on either side of the shaft center (defined as the origin; y-position = 740), is subjected to conditional statements. Since the intensity spots are not an indication of the tip location, only where the reference blade intersects the laser sheet (i.e. Figure 2.13 a), a correction factor is applied to the extremum pixel ascertained from the conditional statements. Once the y-location of the blade tip is resolved, its relative length in relation to the shaft is computed and stored in a matrix.

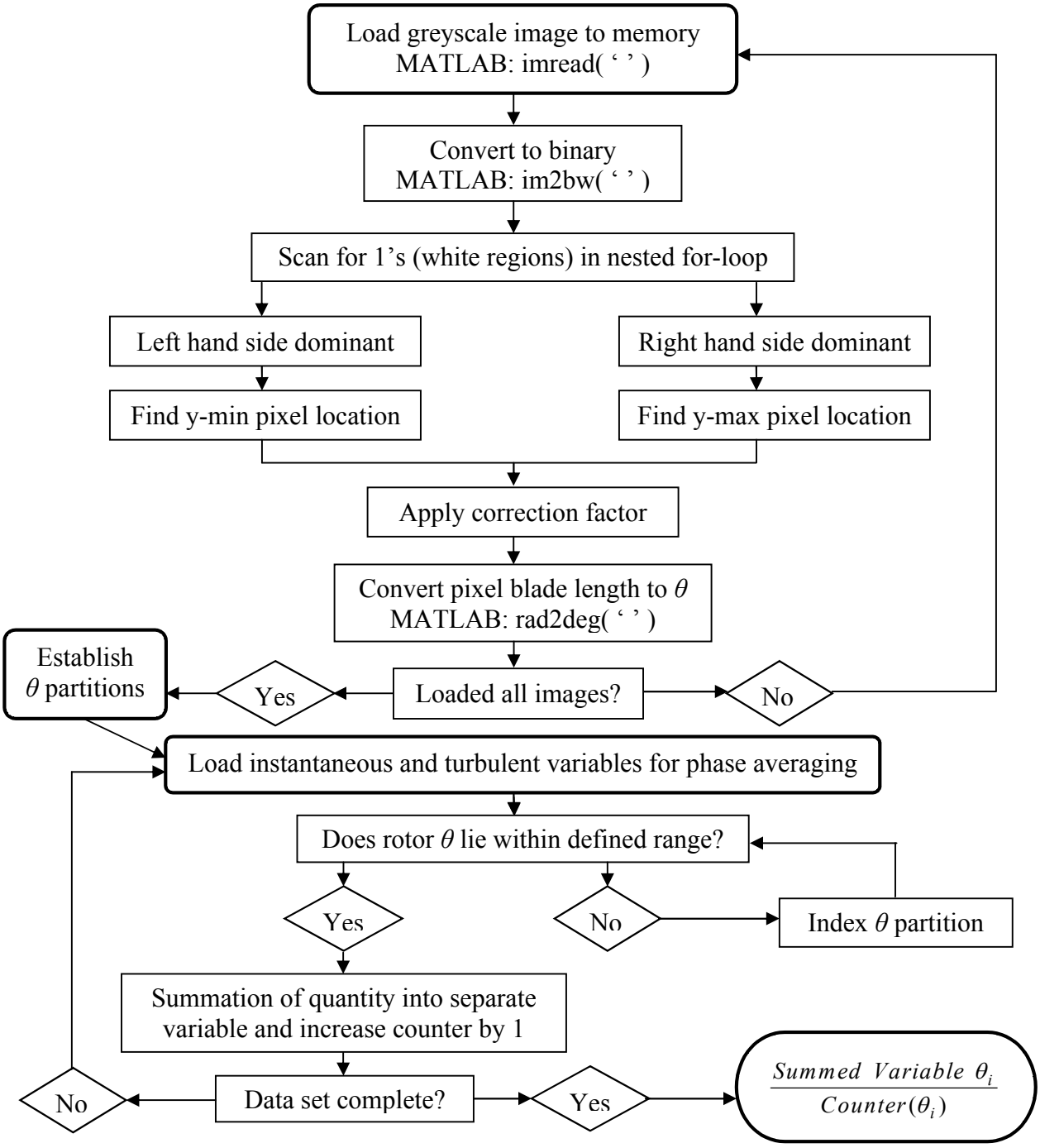

Figure 2.16: Flowchart of the phase averaging method for measurements at a height of 0.185 m.

Converting the relative length into an angle requires the camera magnification factor, at the correct height, to change the blade's length of 0.075 m into its equivalent in pixels. Next, the inverse cosine is taken between these two sides resulting in a phase measurement in radians, which is then converted into degrees. Once the angle for each image is computed, phase partitions are generated by segregating the minimum and maximum value into 10 degree bins. The bins are viewed from 0-120^{o}, and the configurations are fully detailed in Figure 2.17.

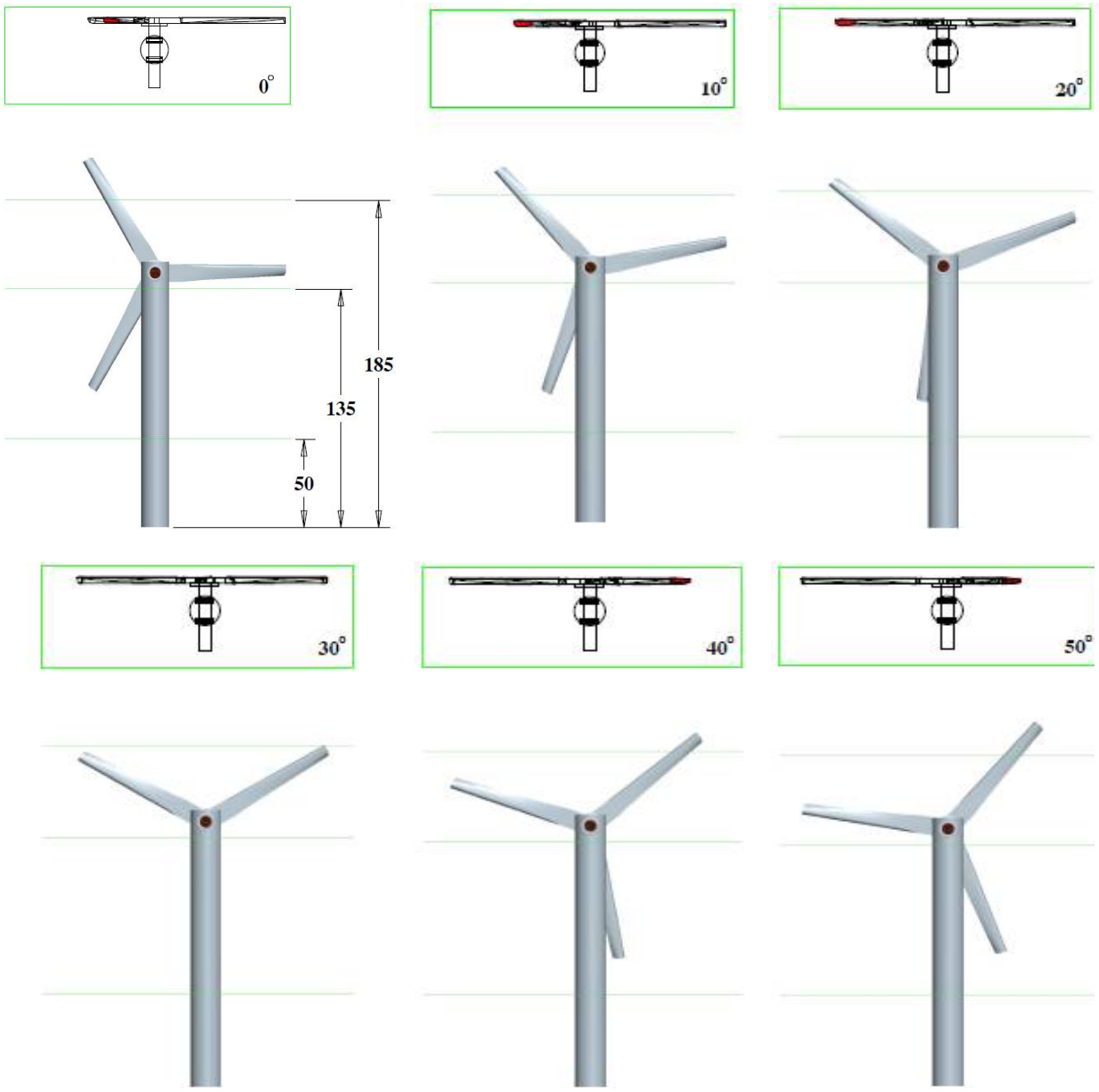

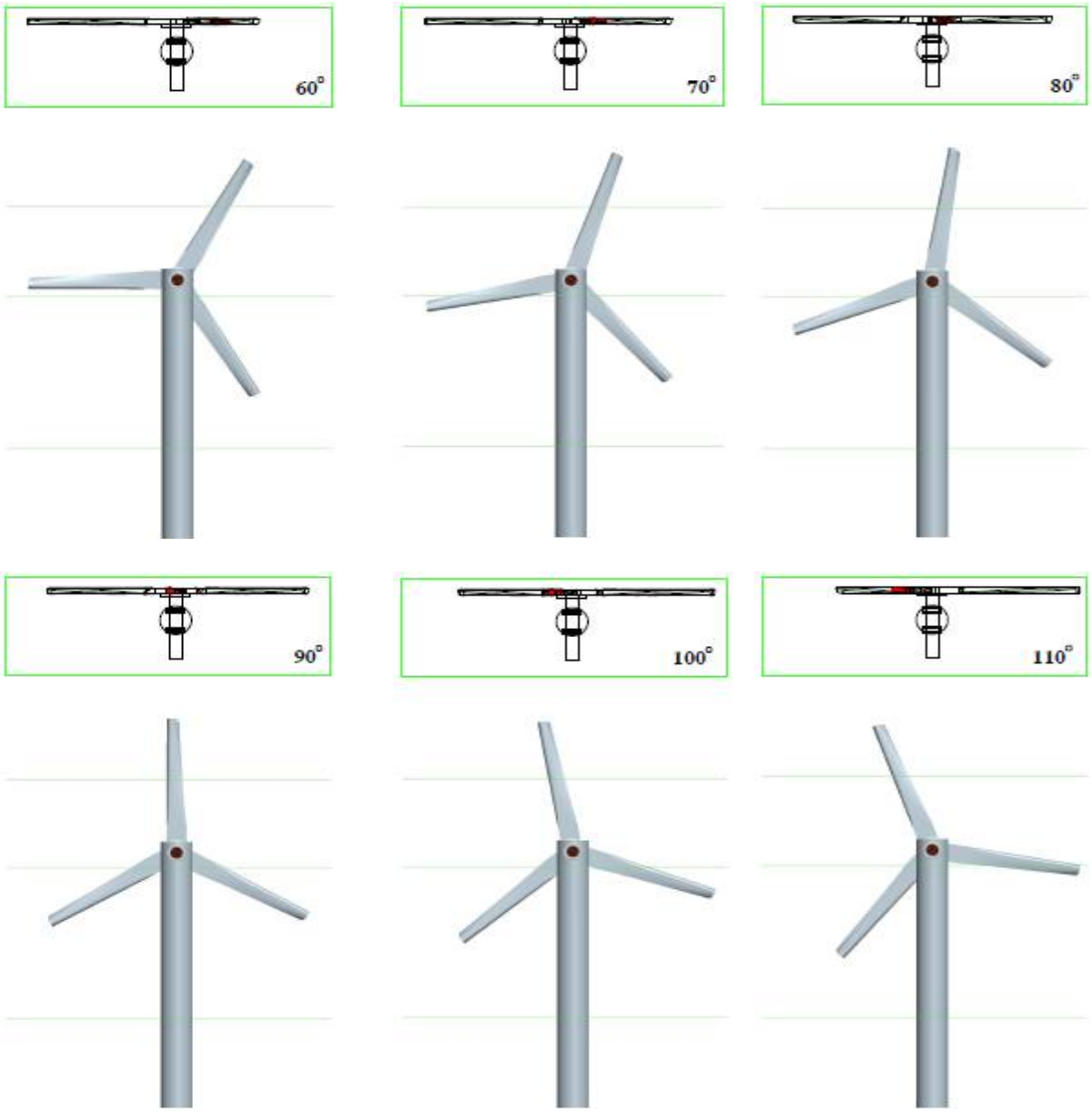

Figure 2.17: Phase angle orientation; measurements are given in mm. Rotor spins counter-clockwise.

Each panel contains a top view (CAD rendition of what the camera records) with the blade-laser sheet cross section shaded in red, an inset of the midpoint for the phase angle partition, and a front view seen from the rear. The three horizontal lines mark the height at which the laser sheet intersects the turbine.

The ensuing process is phase averaging instantaneous and turbulent quantities, initiated by sequentially verifying the stored angles against a conditional statement (partition midpoint $\pm$ 5°). If the comparison agrees, the vector field is summed into a separate matrix that is categorized by the phase bin. In addition, a phase counter tracks the number of image pairs associated with each bin and serves as the divisor when the data set is complete. However, if there is a mismatch between the stored angle and conditional statement, the partition limits are indexed in succession until the check is favourable.

When the data set is concluded, the compiled variable in each phase bin is divided by the counter. On the topic of averaging turbulent quantities, if interest is relegated to velocity fluctuations then the binning procedure works the same as with the instantaneous variables. However, dealing with statistical properties of the fluctuations such as higher order central moments (i.e. the variance), or flow terms consisted of derivatives, necessitated a Reynolds decomposition. Thus, the phase averaged mean terms are computed first before subtracting them from the correct instantaneous field.

Calculating phase averaged quantities at the height of 0.135 m foregoes the binary image sweep and correction factor due to the increased complexity in behaviour between rotor and laser. Instead, discerning the position of the reference blade's tip is accomplished manually, as outlined in Figure 2.18. In this algorithm, the scanning of white pixels and side dominance is replaced by two new actions. Firstly, the greyscale image in the data set is printed to the screen rather than program memory. Secondly, the step requiring human input, is that the MATLAB command, ginput(1), prompts the user to click once (i.e. the amount of clicks is dictated by the number in parentheses) on the image. Once the blade tip is chosen, the command stores both the

x and y coordinates and initiates the exact same processes as previously discussed in Figure 2.17, beginning at pixel blade length conversion, to arrive at a phase averaged variable.

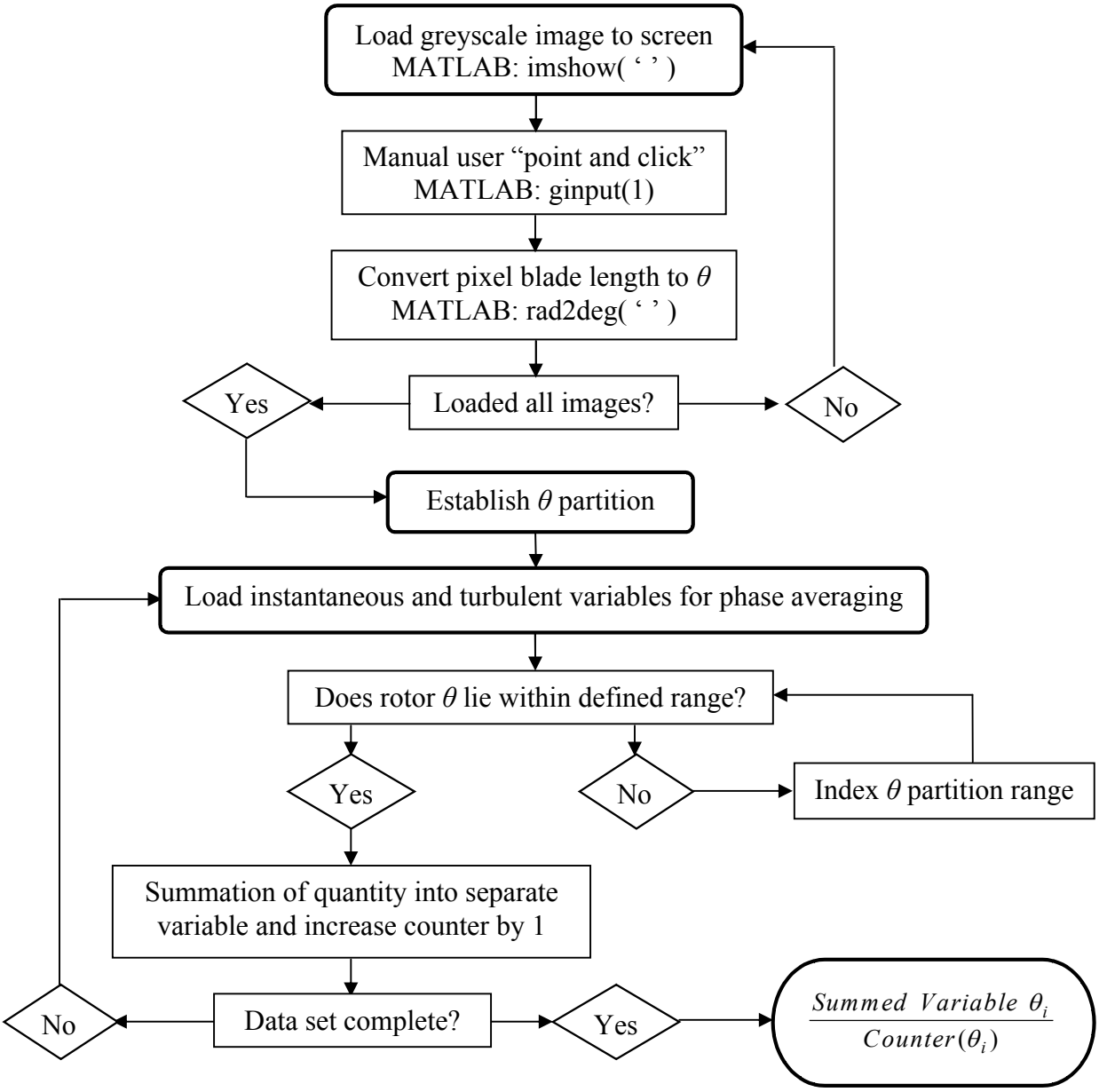

Figure 2.18: Flowchart of the phase averaging method at the measurement height of 0.135 m.

Chapter 3: Mean Flow Topology

This chapter is focused on the analysis of the mean velocity field. Specifically, the aim is to be critical of the phase averaged effects on the mean flow structure. Visual aids in the form of contour plots in the *x-y* plane are provided as a way to explain phenomena at the global scale, while the finer details of the flow parameter are graphically explored. Moreover, comparisons to past experimental or numerical trends will be mentioned for benchmark purposes. As mentioned in Chapter 2, the measurements were conducted on three horizontal planes at heights of 0.185 m, 0.135 m and 0.05 m from the surface, in the near-wake region. In this chapter, the mean flow characteristics at the height of 0.185 m are presented first, followed by the mean flow behaviour at heights of 0.135 m and 0.05 m. At heights of 0.185 m and 0.135 m, both phase averaged and ensemble averaged results are presented, whereas for the height of 0.05 m, phase-averaging was not possible; thus, only ensemble-averaged results are presented.

3.1 Measurements at z = 0.185 m

3.1.1 Instantaneous Velocity and Vorticity Patterns

Analysis of vortex behaviour is crucial to the understanding of several issues such as aerodynamic noise, unsteady spanwise blade loads, and turbulence. For a better perception of the near wake flow dynamics at different phases, instantaneous velocity and vorticity fields at U_∞ = 4 m/s are presented in Figure 3.1 at phase angles of 30, 60, 90 and 110 degrees. In Figure 3.1 (a, b, c), the horseshoe vortex can be identified by the pair of opposite rotating spirals that are eventually advected in a straight path by the mean flow. Within each structure, an inner core with highest axial vorticity is embedded in a diffused outer layer, which is consistent with the observations of Ebert and Wood [28] and Dobrev *et al* [47]. Peculiarly, in Figure 3.1 (d), the tip vortices are shed inward and such motions occur solely at this phase (recall Figure 2.17, 31

degrees). Distinctions between the two types of vorticity are succinctly documented by Snel [56]; he highlights that shed vortices are a by-product of unsteady, non-axisymmetric conditions (i.e. non-uniform inflow), having a tendency to move along the blade axis.

Figure 3.1 also shows that further downstream, beginning at x/R = 0.6, misaligned patches of vorticity of both signs emerge. Possible explanations include spatial variations in wake velocity combined with the induced field's influence, breakdown of vortices into smaller scales of turbulence, or remnants from a previous image pair.

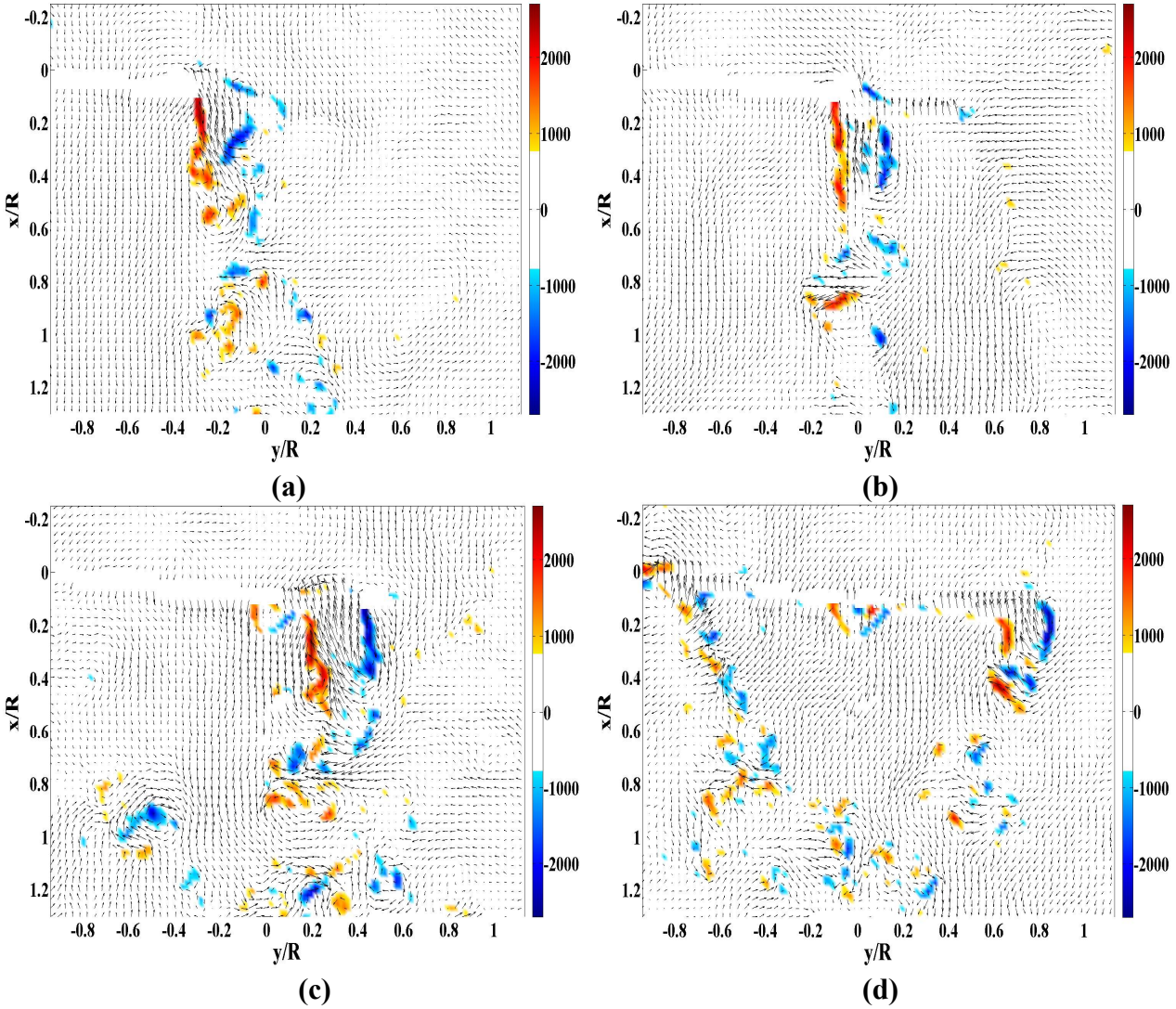

Figure 3.1: Instantaneous velocity vector maps superimposed with contours of instantaneous vorticity (Hz); ccw rotation is red, while cw is blue. **(a)** 110° **(b)** 90° **(c)** 60° **(d)** 30°.

3.1.2 Ensemble Averaged Velocity

The contours of ensemble averaged streamwise and crosswind velocity normalized by U_∞ are presented in Figure 3.2 (a) and (b), respectively. Effect of averaging across instantaneous fields is likened in having traces of interesting flow phenomena erased. Its impact is manifested in the streamwise component, where gradients in wake velocity at individual blade positions are completely swamped out. As a result, vorticity formation is significantly dampened. Ensemble averaging of the crosswind velocity leads to an almost antisymmetric profile about $y/R = 0$.

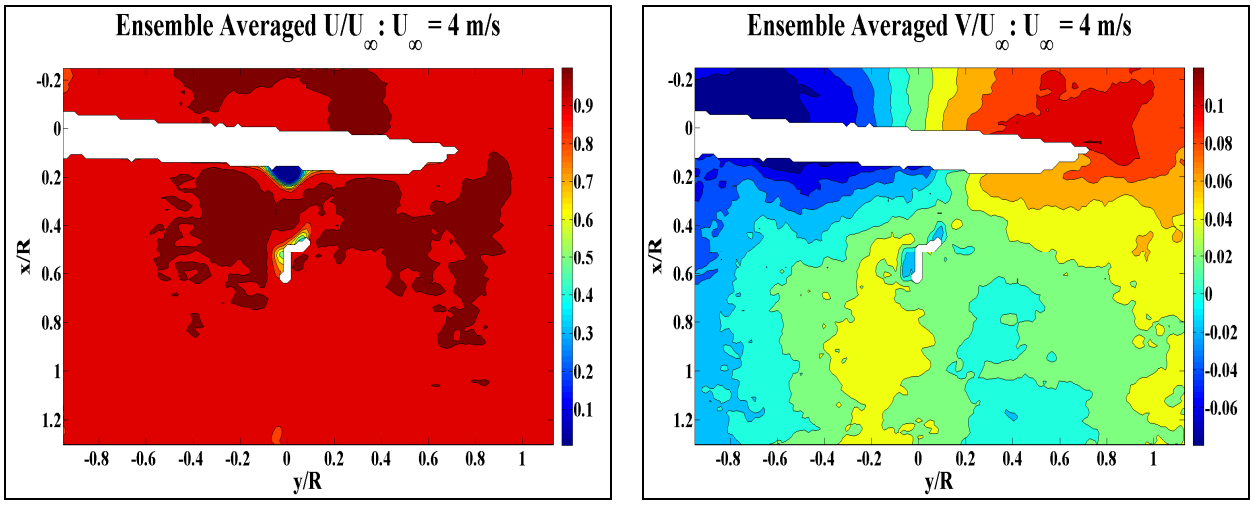

Figure 3.2: Ensemble-averaged contour plots taken at height of 0.185 m and U_∞ = 4 m/s **(a)** Streamwise velocity ratio **(b)** Crosswind velocity ratio.

3.1.3 Phase Averaged Streamwise Velocity

The phase-averaged contour plots of normalized streamwise velocity (U/U_∞) at selected phases are shown in Figure 3.3. At this height, the laser sheet shines above the cylindrical support tower, permitting a clearer idea into the way blade affects the freestream flow. In the upcoming sections, the term "reference" is used to denote regions in the wake that experience significant flow retardation, at shown phases. The plot of 90 degrees in Figure 3.3 displays regions in the turbine wake where the flow is accelerated, which are almost symmetric about the

turbine centerline. At a phase of 31 degrees, the region of flow acceleration occurs between the two blade tips (see Figure 2.17). The zones of flow acceleration arise naturally because the fluid perceives a decrease in area. Regions behind the blade are observed to experience flow deceleration (i.e. reference location), which is caused by flow separation attributed to high local angles of attack, and is common at lower λ. Similar behaviour in the contour of 90 degrees is observed at phases of 0 degrees and 60 degrees, indicating that the mean streamwise velocity is not completely uniform across the near wake, but rather, it is slightly higher than the freestream velocity in some regions. Results also show that this effect is also propagated slightly upstream of the blades.

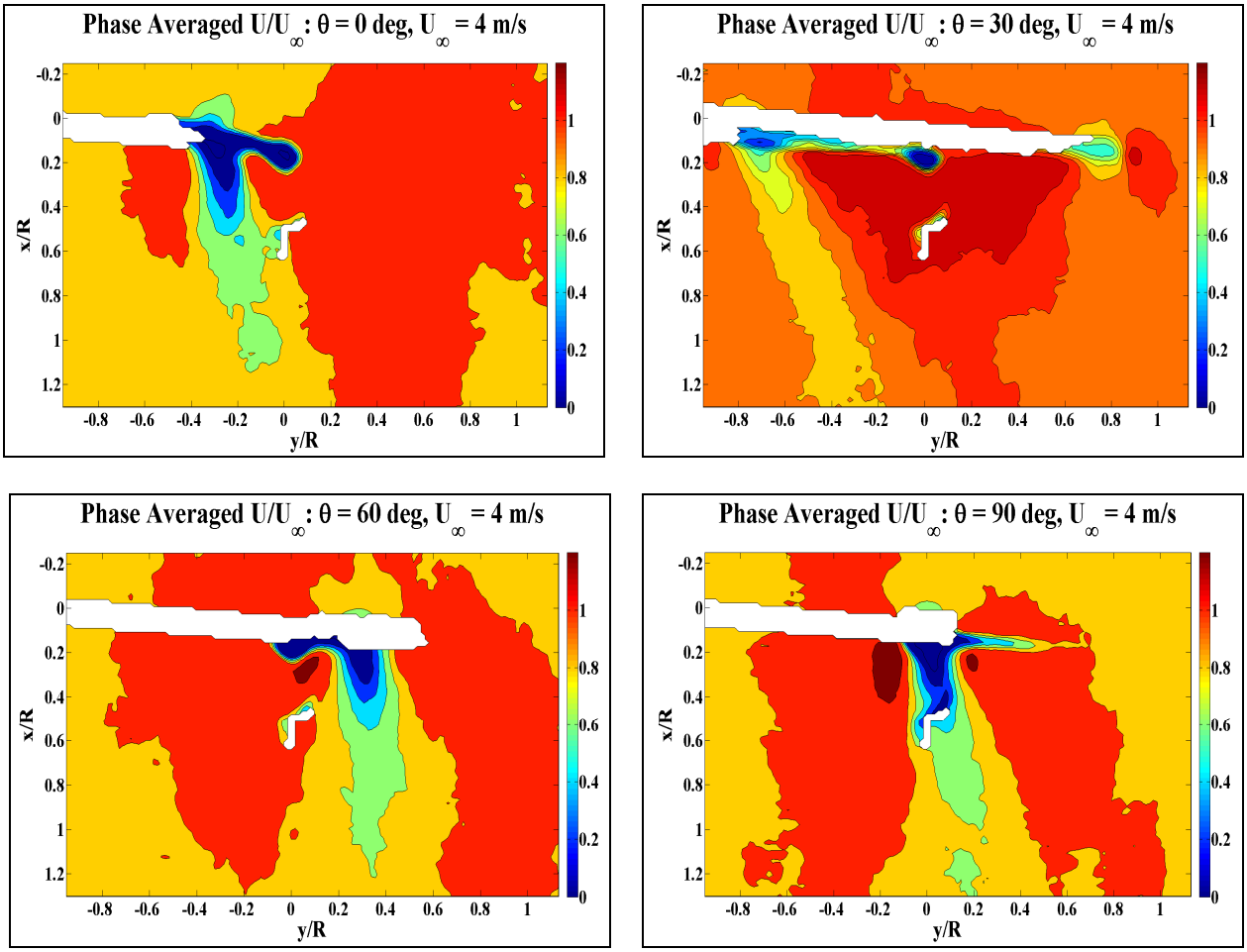

Figure 3.3: Normalized phase averaged streamwise velocity contour plots for a wind speed of 4 m/s.

3.1.4 Phase Averaged Crosswind Velocity

The structure of crosswind velocity is more complex than the streamwise velocity. The contours of phase averaged crosswind velocity normalized by the freestream velocity are plotted in Figure 3.4 at the same phases as in Figure 3.3. The flow structure just in front of the reference blades (in proximity to $x/R = 0$) is similar, where freestream flow splits into two paths due to presence of a stagnation surface. Unclear is whether the reattached flow in the wake, exemplified by opposite coloured columnar contours, is a single vortical structure or a system of vortices (see Chapter 1). Furthermore, as a response to the reaction torque caused by the rotor, wake rotation must occur in the opposite direction; in the present case, it means left to right movement.

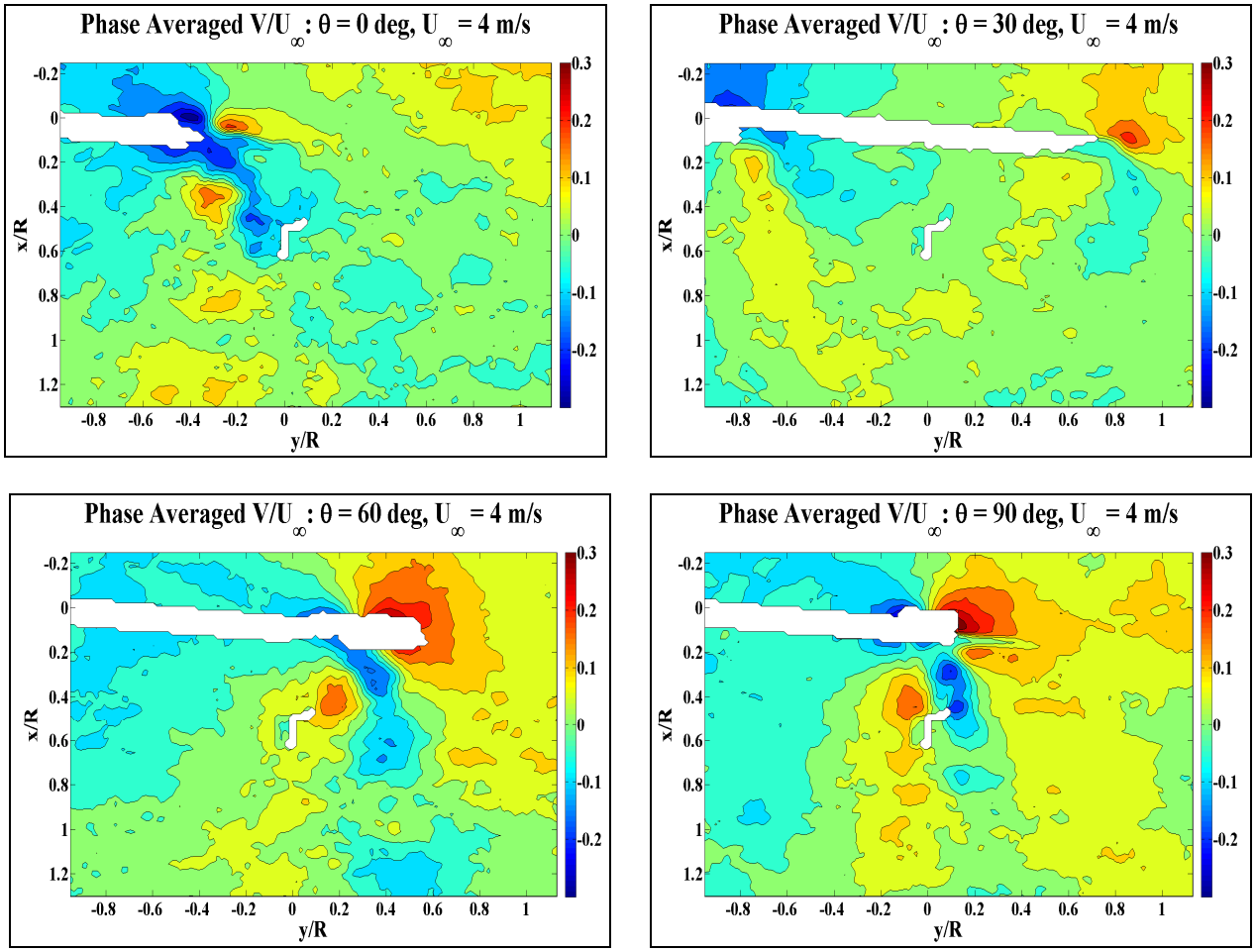

Figure 3.4: Normalized phase averaged crosswind velocity contour plots at a wind speed of 4 m/s.

3.1.5 Streamwise Velocity Deficit

The mean streamwise velocity deficit (1 - $<U>/U_\infty$) computed at different phases and in the ensemble form is plotted in Figure 3.5 at different crosswind locations that correspond to y/R = -0.4, 0.032, 0.4. The results are presented from x/R = 0.3 to 1.3 to avoid regions of higher data uncertainty closer to the blades. The data analysis reveals several interesting characteristics that normally do not receive exposure; specifically, it is common to view wake deficits as an ensemble average over many rotor revolutions. Two distinct trends, differentiating the behaviour between reference and non-reference phases, occur: the reference phases of 90 degrees at y/R = 0.032 and 60 degrees at y/R = 0.4, demonstrate a quasi-monotonic decay of the wake deficit, whereas the non-reference phases and ensemble averaged data show a steady increase. The latter transpires because of the wake expansion, which is known to be a strong function of C_T and λ [16], and which triggers both a decrease in axial velocity and pressure recovery, previously mentioned in Figure 1.1. Due to the planform surface of the rotor – a combination of sharp and rounded edges – the aerodynamic behaviour, behind a reference blade, perceived by the upwind flow is a mixture of blunt and streamlined objects.

Results at the phase of 90 degree show stagnant flow approximately 0.3R downwind which recovers to 80 percent of the freestream flow by 0.7R. Although the blade at 60 degrees is treated as a reference position in Figure 3.5, it has a lower initial deficit because the crosswind location is to the left of the accelerated zone as viewed from its contour in Figure 3.3. The behaviour in the plots appear to respond similarly even with a change of freestream velocity. However, the 3 degree profiles at y/R = -0.4 show large discrepancies in their signs. One factor could be meandering of the accelerated flow region inside the wake.

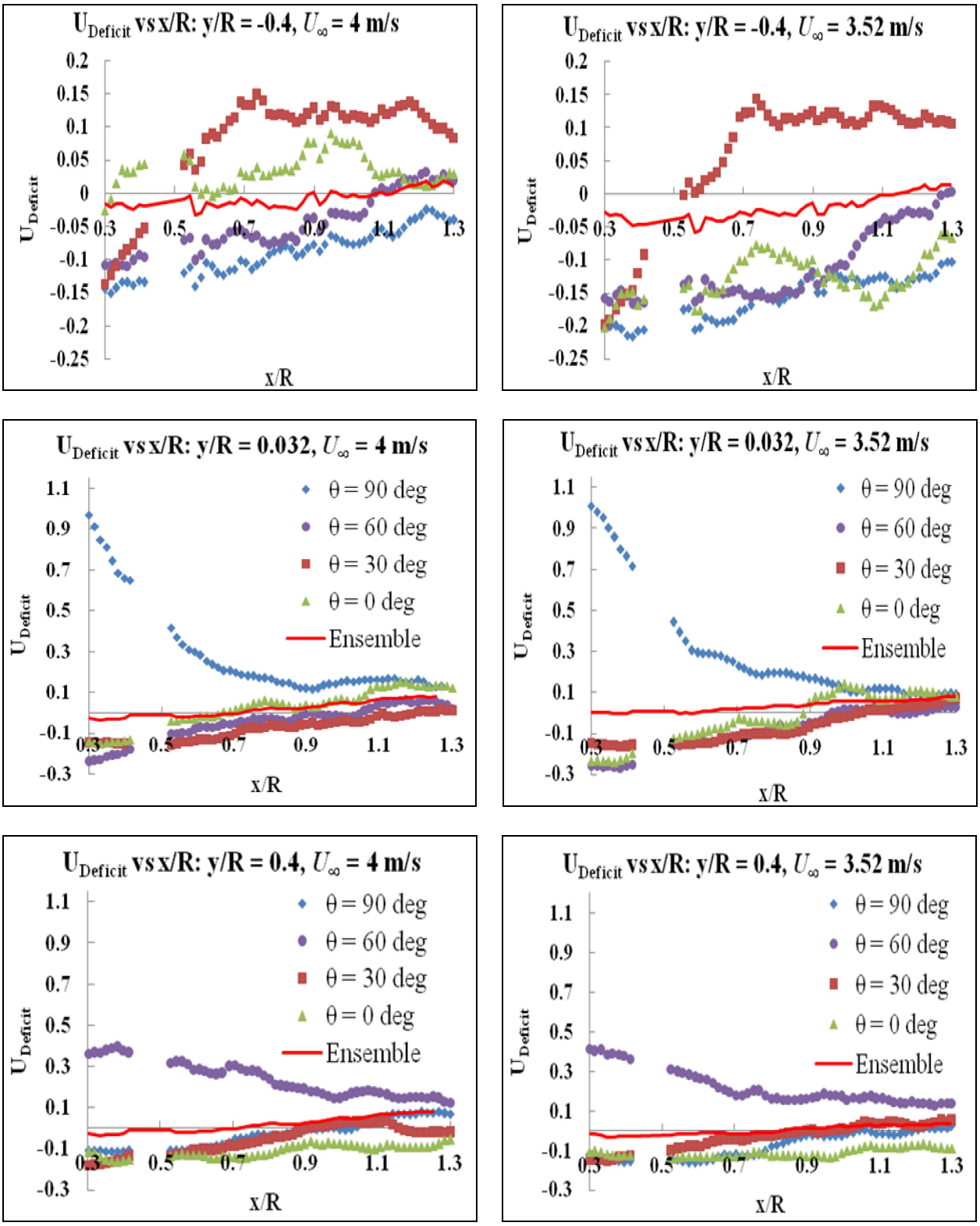

Figure 3.5: Streamwise velocity deficit at spanwise distances corresponding to y/R = -0.4, 0.032, and 0.4 at U_∞ = 4 m/s and 3.52 m/s.

A second reason may be due to a difference in sample size at this specific phase, which would alter the phase averaged mean velocity. Ensemble averaging smoothes out the fluctuations resulting in the solid curve nested between the phases.

Two independent researches, by Ebert and Wood [19] and Papaconstantinou and Bergeles [30], of similar wake extent concerning mean streamwise velocity deficits are reported in Figure 3.6. The other related parameters from these studies are presented in Table 3.1. The shape of their wake deficit profiles are similar to the profiles of the wake deficit presented in Figure 3.5, although the magnitudes are different. The comparison of the deficit profile shape obtained in the present study with that from the above mentioned studies is quantified in terms of the profile slope obtained through the linear fit. The results are presented in Table 3.2. The results show a fairly good agreement between the slopes among these studies. The differences could be due to the airfoil shape and the Reynolds number (see Table 3.1).

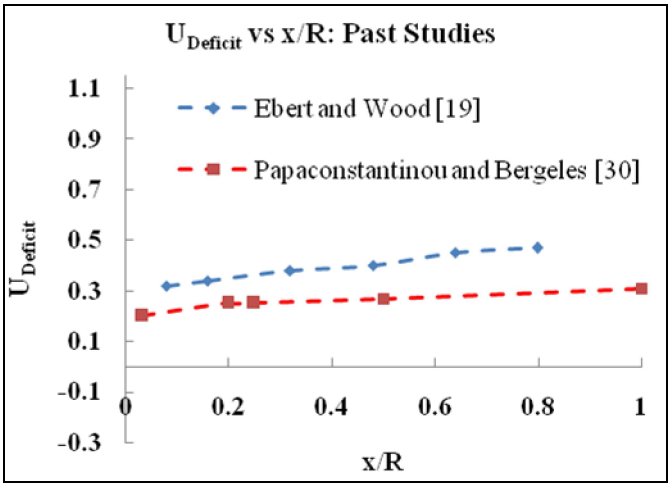

Figure 3.6: Axial velocity deficits in previous studies measured at centerline and $z/R = 0.5$ above hub.

Table 3.1: Experimental parameters in past studies

Reference	λ	$U_{\infty, hub}$ *[m/s]*	I_∞ *[%]*	*Airfoil Section*	*Rotor Diameter [m]*
[19]	2, 4, 6	26.5, 21.4, 17.3	< 0.2	NACA-4418	0.25
[30]	4, 6	Unspecified	< 1	NACA-4412	2.64

Table 3.2: Linear curve fitting through Figure 3.5 (y/R = 0.032) and Figure 3.6

[19]	*0 degrees*		*30 degrees*		*60 degrees*		*[30]*	*Ensemble*	
	50 Hz	*45 Hz*	*50 Hz*	*45 Hz*	*50 Hz*	*45 Hz*		*50 Hz*	*45 Hz*
0.211	0.298	0.367	0.235	0.257	0.286	0.322	**0.099**	0.11	0.080
% Dev.	29.3	74.3	11.3	21.8	35.5	52.6	*% Dev.*	11.1	19.2

Swift-Hook and Højstrup [57] accounted for the relationship between initial velocity ratios and its recovery rate as a function of freestream turbulence intensity. Their findings, spanning from 2 to 6 blade lengths downstream, verify that larger initial deficits are induced by higher turbulence intensities, but decay quicker. Ainslie [58] expanded the discussion to include thrust coefficient, C_T, into an eddy viscosity (ν_T) turbulence model. In stark contrast, his model demonstrated an inverse relationship between initial wake deficit and I_∞ at various C_T; as a matter of fact, correlations with field data suggest a stronger link to thrust coefficient. Judging by the abnormally rapid decrease of the reference phase in Figure 3.3 (a-b), fluid mixing via diffusion of high turbulent fluctuations (computed to be approximately 27%) must be the dominant flow process. However, it is worth alluding to that the two previous studies dealt with full scale turbines operating at higher λ, which affects the distance of maximum wake expansion (and the deficit).

3.1.6 Crosswind Velocity as a Function of Phase

The centerline cross-wind velocity at five downstream locations in the near wake is presented as a function of phase in Figure 3.7. At first glance, all curves appear to be aperiodic throughout

the rotor's rotation, but several outstanding qualities in the flow may be discerned. Wake development of the centerline crosswind component of velocity becomes increasingly positive, while the peak to peak amplitudes decrease. This can be explained as the induced velocity field, by the trailing vortex sheet, loses strength in proportion to the axial distance (i.e. Biot-Savart Law [13]).

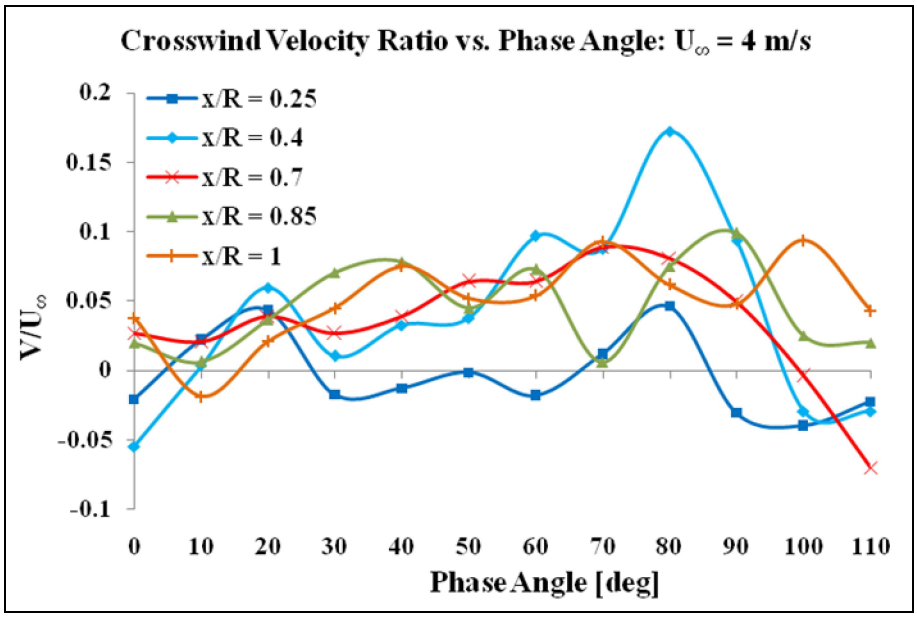

Figure 3.7: Crosswind velocity ratio profiles as a function of phase angle at centerline ($y/R = 0$).

The magnitude of normalized cross-wind velocity observed in the present study is similar to that reported by Medici and Alfredsson [59]. Moreover, the computational study by Hasegawa, Kikuyama, and Imamura [60] conferred a periodicity of 180 degrees (deriving from their 2-bladed rotor); in between, a negative and positive peak in the circumferential velocity were separated by 45 degrees (or ¼ of the period). Fascinatingly enough, this trend continues presently, though not universal at all centerline positions, and is most perceptible at 80 degrees with respect to $x/R = 0.4$, where the peaks occur approximately 30 degrees from one another.

3.2 Measurements at z = 0.135 m

Discussed in Chapter 2, the measurement plane at 0.135 m is lower than the height of the support tower. Thus, flow field measurements are influenced by the blades as well as the tower. That is, the near wake structure is generated by the rotating blades as well as the stationary tower, and their interaction. As mentioned earlier, previous studies mainly focused on the wake structure produced by blades only. Since half of the rotor diameter always lies upstream of the post, it is vital to have a good understanding of the wake flow structure due to the interaction between blade and tower wakes. Furthermore, since this region is closer to the ground, understanding of this flow regime is important for the environmental effects.

3.2.1 Vorticity Patterns

The instantaneous velocity fields at a height of 0.135 m, superimposed by corresponding instantaneous vorticity contours, are presented in Figure 3.8 at various phases. The plots clearly demonstrate that the vortex dynamics at this height is bountiful in variation because of its enormous complexity. With the exception of Figure 3.8 (d), there is no longer an identifiable horseshoe vortex system originating from the blades due to interference by the vertical cylindrical tower. Moving laterally from centerline, it is stipulated that the counter clockwise vorticity is created from the root end of the blade before mixing with the tip vortices.

A general observation is that a greater abundance in negative vorticity (blue contours) remains in the wake when the blades rotate away from the tower, such as the case in Figure 3.8 (a-c). A meaningful hypothesis, drawn from Palau-Salvador *et al's* [61] extensive research on the highly unsteady, three dimensional wake of short cylinders, is to assume that the two systems of trailing vortices adopt opposing signs, where positive vorticity is being suppressed. Of course, the

problem is compounded by shedding on the lateral faces, edge of the cylinder's free end, and from the blades themselves.

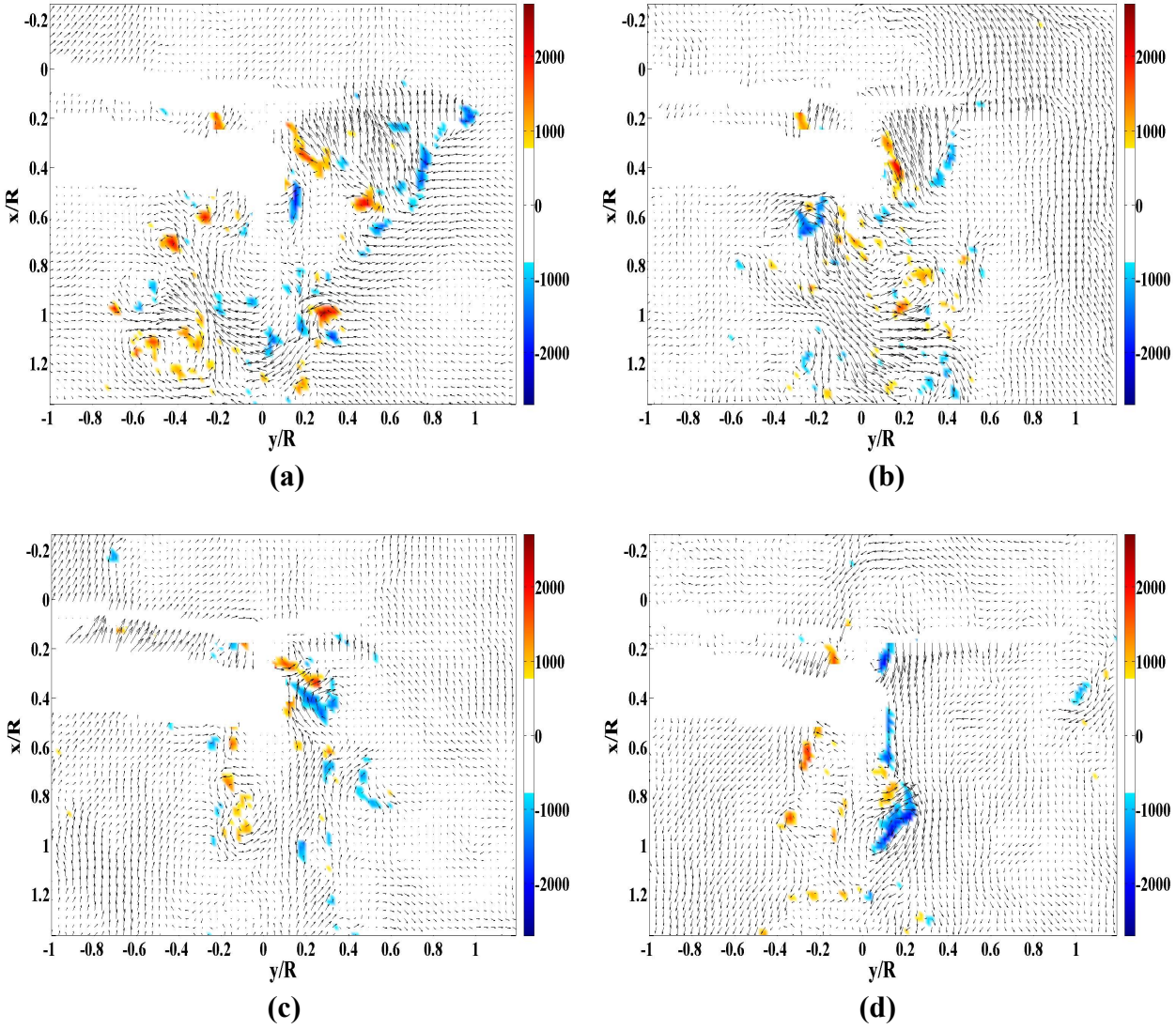

Figure 3.8: Instantaneous velocity vector maps superimposed on contours of instantaneous vorticity (Hz) at a height of 0.135 m at free stream velocity of 4 m/s; ccw rotation is red, cw rotation is blue. The plots are at phases, **(a)** 110° **(b)** 90° **(c)** 60° **(d)** 30°.

3.2.2 Ensemble Averaged Velocity

The contour plots of ensemble-averaged streamwise and crosswind velocity components at the freestream velocity of 4 m/s are shown in Figure 3.9. The influence of the post on the mean

velocity field is clearly evident in the plots. The wake of the cylinder in Figure 3.9 (a) remains unaffected by the averaging process and does appear to be axisymmetric about $y/R = 0$ with its streamwise extent beyond one blade length. Figure 3.9 (b) shows that the mean crosswind velocity changes its direction as it passes the tower, which could be due to the flow separation caused by the tower wake.

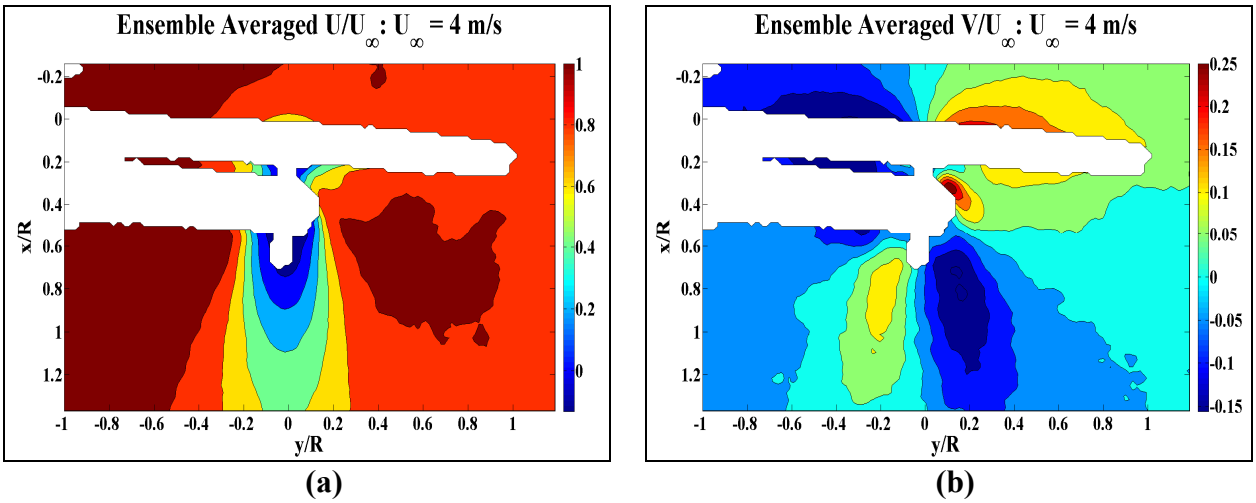

Figure 3.9: Ensemble averaged contour plots taken at a laser sheet height of 0.135 m and $U_\infty = 4$ m/s **(a)** Streamwise velocity ratio **(b)** Crosswind velocity ratio.

3.2.3 Phase Averaged Streamwise Velocity

Phase-averaged contours of the normalized mean streamwise velocity at different phases are plotted in Figure 3.10 at the free stream velocity of 4 m/s. A much different flow pattern is revealed, especially in the region $0.5 \leq x/R \leq 1.2$ and $-0.3 \leq y/R \leq 0.3$ when compared to those at $z = 0.185$ m. Introduction of a second blunt object - the cylindrical tower - is the source for the major change. Similar to the observation at 0.185 m, the plots show flow acceleration in the region bounded between two blades. The interaction of the wakes produced by the blade with that of the tower, when both are aligned, is clearly depicted at the phase of 30 degrees. There is an evident shrinking in the width of the tower wake, which stems from the streamlines diverging

less in the presence of the blade planform surface. Another interesting observation is that when the blade is not aligned with the tower, the wake produced by the blade is sucked in towards the tower (see Figure 3.10, 60 and 90 degrees). One plausible explanation for this trend could be that the low pressure region generated by the tower induces a strong suction force.

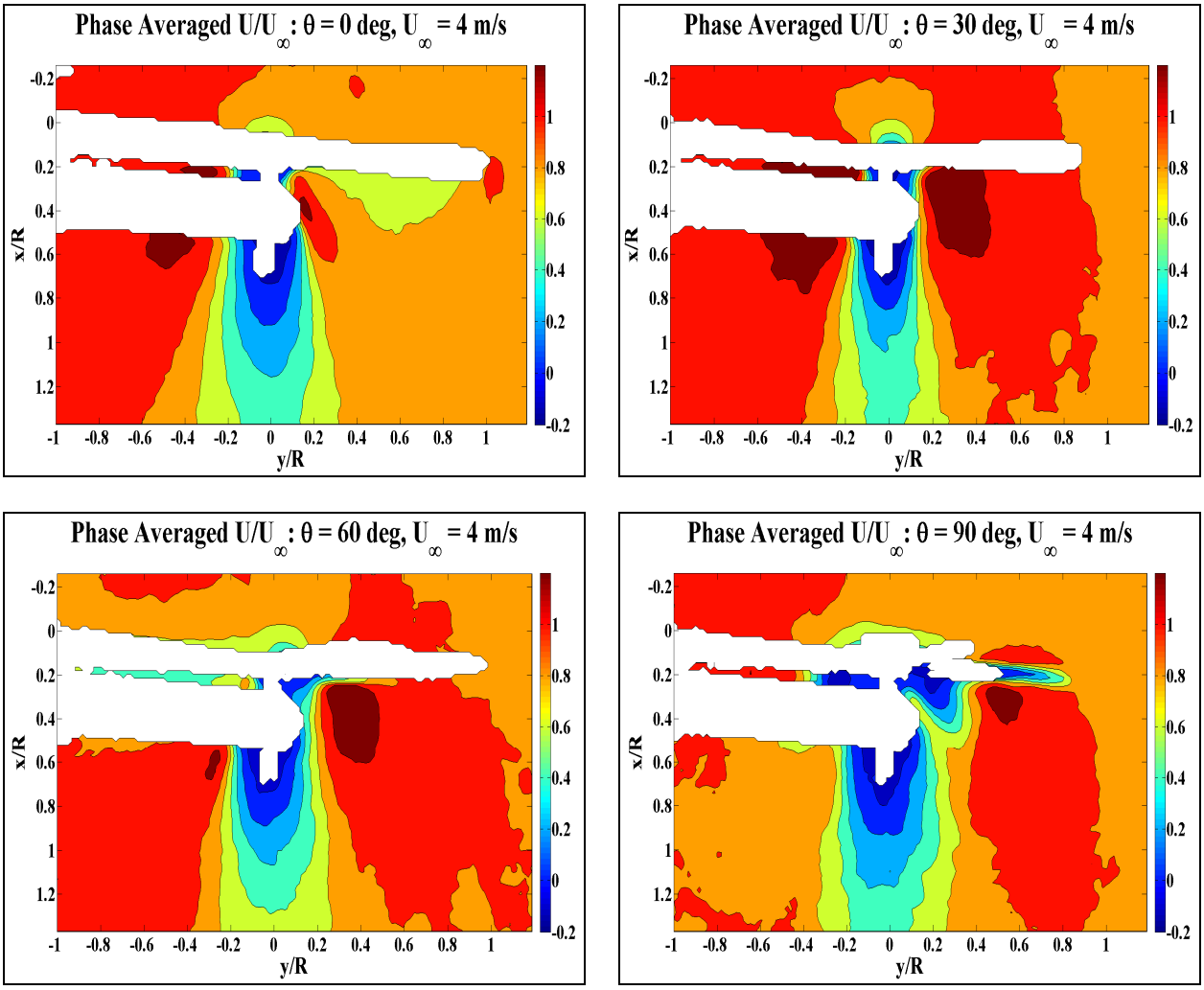

Figure 3.10: Phase averaged contours of streamwise velocity normalized by U_∞ at 0.135 m for wind speed of 4 m/s.

3.2.4 Phase Averaged Crosswind Velocity

With the rotor intersecting the light sheet at this specific height, the incident flow is deflected by a relatively larger cross section – the blade root. Incidentally, it accounts for the augmented

phase-averaged crosswind velocity ratios shown in Figure 3.11, if paired against Figure 3.4. This transpires because the flow senses a relatively smaller area to negotiate and must convect faster laterally; it is simply an application of the continuity equation (Eq. 1.1) in the y-direction. Immediately behind the cylinder, two regions of opposite crosswind velocities is a matter of the streamlines opening (accelerating on the forward face of the tower) and closing (deceleration by adverse pressure gradient on rearward side).

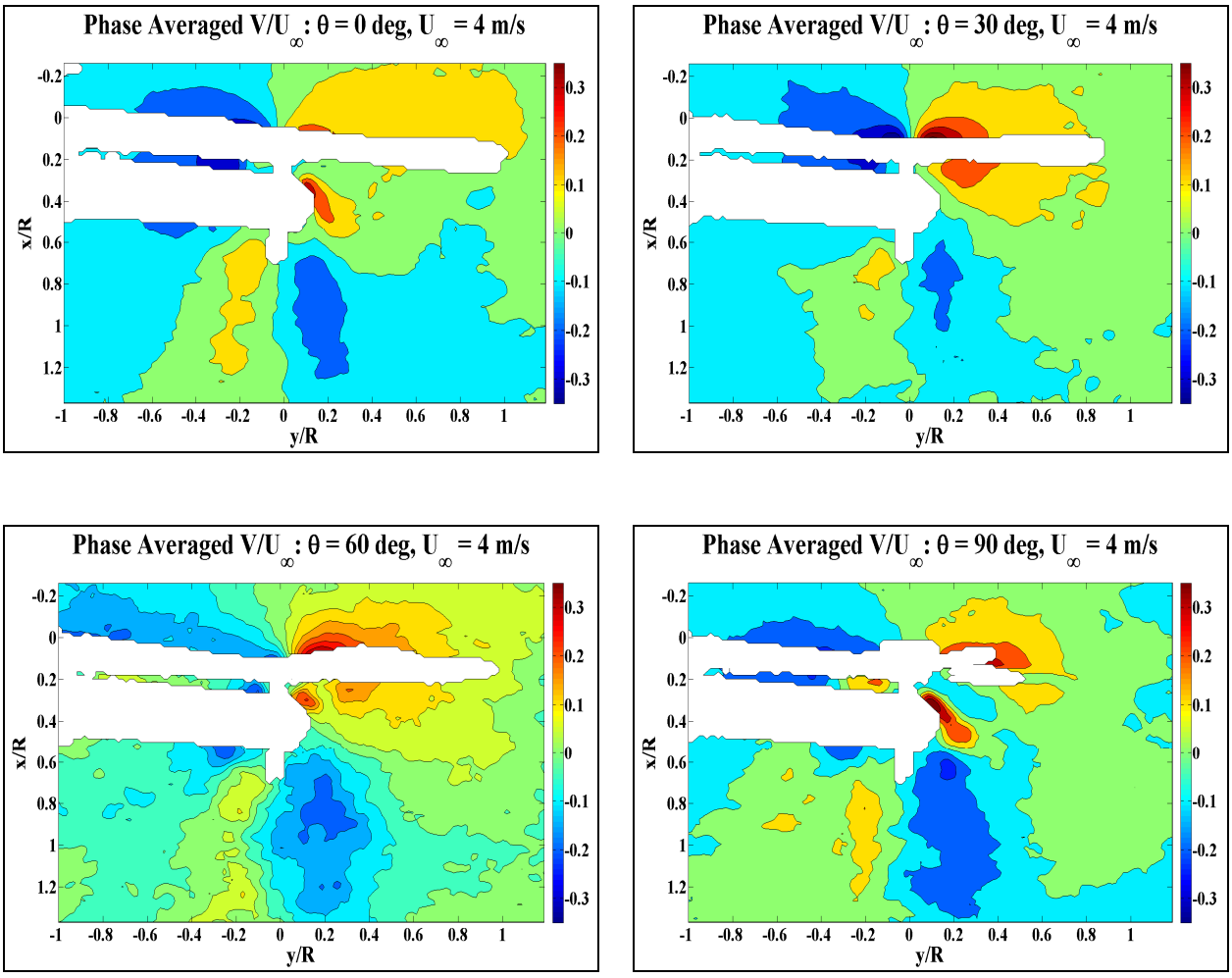

Figure 3.11: Phase averaged contours of crosswind velocity normalized by U_∞ at 0.135 m for wind speed of 4 m/s.

3.2.5 Streamwise Velocity Deficit

The streamwise velocity deficit at different crosswind locations is presented in Figure 3.12 at two free stream velocities. The wake deficit plots close to the centerline, at y/R = 0.034, show that the weakening of streamwise velocity deficit is more gradual in the cylinder's wake than that caused from a blade at both wind speeds. Since the cylinder is a non-lifting body, it is surmised that the lack of circulation inhibits the generation of an induced flow field, leading to moderately lower turbulence and a decrease in fluid mixing. Although the selected phases behave similarly, those with a blade situated in front of the post are subjected to a lower deficit (i.e. 30 degrees).

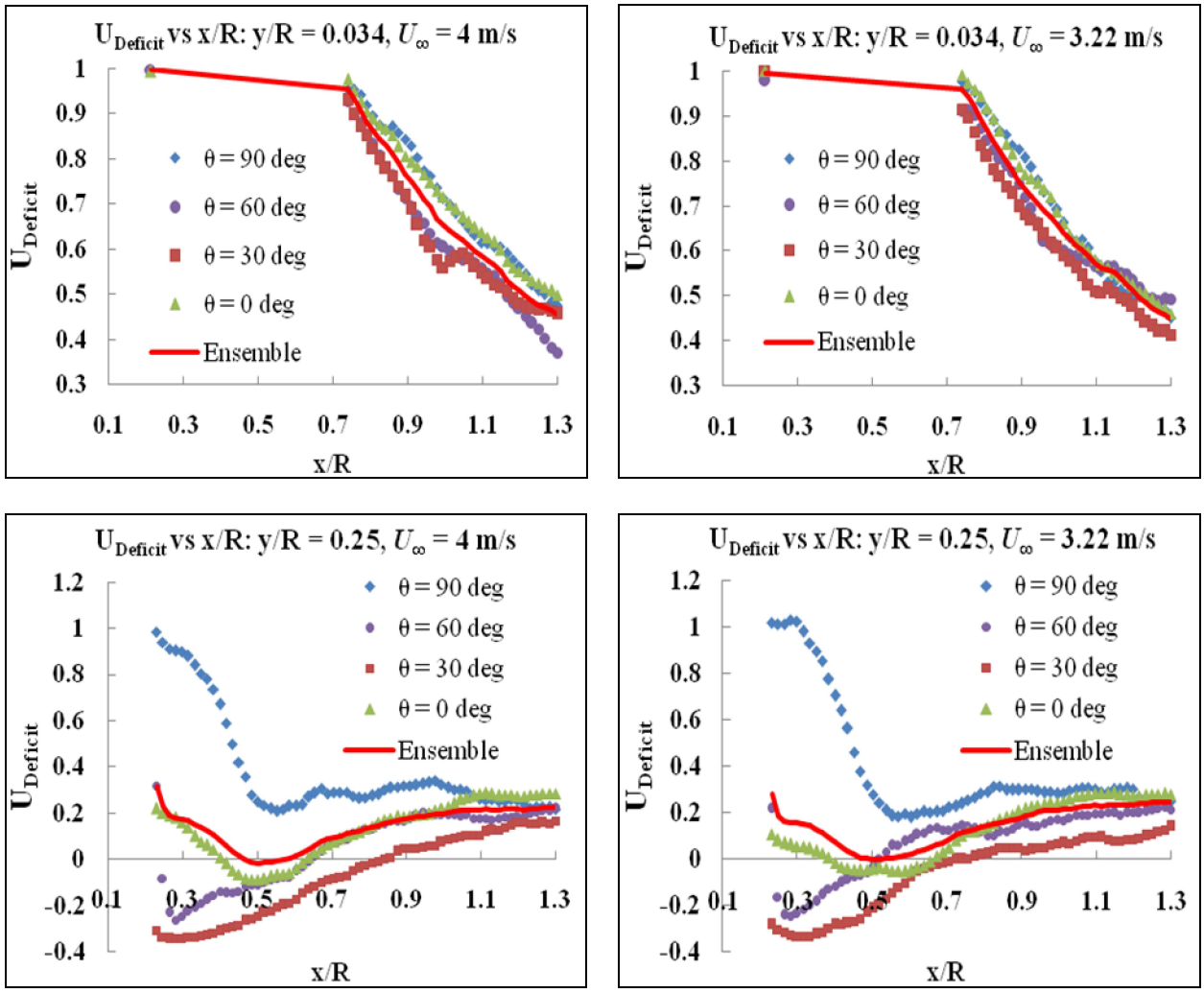

Figure 3.12: Phase averaged streamwise velocity deficit at spanwise distances of y/R = 0.034 and 0.25 for a height of 0.135 m, at wind speeds of 4 m/s and 3.22 m/s.

As moving away from the centerline, the effect of the tower wake decreases and the typical streamwise velocity deficit due to blades become prominent as depicted in the spanwise location at the quarter blade length from the centerline (y/R = 0.25). The results show that the velocity deficit at the phase of 90 degrees is significantly different from other phases. The blade position at this phase (see Figure 2.17) indicates that the flow has higher momentum loss due to the presence of blade that almost coincides with this spanwise location. The lowest momentum losses are at phases of 30 and 60 degrees. These cross-stream locations are positioned in between two blades (see Figure 2.17); therefore, as mentioned earlier, the flow accelerates and causes a negative deficit. However, once the flow enters the flow regime of the cylinder, the deficit becomes positive. Results also show that the ensemble averaged velocity deficit profile is similar to that at the phase of 0 degrees.

3.2.6 Development of Crosswind Velocity

The spanwise distribution of normalized crosswind velocity at two downstream locations at different phases is shown in Figure 3.13 for U_∞ = 4 m/s and 3.22 m/s. The flow in the wake is expected to move with a positive value (i.e. left to right flow), yet both signs appear irrespective of phase or ensemble averaged schemes. Granted, flow direction and its magnitude in the region set by $-0.3 < y/R < 0.3$ is strongly dictated by the support tower. As the wake develops, a decrease of relative time is spent on being negative in the left hand quadrant ($y/R < 0$), and likewise for positive values in the right hand quadrant ($y/R > 0$). Furthermore, in the case of the ensemble averaged profile, the separation in magnitude in the peak velocities becomes larger as the tower wake expands downwind. Farther into the wake, the flow appears to have less spatial variation between phases.

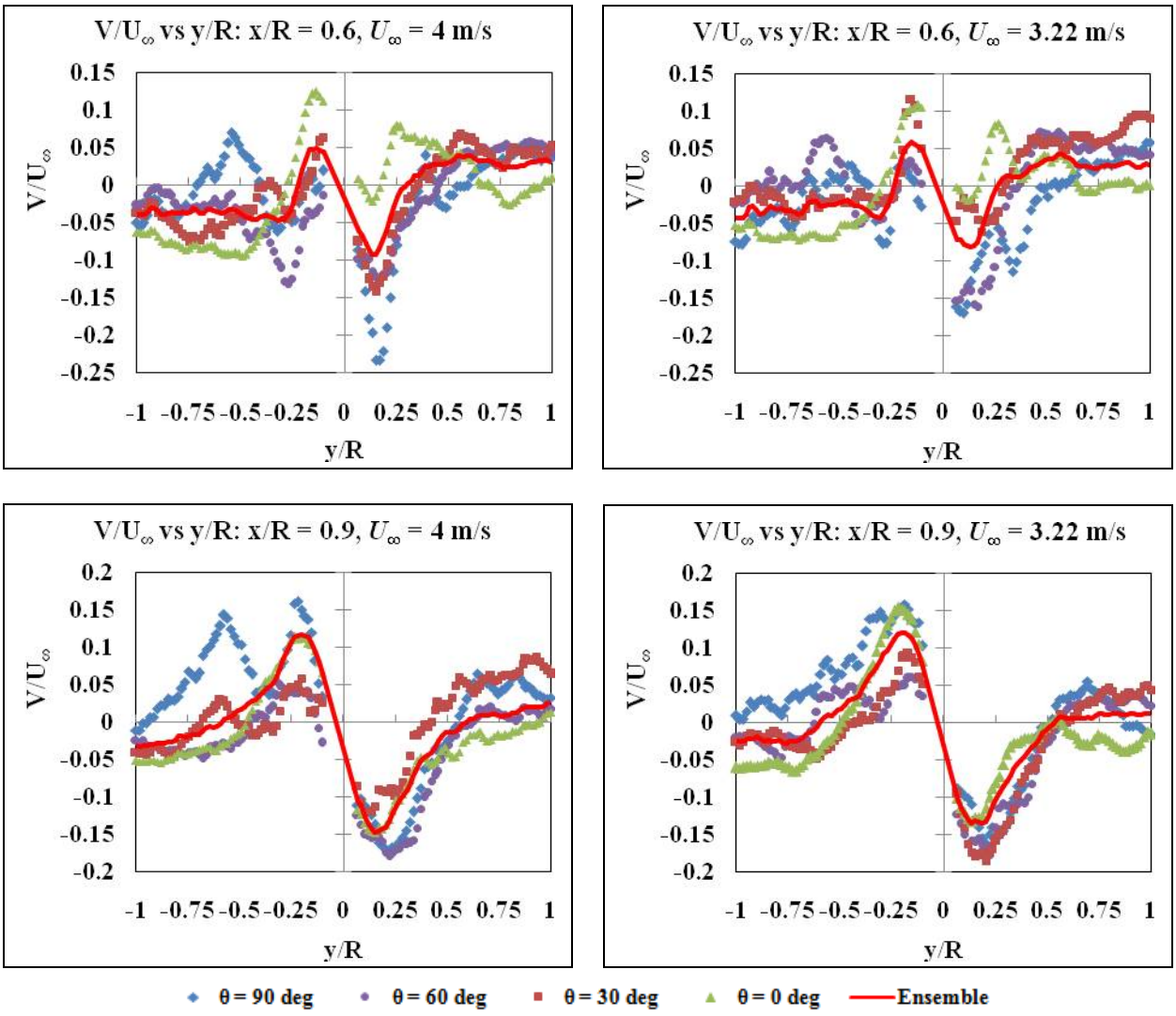

Figure 3.13: Spanwise distribution of normalized phase averaged crosswind velocity at *x/R* = 0.6 and 0.9 for a height of 0.135 m. Wind speeds are 4 m/s and 3.22 m/s, respectively.

3.3 Measurements at z = 0.05 m

The height 0.05 m is located underneath the rotor diameter. Thus, the flow is primarily influenced by the tower. Since the blades were rotating above this location, they did not interfere with the light sheet. As a result, it was not possible to compute blade phases. Thus, only ensemble averaged results are presented at this location. The contours of ensemble averaged streamwise and cross-wind velocities are presented in Figure 3.14. The results show some weak

influence of the rotor on the wake at this height, however, the wake is predominantly produced by the tower.

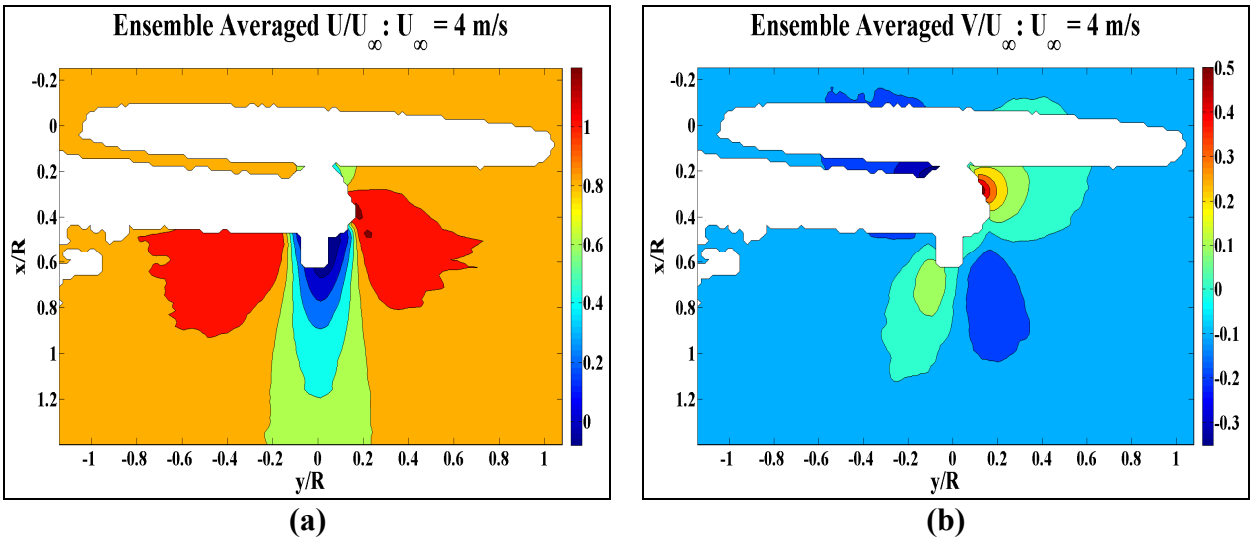

(a) **(b)**

Figure 3.14: Ensemble averaged contour plots taken at a height of 0.05 m and U_∞ = 4 m/s **(a)** Streamwise velocity ratio **(b)** Crosswind velocity ratio

Figure 3.15 provides spanwise distributions of normalized ensemble averaged streamwise and crosswind velocities at axial locations corresponding to x/R = 0.6, 0.9, and 1.3. The data at the heights of 0.185 m and 0.135 m are also plotted for comparison. From the plots of normalized streamwise velocity, profiles at the bottom two heights demonstrate Gaussian-like behaviour in their momentum losses, but the lone tower wake along the centerline recovers more rapidly, in addition to having a narrower trough. The tail ends in the crosswind velocity remain negative at all three axial distances at a height of 0.05 m. This is in stark contrast to the 0.135 m profile, where the rotor induced flow tends to force the air to move with a positive crosswind velocity. Unclear is how the peak crosswind velocity at x/R = 1.3, in the second quadrant, destabilized from a positive to negative structure.

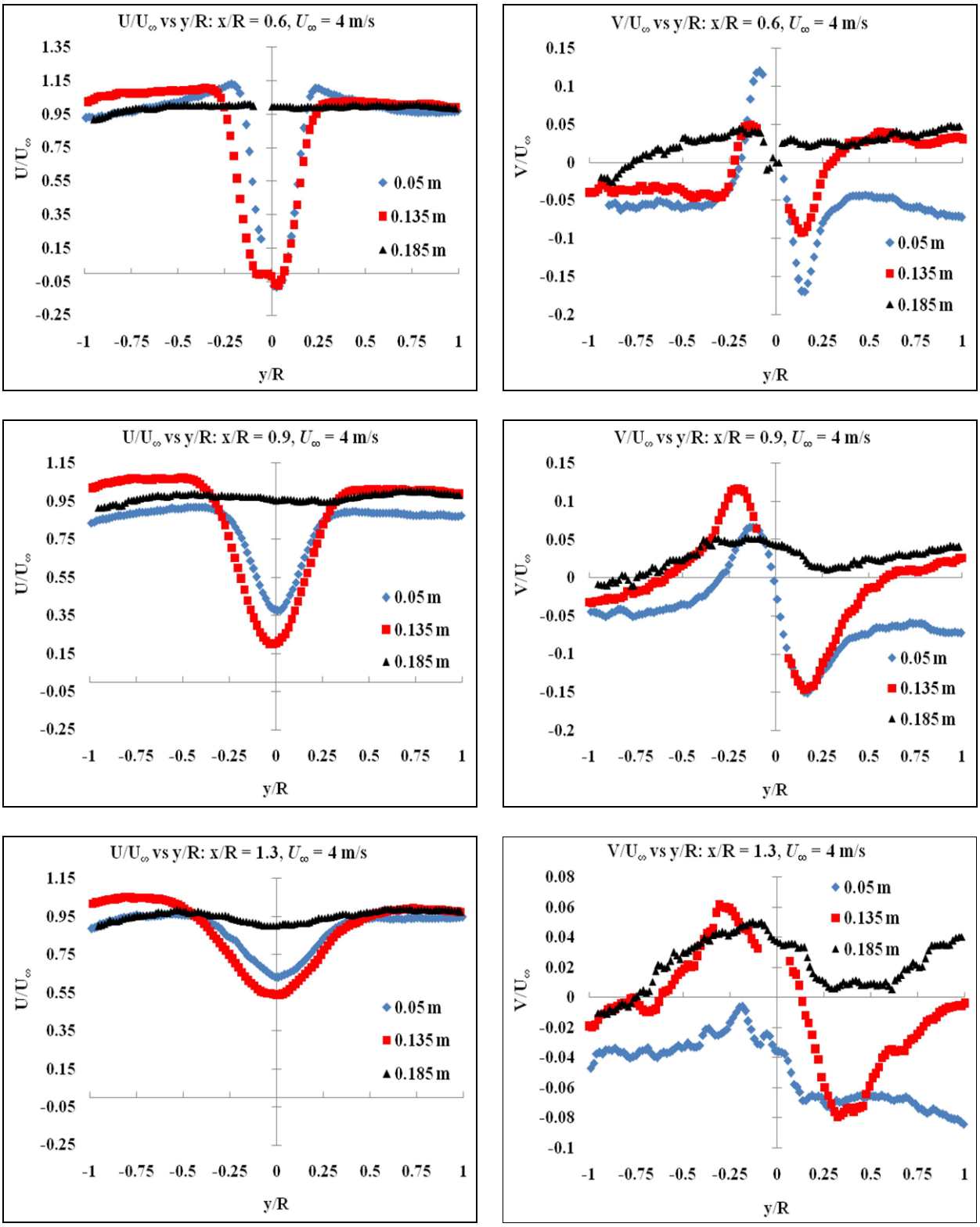

Figure 3.15: Spanwise distribution of ensemble averaged normalized velocities at *x/R* = 0.6, 0.9, and 1.3 for all 3 measurement heights. **(left)** Streamwise **(right)** Crosswind.

3.4 Conclusion

The present chapter focused on the mean flow at heights of 0.185 m, 0.135 m, and 0.05 m. Both ensemble and phase averaged streamwise and crosswind velocities were studied. Some main conclusions drawn from this analysis are presented below.

3.4.1 Streamwise Velocity

At a height of 0.185 m, where the wake was composed solely of the rotor's induced flow, the phase averaged profiles of streamwise velocity exhibited a region of reduced momentum, in between adjacent zones of accelerated flow. The sole exception to the abovementioned behaviour occurred with the appearance of two blade tips, in which the accelerated flow was entrained by lower momentum flow. Due to unsteadiness in the wake, the structure of the accelerated flow was not uniform across phases. It was observed that the centerline streamwise velocity deficit, for both ensemble and phase averaged profiles, decayed linearly due to wake expansion.

At lower heights, the combined influence of the tandem wakes from the cylindrical support tower and the rotor radically altered the nature of the flow dynamics. The pressure field generated about the tower resulted in suction of the blade flow that advected within its vicinity. In addition, the spanwise distribution of the velocity deficit was determined to be Gaussian, with a lower decay rate than the rotor wake in isolation. Only an analysis of the turbulence, in the subsequent chapter, will provide a sufficient explanation.

3.4.2 Crosswind Velocity

A weak periodic pattern in the crosswind velocity, at a height of 0.185 m, was noted between phases. In particular, the peak to peak amplitudes were separated by a quarter of the periodicity,

or 30 degrees. The centerline flow direction was predominantly positive, which indicated that the flow rotated in an opposite sense to that of the rotor.

At the intermediate measurement plane, the effect of the rotor became obvious. Since individual blades acted as stagnation surfaces, the flow upstream deflected accordingly, but had a bias towards achieving positive values in the wake. The tower wake, on its own, did not display this type of activity.

Chapter 4: Quantification of Turbulent Flow Behaviour in the Near-Wake Region

Quantification of the turbulent flow behaviour in the near-wake region is important for the better understanding of the near-wake flow development, improvements in modelling wind farms and their power capacitites, and proper management of dynamic loads, including fatigue stress. Definitions of turbulence, amongst other things, are typically along the lines of being stochastic and having organized motions (in the form of eddies) that exist across a continuum of scales. As a result, this chapter employs both probabilistic and spectral techniques in its analysis and description of turbulent velocity field.

Attention is firstly honed on turbulent intensities ($I_{u,v}$) because they characterize the width of a random distribution. Indications of directional transfer of the energy are treated by the Reynolds stress. Subsequently, one-dimensional wave number spectra are presented, in order to identify energy contributions across the range of resolved length scales. Like the preceding chapter on mean velocities, turbulent flow quantities are visualized initially with contour plots before proceeding meticulously with graphical profiles of selected phase averaged effects.

4.1 Measurements at z = 0.185 m

4.1.1 Ensemble Averaged Turbulence Intensity

The ensemble averaged contour plots of turbulence intensity, which is defined by Eq. 1.15 ($I_{u_1} = I_u; I_{u_2} = I_v$), are presented in Figure 4.1 for wind speed of 4 m/s. Figure 4.1 (a), shows that the streamwise component of turbulent intensity is significantly enhanced in the near wake of the turbine blades. Turbulence intensity, as high as 55 percent, are observed in the immediate wake region. This enhancement of turbulence is attributed to the trailing and shed vortices. This

enhanced turbulence region, which is symmetric about the centerline (y/R = 0), extends up to one rotor diameter downstream of the turbine; however, its radial width (which is equal to the rotor diameter immediately downstream of the turbine) decreases with downstream distance. The plot also shows that the ambient level of I_u is relatively high. Such a high level of background turbulence is in the range of conditions observed in the field.

Contrary to I_u, the crosswind turbulence intensity profile (I_v) in Figure 4.1 (b), is non-uniform upwind of the rotor, and displays less variation within the wake. A centralized core region of high crosswind turbulent intensity of about 25 percent is present, which extends to about one rotor diameter downstream; however, its width is significantly less than that of streamwise turbulent intensity (see Figure 4.1a).

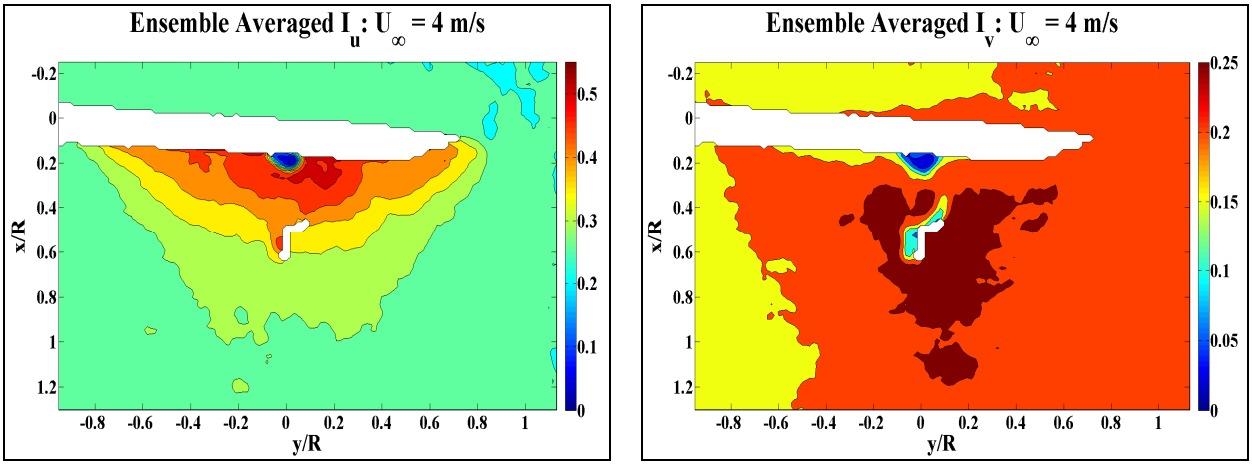

(a) **(b)**

Figure 4.1: Ensemble averaged turbulence intensity contour plots **(a)** Streamwise direction **(b)** Crosswind direction.

4.1.2 Phase Averaged Streamwise Turbulence Intensity

Viewing the structure of turbulent motions at discrete phases is important to have a deeper insight into the flow structure, which smoothens out due to ensemble averaging. Figure 4.2 shows turbulent velocity fields at four selected phases of 0, 30, 60, and 90 degrees. The plots clearly demonstrate the vortex shedding off the blades (double core) at all presented phases,

which indicates that the turbulence enhancement in the near-wake region is contributed by the localized high turbulence intensity patches generated by vortex shedding. These high turbulence patches then diffuse in the near-wake as they advect downstream, disappearing by x/R = 0.8. Another interesting observation is that these patches diffuse towards the centerline. Furthermore, it is not a coincidence that the contours in Figure 3.1, illustrating instantaneous ζ, correspond almost identically to the patterns observed for I_u; mathematical formulations are introduced in upcoming paragraphs to help explain how turbulence is produced and destroyed in the wake.

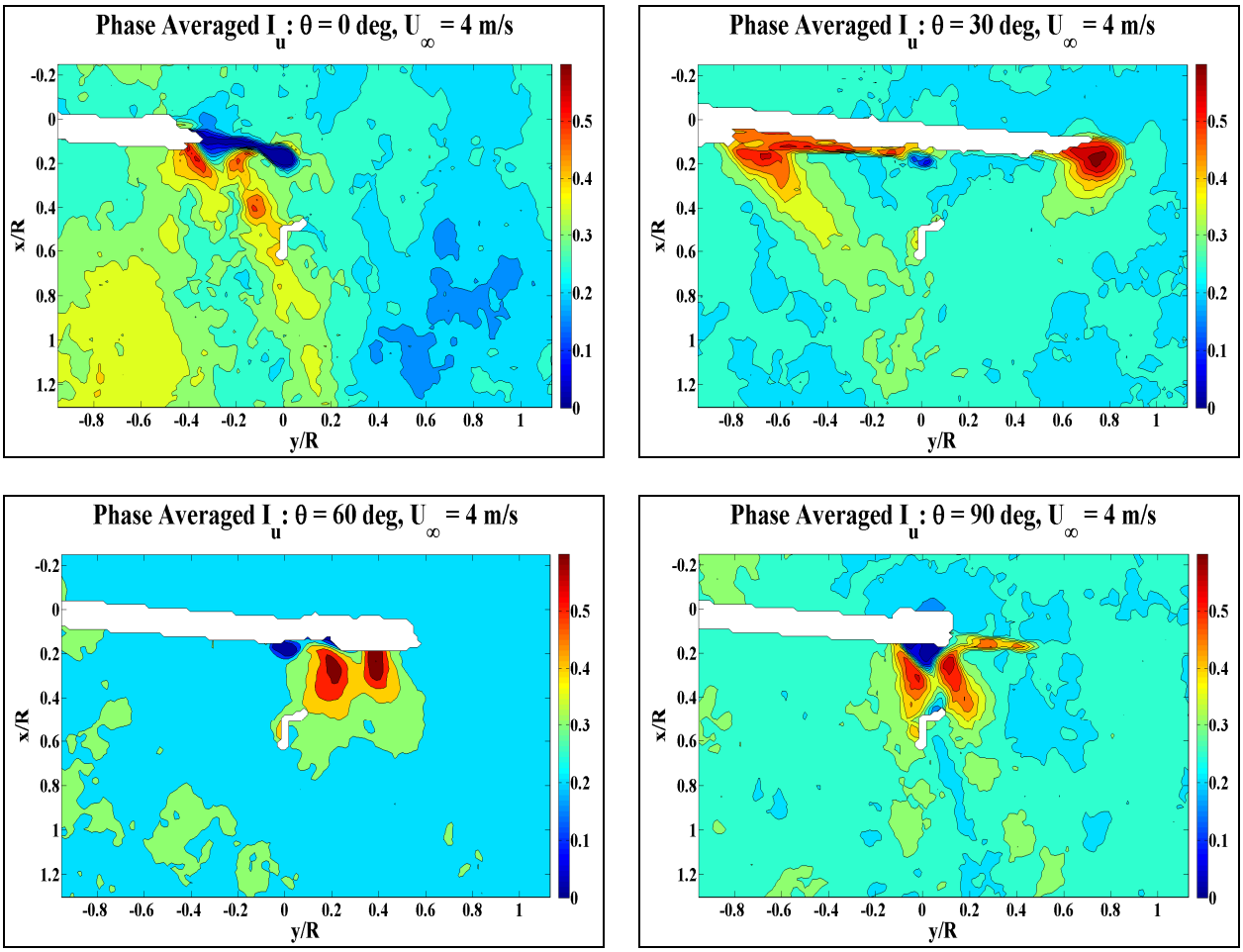

Figure 4.2: Phase averaged contour plots of streamwise turbulence intensity.

Figure 4.3 presents the axial profiles of I_u (both ensemble and selected phase averaged) at different crosswind locations (y/R = -0.4, 0.032, and 0.4) at two U_∞. A reminder that gaps in

some profiles are due to regions of poor quality data. At crosswind locations coinciding with the pair of vortex cores, rotor generated turbulence increases I_∞ values varying between 20 to 30 percent to those approaching 60 percent (0 degrees at y/R = -0.4) and beyond (60 degrees at y/R = 0.4) in the near-wake. Yet, after achieving respective maxima, both profiles decline steeply over a short distance of 0.25 R. Ensemble averaged curves also display a drop in turbulence, after peaking, but remain above freestream levels even at x/R = 1.3. Phases away from the vicinity of the local turbulence exhibit minor fluctuations around freestream turbulent intensity (I_∞), while certain phases can display higher peak values than the ensemble curve (60 degrees at y/R = 0.4).

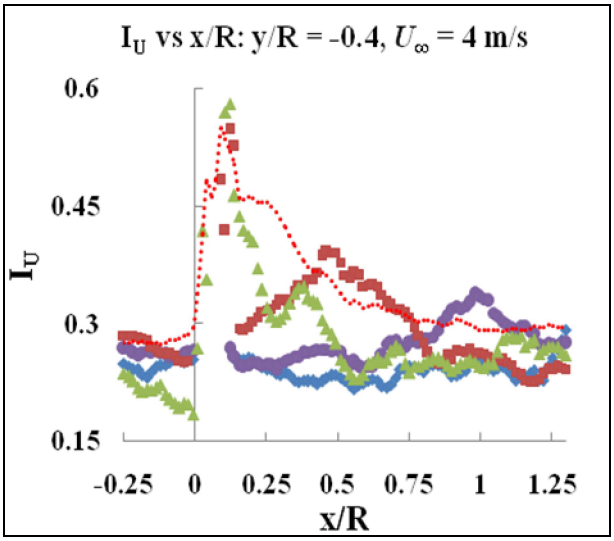

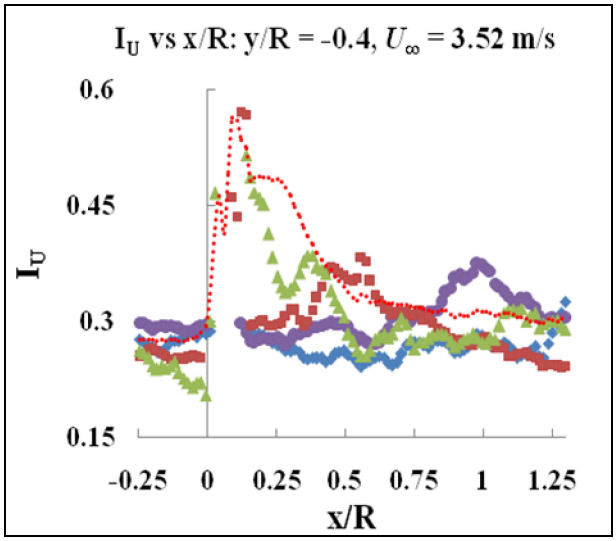

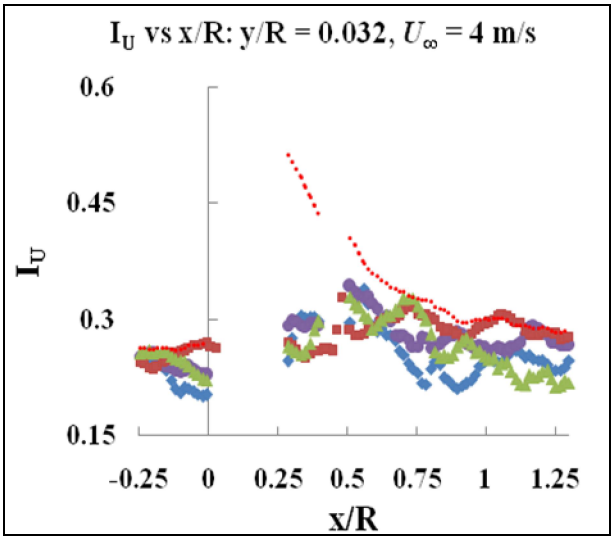

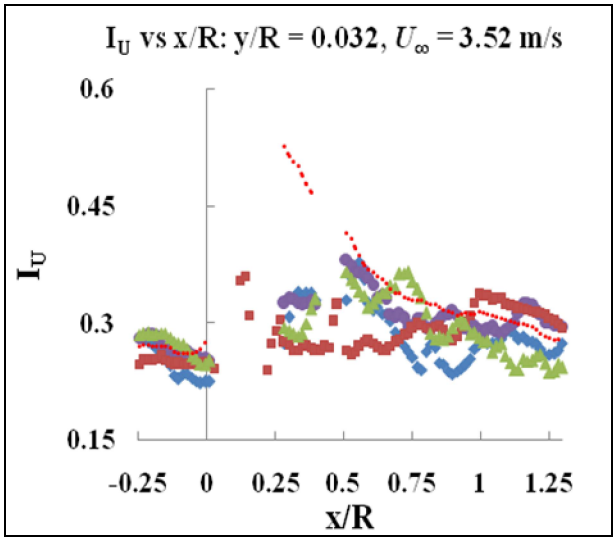

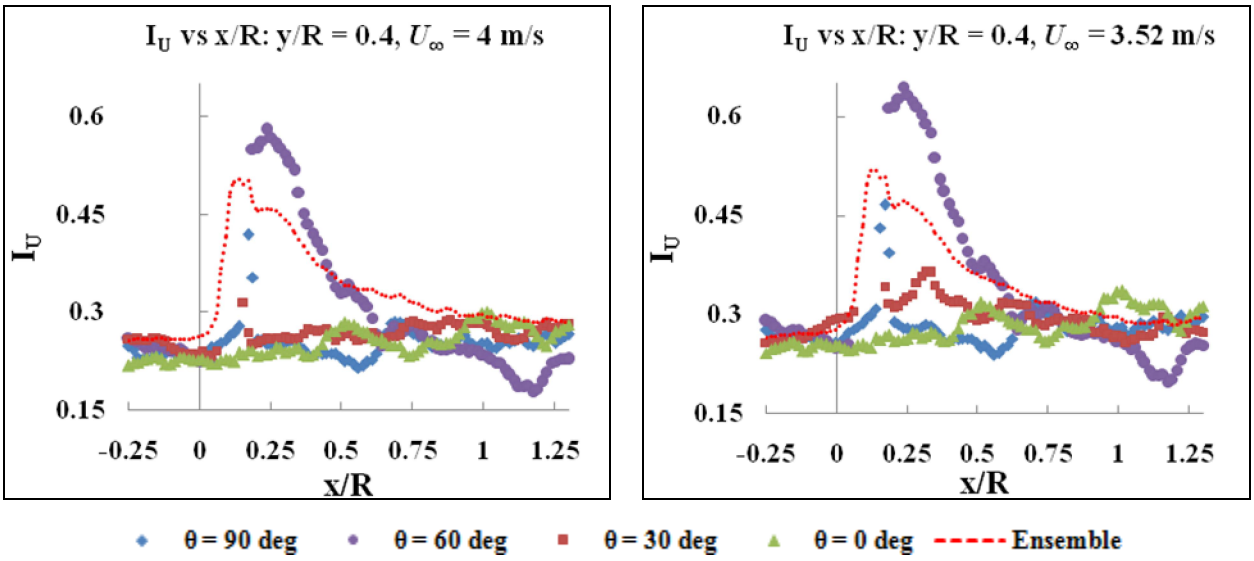

Figure 4.3: Comparison of streamwise turbulence intensity as a function of wake distance for three crosswind locations (y/R) of -0.4, 0.032 and 0.4.

Ainslie [55] mentioned that large scale eddies, originating at the wake boundaries (i.e. shear layer materializes from velocity differences), spread into the interior and eventually meet the centerline several rotor diameters downstream. Concurrently, I_∞ strives to diffuse the energy from the shear layer into the core, propagating monotonic decay of $U_{Deficit}$. Helmis *et al* [31] report that lower U_∞ and higher I_∞ are ripe conditions for smaller velocity deficits, which concur with Figure 3.5's findings. One can further understand the connection involving the mean flow and turbulence through the RANS (Reynolds Averaged Navier Stokes) equation [35],

$$\frac{\partial \langle U_i \rangle}{\partial t} + \langle U_j \rangle \frac{\partial \langle U_i \rangle}{\partial x_j} = -\frac{1}{\rho}\frac{\partial}{\partial x_j}\left[\langle p \rangle \delta_{ij} - 2\mu \langle S_{ij} \rangle + \rho \langle u_i u_j \rangle\right]. \qquad 4.1$$

Terms on the right hand side of Eq. 4.1 denote transport of mean momentum by pressure gradient, viscosity, and turbulent fluctuations, respectively. Evidently, $-\rho\langle u_i u_j \rangle$, or Reynolds stress, derives from the advective term in Eq. 1.2 via Reynolds decomposition and taking its average. Hence, it is the most essential of the three terms because it performs the fluid mixing between the mean and turbulent components of the velocity.

4.1.3 Added Streamwise Turbulence Intensity

One model normally employed for its simple yet holistic approach to quantify the heightened streamwise turbulence intensity in the wake is expressed by [14],

$$I_u^+ = \sqrt{I_{u,wake}^2 - I_\infty^2}\ . \tag{4.2}$$

Specifically, Eq. 4.2 is plotted for both sets of ensemble averaged data, in conjunction to being utilized to transcribe trend lines from [30], in Figure 4.4 - a comparative diagram of I_u^+ as a function of axial distance. Also included in the plot are rearward extrapolated results from both [34] and [41] (authors focused their analysis on far-wake dynamics), and a semi-empirical relationship introduced by Crespo and Hernandez [62] which is described by the following equation,

$$I_u^+ = 0.73 a^{0.8325} I_\infty^{0.0325} \left(\frac{x}{D}\right)^{-0.32}, \tag{4.3}$$
$$5 < x/D < 15;\ 0.07 < I_\infty < 0.14;\ 0.1 < a < 0.4,$$

where *x/D* represents wake distance non-dimensionalized by the rotor diameter; *a* is the axial induction factor, and the two dominate its decay. Though direct correlations of I_u^+ in the near wake have been debated previously by Crespo and Hernandez [63], relations therewithin fail to account for I_∞'s effect and spatial decay. Thus, improved analytical models of I_u^+ in the near wake should be calibrated with an emphasis towards I_∞ (recommended by measuring both upstream and downstream turbulence over a wide array of freestream conditions); of course, the λ-regime in which the turbine operates will reflect heavily on tip vortex stability and the mixing process that ensues.

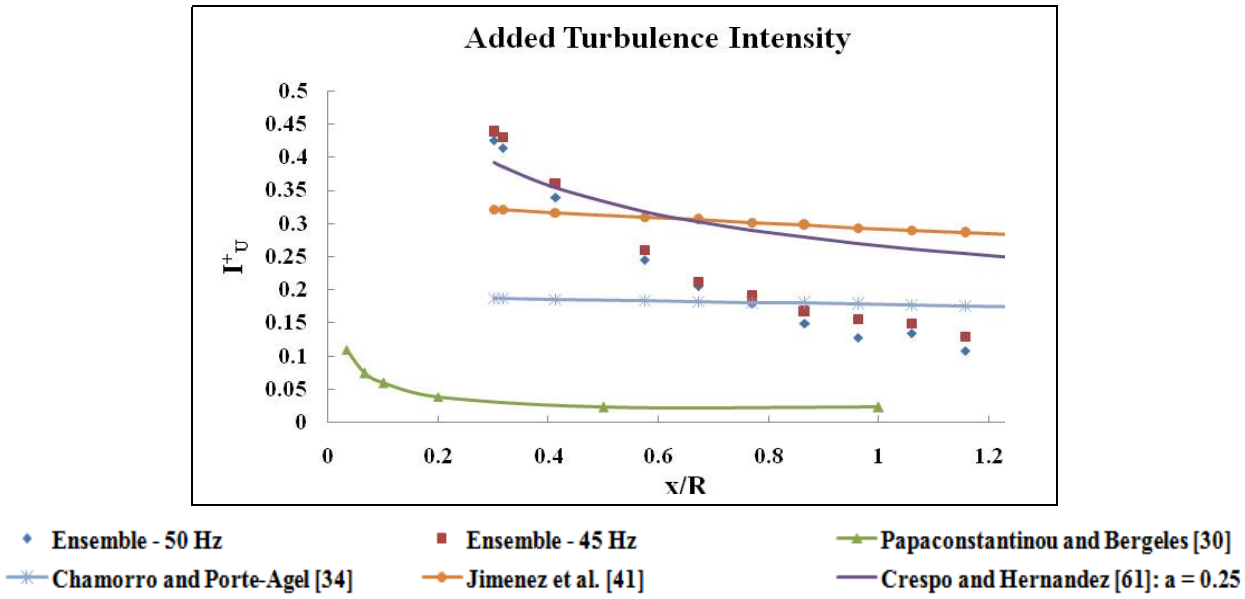

Figure 4.4: Level of increased turbulence intensity as a function of axial distance. Ensemble curves correspond to a measurement plane at centerline.

The results in Figure 4.4 show that the values of added turbulent intensity closer to the rotor are comparable to that predicted by Eq. 4.3. However, the subsequent decay of I_u^+ in the present study is found to be faster than that predicted by Eq. 4.3. The results from Chamorro and Porte-Agel [34] and Jimenez *et al* [41] show no appreicable decay of I_u^+ in the near-wake region, which does not seem physcially consistent. Also, both studies show significant differences in the magnitudes of I_u^+. The results of Papaconstantinou and Bergeles [30] show a decay of I_u^+, however, most of the decay occurred immediately behind the rotor ($x/R < 0.2$).

Many factors can simultaneosuly impact I_u^+, some of which are summarized in Table 4.1. Beginning first with the ensemble averaged profiles, it is highly likely that a bulk value of 27 percent for I_∞ causes a faster decay. Compare this to the experimental work in [34]: identical rotor size and similarly loaded, but the oncoming flow is logarithmic (typical of full scale flows) and has much lower I_∞. A logarithmic flow causes a non-axisymmetric distribution of added

turbulence, peaking at the shear layer. In fact, turbulence intensity is shown to decrease below hub height due to the tower shadow and ground effects. Field turbines, in [41] and [62], must contend with altered boundary layer development over the blades (affecting stall behaviour), higher inertial forces, and unsteady wind directions (triggers wake meandering). Additionally, there are no guarantees that the extrapolated profiles succeed in predicting the actual near wake behaviour (extrapolated backwards from 3 *D* and 2.5 *D*, respectively for [34] and [41]).

Table 4.1: Differences in flow and turbine parameters

Reference	***Type of Incident Flow***	***Rotor Diameter [m]***	λ	$I_{\infty,\, z/R\, =\, 0.5}$ ***[%]***
Ensemble	Uniform	0.15	3.47, 4.24	27
[30]	Uniform	2.64	4, 6	1
[34]	Logarithmic	0.15	4.2, 4.4	10
[41]	Logarithmic	30	4.7-6.7	11
[58]	Logarithmic	Various	Various	7-14

4.1.4 Phase Averaged Crosswind Turbulence Intensity

The contour plots of phase-averaged crosswind turbulent intensity (I_v) at selected phases are presented in Figure 4.5. The vortex shedding off the blades at all given phases is clearly evident in the plots. In contrast to the double core arrangement in the I_u plots, Figure 4.5 illustrates that only a single core of high crosswind turbulence intensity is present. At each of the displayed phases, the core weakens quickly, but permeates deep into the near-wake, an action aided by the entrained column of diffused fluid. Width of the affected region seems to be on par with the streamwise component, measuring approximately 0.4 *R*. At certain phases (0 and 90 degrees), there are areas of low turbulence that flank the diffused column, a by-product of the averaging technique.

The axial profiles of phase and ensemble averaged I_v are depicted in Figure 4.6 at different crosswind locations (y/R = -0.4, 0.032, and 0.4) at two U_∞. The plots show that across the wake,

the ensemble averaged data contains a relatively wide plateau, hovering around 30 percent. The turbulence dissipates to freestream values away from the core by the time the flow reaches x/R = 1.3, while centerline values continue to persist strongly. Similar to I_u, the strength of an I_v core in phase averaged data is certainly more intense than ensemble averaged, typified by 90 degrees at centerline. Maximum peak value reaches 45 percent, or roughly 70 to 75 percent of $I_{u,max}$ from Figure 4.3. Quite fascinating is that the peaks across the wake occur in the neighbourhood of x/R = 0.6, and the phase averaged values in the wake also remain above ambient values.

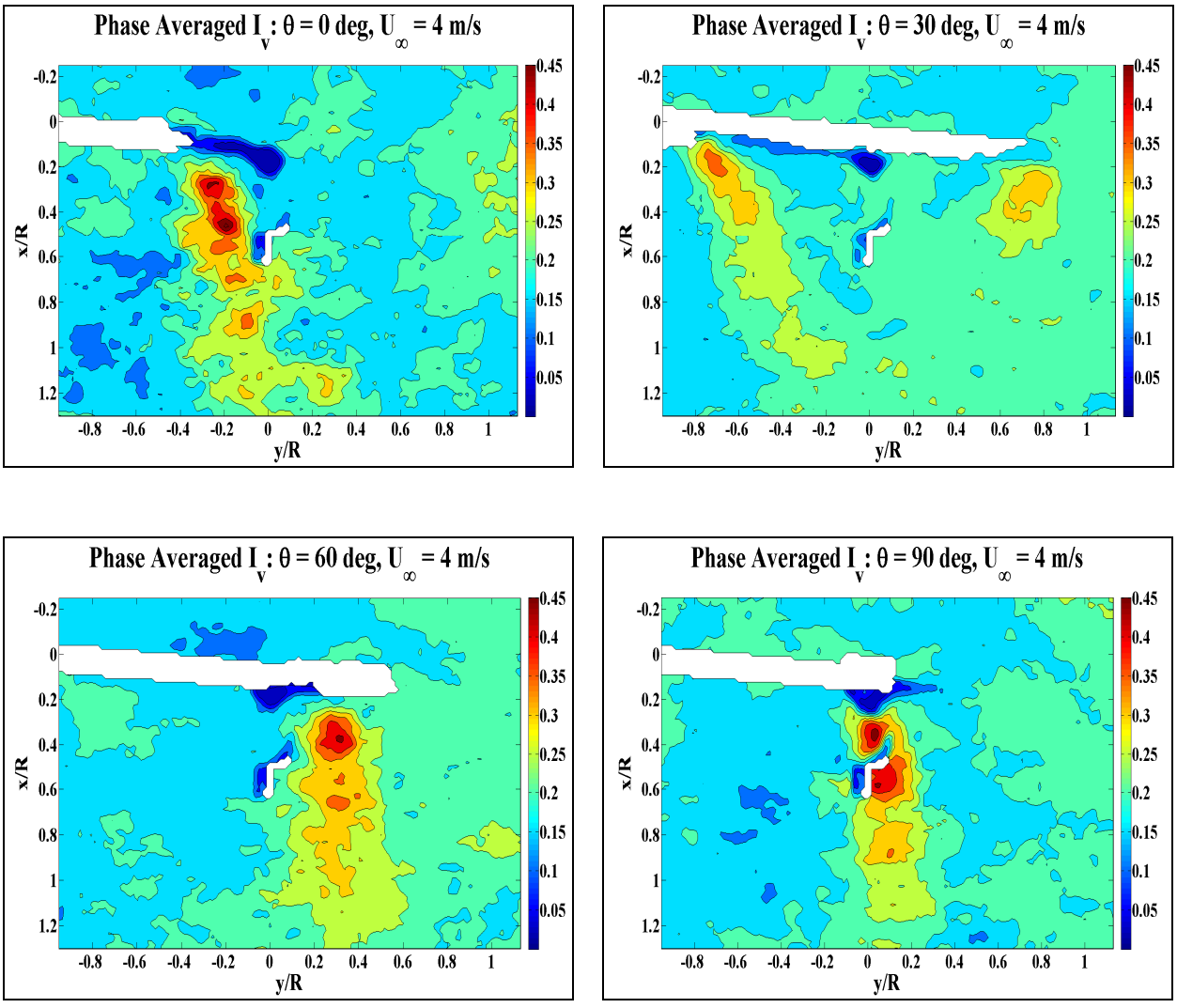

Figure 4.5: Phase averaged contour plots of crosswind turbulence intensity.

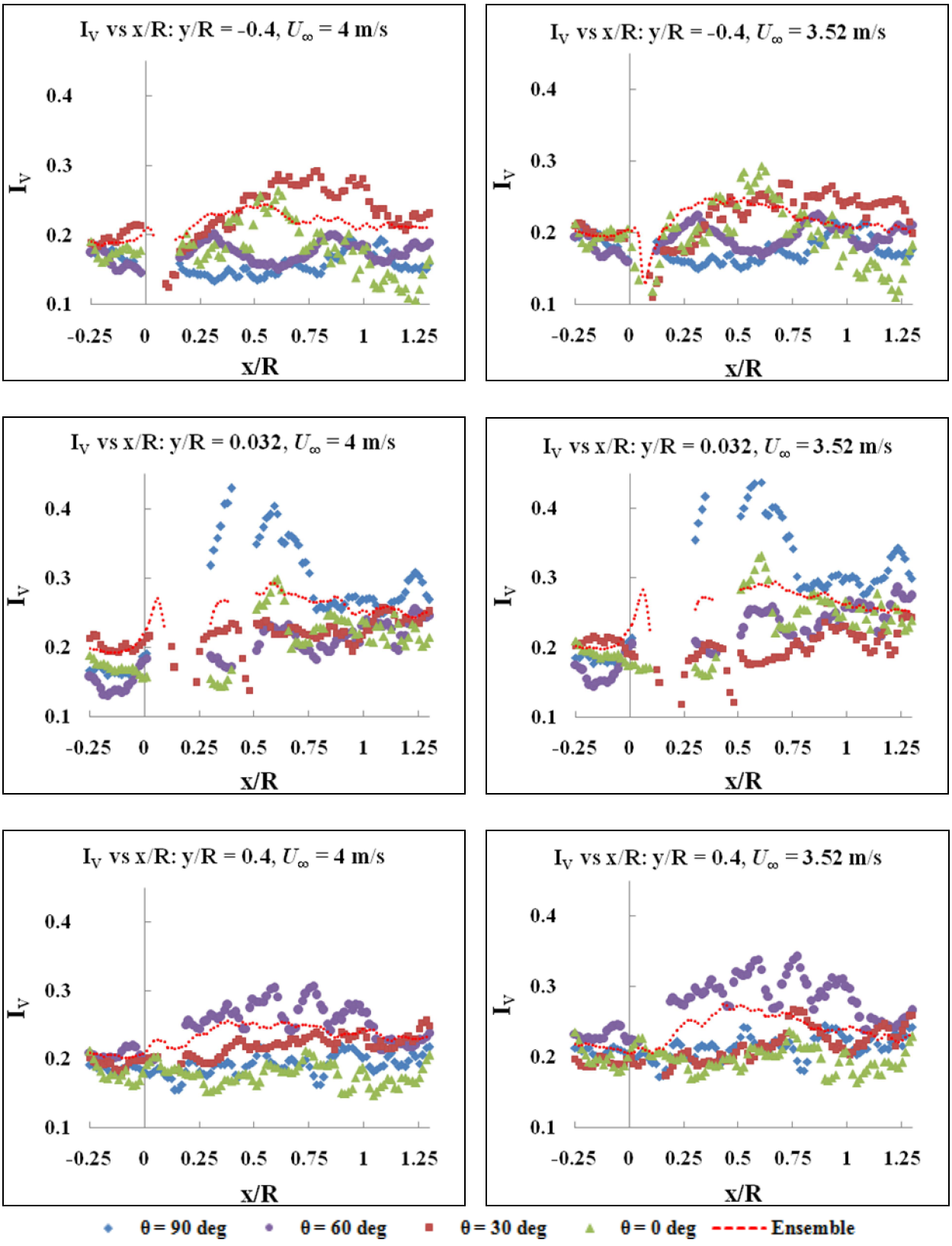

Figure 4.6: Comparison of crosswind turbulence intensity as a function of wake distance for three spanwise locations (y/R) of -0.4, 0.032 and 0.4.

4.1.5 Reynolds Stress

The Reynolds stress, in the horizontal plane, is computed by multiplying the streamwise and crosswind turbulent velocities at each grid point within the vector field, and averaging the velocity product across the data set. In the transport equations of turbulent kinetic energy, the production term, $\langle u_i u_j \rangle \langle S_{ij} \rangle$, emerges in both the mean and turbulent flows with opposing signs. A negative sign attached to the Reynolds stress (i.e. $-\langle uv \rangle$) indicates that the production of TKE is viewed from the perspective of the turbulence. In other words, the turbulence extracts energy from the mean flow. This sign convention is adopted for all cases in the present study.

The ensemble averaged Reynolds stress normalized by U_∞^2 is presented in Figure 4.7. The contour plot, Figure 4.7 (a), shows segregated behaviour of the Reynolds stress; that is, the left hand side is mostly positive, while the right hand side is mainly negative. The spanwise variation of Reynolds stress, shown in Figure 4.7 (b), exhibits symmetry about the centerline. However, it should be noted that different signs of Reynolds stress in Figure 4.7 are due to the change in the direction of the velocity components (primarily crosswind velocity component) about the rotor centerline. Therefore, the positive or negative signs of Reynolds stress do not represent the direction of energy exchange between the mean and turbulent velocity fields. In the subsequent Reynolds stress plots, the contours are still presented with both signs to illustrate the influence of velocity direction. On the other hand, the phase averaged Reynolds stress profiles are presented in absolute terms to quantify its magnitude and hence turbulence production under different rotor configurations.

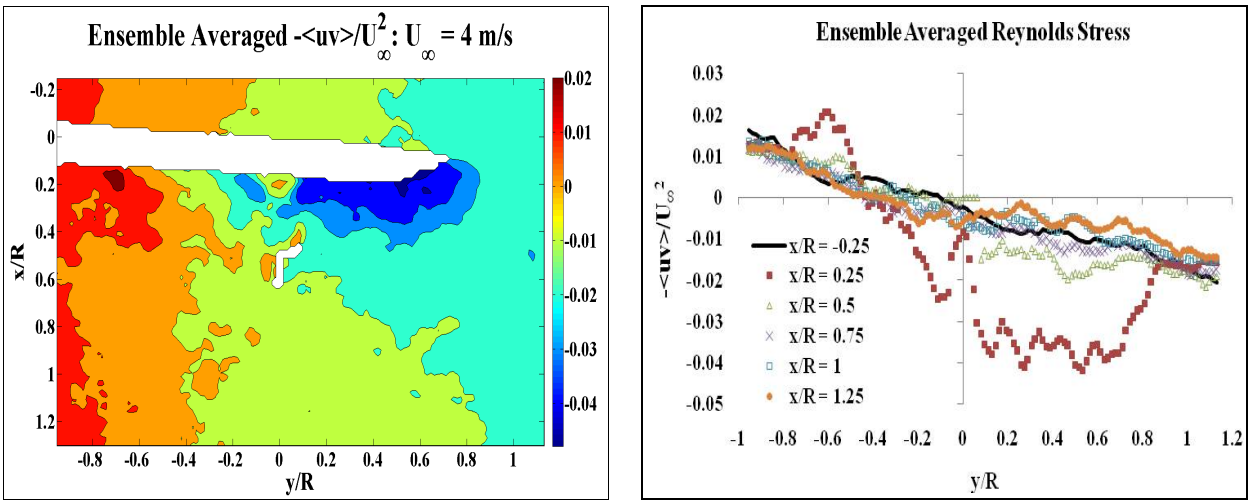

(a) **(b)**

Figure 4.7: Ensemble averaged Reynolds stress at wind speed of 4 m/s **(a)** Contour plot **(b)** Spanwise distribution at upstream and downstream positions.

Previous research makes it clear that shear is generated by the formation of tip vortices at the wake boundary. However, the high shear stress levels occur short of $y/R = \pm 1$ due to the physical limitation of where individual blades intersect the laser sheet. Figure 4.7 (b) shows that the Reynolds stress upstream of the rotor varies linearly, approaching zero at the centerline. Upon contact with the turbine, the Reynolds stress is observed to be 2 – 4 times greater at $x/R = 0.25$ than in the incident flow, which is similar to the results presented in [40]. Progressing deeper into the wake, the augmented stress levels recede back to the upstream conditions.

To widen our understanding of the Reynolds stress, analysis of individual blade positions is carried out because they avoid the recurring issue intrinsic to ensemble averaging, i.e. smoothing effect. Figure 4.8 illustrates a combination of contour and spanwise distribution plots of normalized phase averaged Reynolds stress. The four angular positions share two common traits that distinguish them from ensemble averaging. Firstly, as with mean streamwise $U_{Deficit}$ and turbulence intensities, the shear stress is localized in a narrow region behind the blade. Secondly, the increase of shear developed by rotor generated vortices exceeds those observed in the

ensemble averaged plot by a wide margin. As the mean velocity gradients are not expected to vary significantly in the measurement domain, any variation in the turbulent kinetic energy production would be primarily dependent on the variation in the Reynolds stress. The plots in Figure 4.8 show local enhancement of the Reynolds stress immediately behind the blade, which stays higher than the background level almost up to x/R = 1. An enhancement up to almost a factor of 8 is observed at some phases. These results imply that a significant local augmentation of turbulence production occurs in the near wake region, while ensemble averaging numerically suppresses it. The plots also show that the Reynolds stress at each phase is not identical: the normalized peaks fluctuate between 0.06 (at 30 degrees) and 0.1. Furthermore, the Reynolds stress arising from negative shear (blue contours) is generally larger than the positive shear. Despite the vortex system breaking down at each phase, the Reynolds stress does not completely return to the background levels.

Figure 4.9 shows the spanwise distribution of phase averaged normalized Reynolds stress magnitude at the wind speed of 3.52 m/s. The profiles display similar behaviour as in Figure 4.8, but the normalized Reynolds stress magnitude is slightly greater with a more uniform level of stress between positive and negative values.

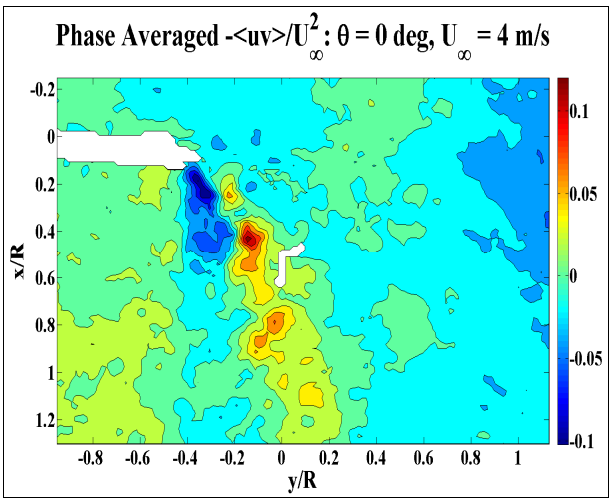

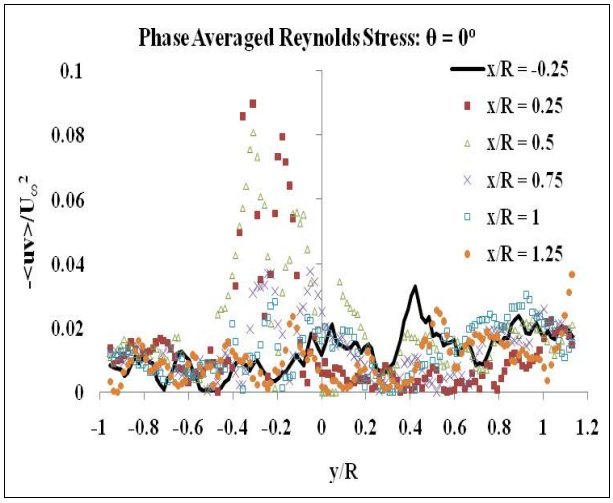

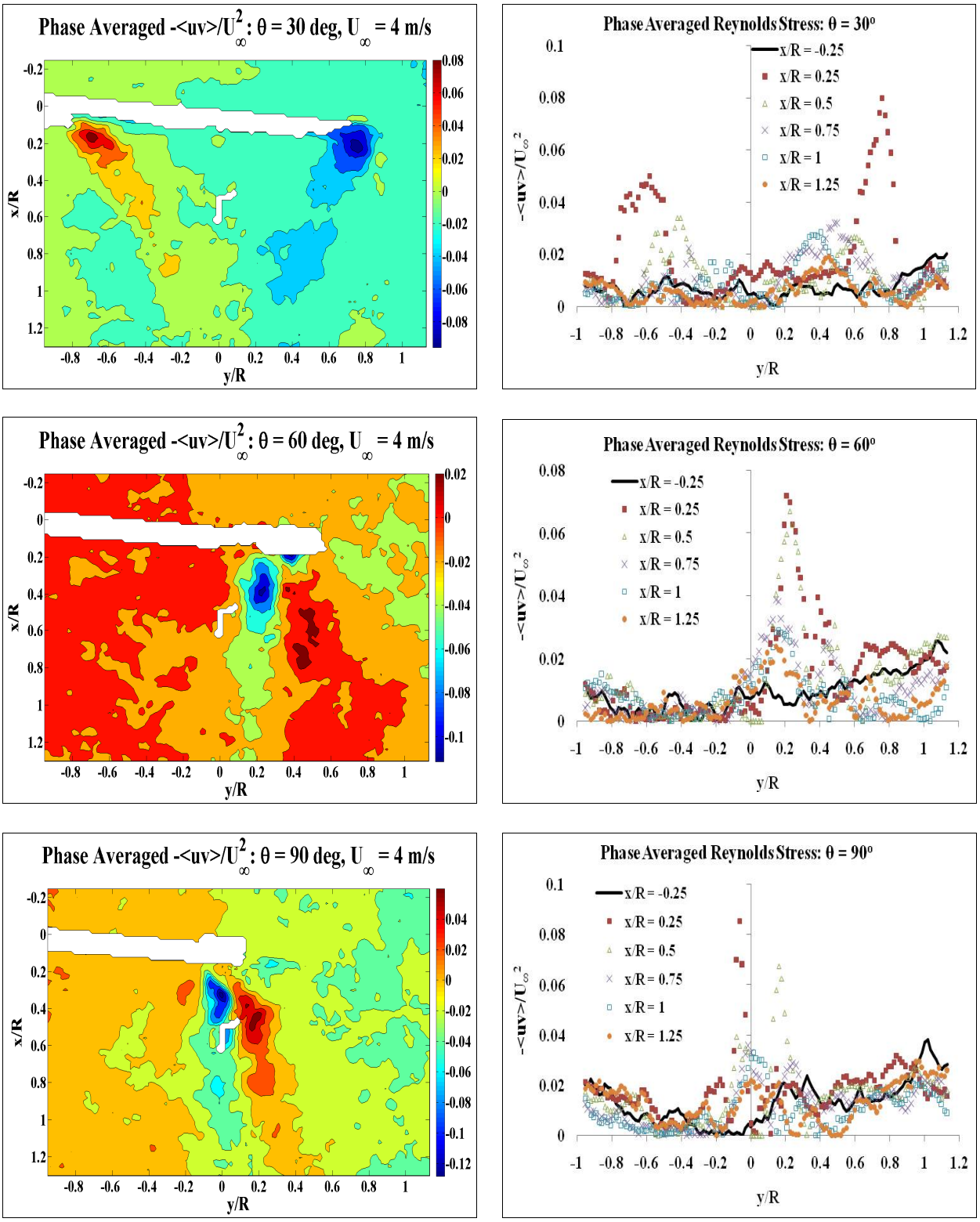

Figure 4.8: Phase averaged Reynolds stress **(left)** Contour plot **(right)** Spanwise distribution of absolute values.

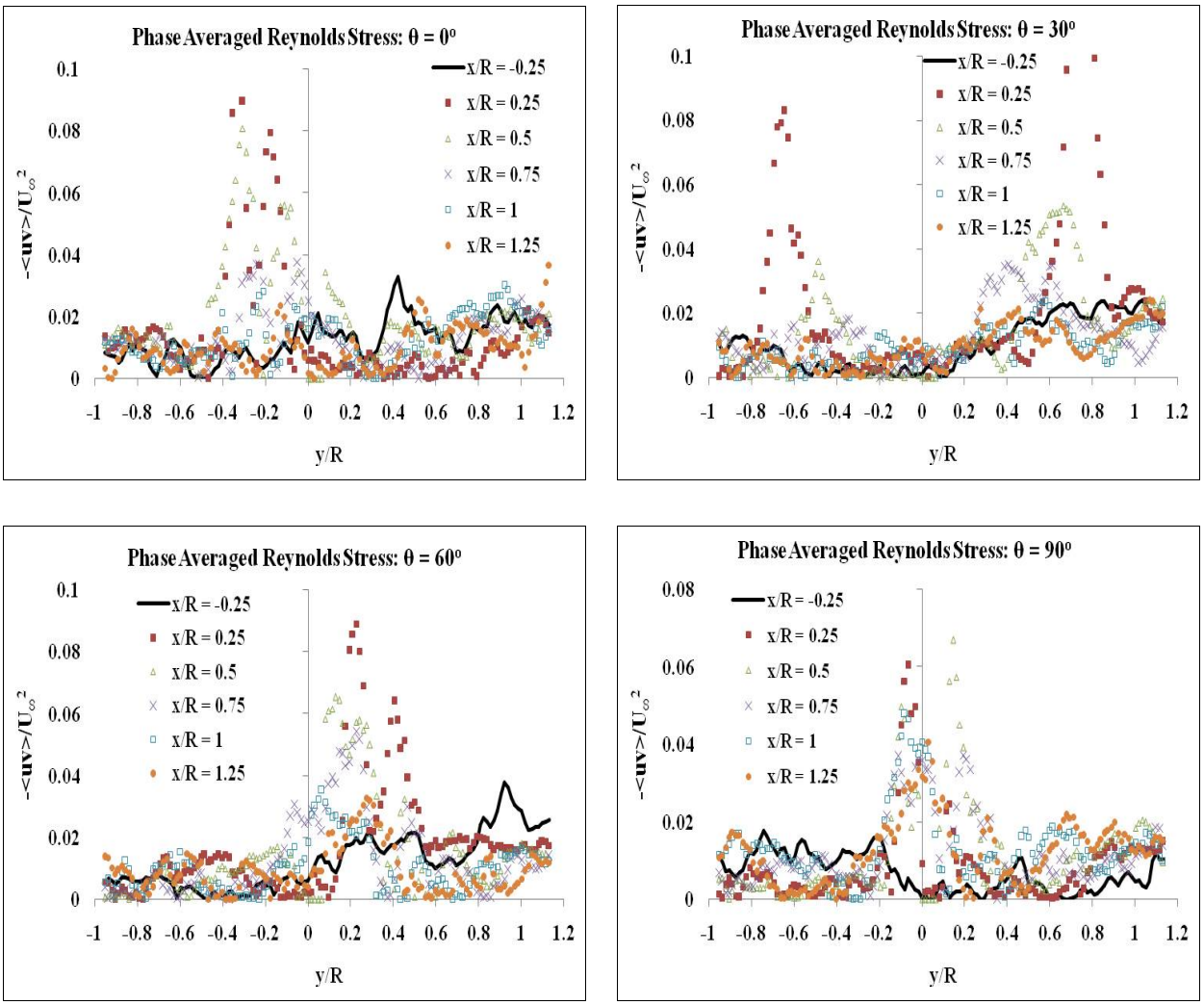

Figure 4.9: Absolute values of phase averaged Reynolds stress, normalized by U_∞^2, at wind speed of 3.52 m/s.

4.1.6 Spectral Analysis

The wavenumber spectra of the horizontal and vertical turbulent velocities are computed for all cases. For each case, the one-dimensional wavenumber spectrum was computed in the crosswind direction at all downstream locations in each velocity field and then averaged at each downstream location. Each spectrum is plotted with log-log axes, and resolved wavenumbers from about 40 rad/m to 2600 rad/m with the resolution of 40.5 rad/m. The corresponding wavelength range is from 155 mm to 2.4 mm (see Appendix B for more details). Due to the

limitation of the grid spacing set by the interrogation window size, there is an abrupt cut-off at the highest wavenumber (i.e. scales smaller than 2.4 mm were not resolved).

Equally important for the reader is to grasp the basic physical process that generates turbulent kinetic energy in the wake, and the mathematical terms involved (i.e. transport equations). Sanderse [64] explains that because the rotor is an instability to the incident flow, kinetic energy from the latter is transferred to the large scale motions that form during wake expansion. These eddies persist so long as they are supplied with energy by shear (i.e. from the shear layer). Furthermore, when the wake boundaries grow, the vorticity increases as the vortices are stretched, triggering an energy cascade from larger to smaller scales (or from lower to higher wavenumbers) [35].

Figure 4.10 presents ensemble averaged wavenumber spectrum of the streamwise velocity fluctuations (F_{11}), normalized by the product of U_∞^2 and rotor diameter. Three slopes that demonstrate power law decay rates at different wavenumber bands are also shown as reference. The spectra, in general, show the classical trend of energy cascading. The lowest spectral energy level is observed in the region upstream of the rotor and the highest spectral energy level is observed immediately downstream of the rotor. This demonstrates that the turbine blades enhance turbulence, as expected. The spectra immediately downstream of the rotor show a bulge. This bulge indicates the energy input at these scales. The bulge covers the range from about 80 rad/m to 400 rad/m with the peak at the wavenumber of about 120 rad/m. The corresponding length scales are 79 mm to 16 mm with peak at 52 mm. In terms of blade length, these length scales are approximately R to 0.2 R, with peak at 0.7 R. Since these spectra are computed from the entire dataset at a particular wind speed (i.e. ensemble averaging), it can be concluded that the overall energy input into the turbulent flow occurred over this band of scales. The plots in

Figure 4.10 also show that this bulge of energy input exists up to a downstream distance of about 0.4 R, which indicates that the influx of energy into the turbulent flow ceases after a 1/4 of the rotor diameter downstream. Additionally, results determined that the spectral energy continues to decrease with an increase in downstream distance from the rotor; even at the distance of x/R = 1.3, the spectral energy remains higher than that upstream of the rotor. The inertial subrange, where the slope exhibits $-5/3$ decay rate, is evident in both downstream (x/R > 0.5) and upstream spectrum. The inertial subrange covered wavenumbers ranging between 120 rad/m to 400 rad/m (corresponding length scales are 52 mm to 16 mm, respectively). At higher wavenumbers, viscous damping causes a steeper decline of energy at the small scales.

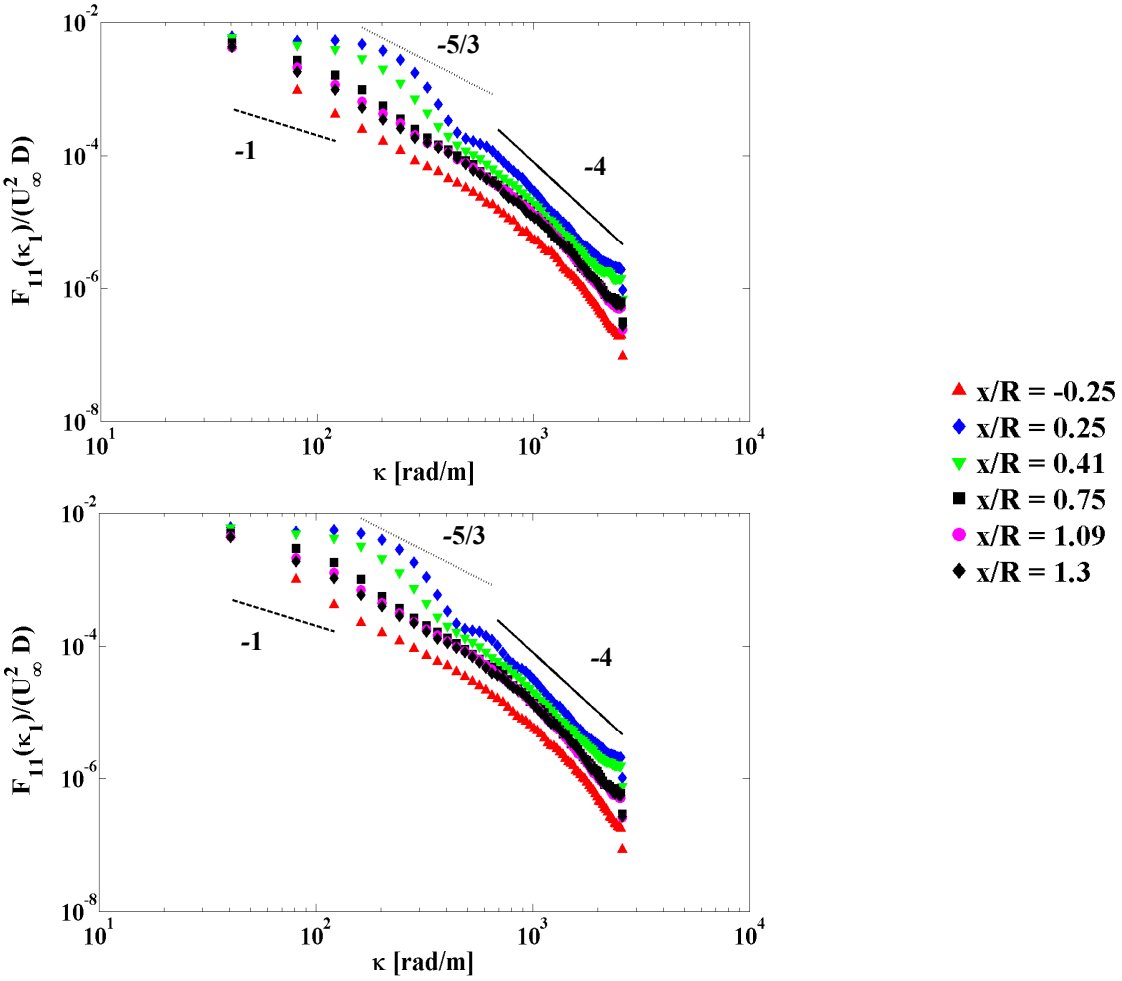

Figure 4.10: Ensemble averaged streamwise wavenumber spectrum **(top)** U_∞ = 4 m/s **(bottom)** U_∞ = 3.52.

To further confirm the length scales associated with the inertial subrange observed in the above spectra, another independent relationship is used, and is given below,

$$\frac{L}{\eta} \approx R_l^{3/4}, \tag{4.4}$$

where L is the integral length scale, η is the Kolmogorov microscale, and R_l is the Reynolds number associated with the length scale, l, of the inertial subrange [35]. Integral length scale is assumed to be equal to the rotor diameter, which is reasonable (i.e. L = 0.15 m), while η is computed from $(\nu^3/\varepsilon)^{1/4}$ to give a value of 0.138 mm. From Eq. 4.4, R_l is estimated to be 520 and the characteristic scale of the inertial subrange was found to be $l \approx 40$ mm, which is comparable to that obtained from the wavenumber spectra.

The normalized wavenumber spectra of crosswind turbulent velocity component (F_{22}) at wind speeds of 4 and 3.52 m/s are plotted in Figure 4.11. In general, both spectra have the shape similar to that of F_{11}, except that no bulge of energy input is present. This indicates that the energy input to the turbulent velocity field is primarily through the streamwise velocity component, which later redistributes among other velocity components. The spectra also show that energy remains almost the same at all downstream locations, but is higher than the spectral energy upstream of the rotor. The anisotropy is estimated by computing the ratio of streamwise to crosswind spectra at the lowest wavenumber for different axial locations. The results are tabulated in Table 4.2. The significance of the values is that in isotropic turbulence, the ratio must be equal to two [35]. Results in Table 4.2 show that some anisotropy exists within the large scales.

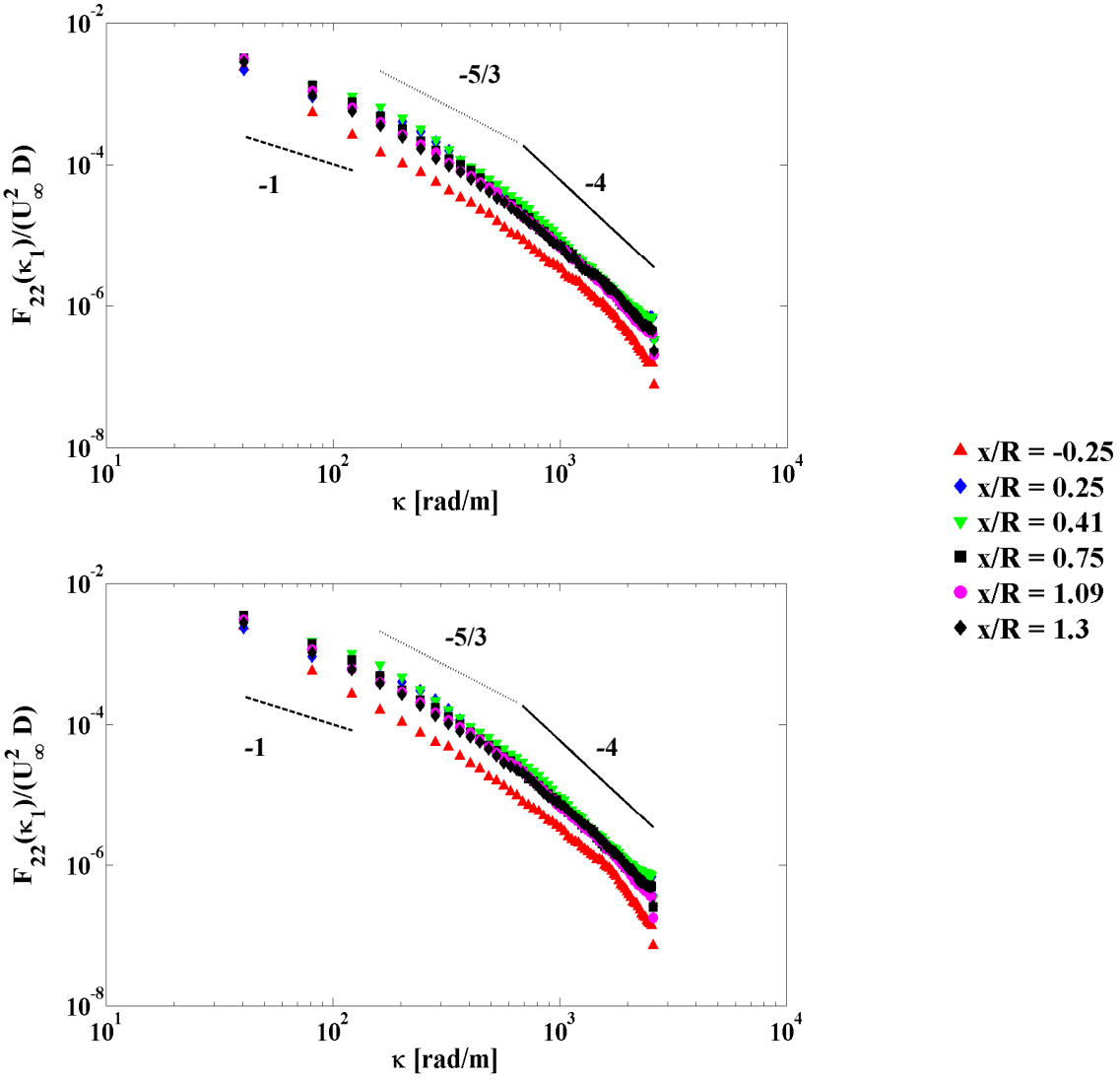

Figure 4.11: Ensemble averaged crosswind wavenumber spectrum **(top)** U_∞ = 4 m/s (**bottom)** U_∞ = 3.52.

Table 4.2: Ratio of spectral energy at lowest wavenumber

x/R	**-0.25**	**0.25**	**0.41**	**0.75**	**1.09**	**1.3**
$F_{11}(40.5)/F_{22}(40.5)$	1.85	2.77	2.08	1.53	1.37	1.48

The normalized phase averaged streamwise wavenumber spectra at downstream positions of 0.25 *R*, 0.75 *R*, and 1.3 *R* are presented in Figure 4.12 at two wind speeds. All phases contain a bulge in the spectra immediately downstream of the rotor, which corresponds to the length scales whereupon energy is transferred to the turbulent flow by the rotor. That is, the energy is related

to the length scales of blade-shedding vortices. The spectrum at 30 degrees displays a slightly different bulge profile, and the reason could be due to the absence of an active blade within the measurement plane. Thus, the energy associated with shedding vortices may not have been fully captured in the spectrum. This is further substantiated by the fact that its spectral energy is lower than the other phases (which captured the energy of the shedding vortices). At this downstream position, anisotropy related to the larger vortices prevents the formation of an inertial subrange. As soon as the flow develops further into the wake, energy decays and the curves collapse onto one another. Also, the inertial subrange extends slightly with wake distance. Wind speed does have a minor effect, more so at distances close to the rotor, but the overall behaviour remain unaltered.

Figure 4.13 displays normalized phase averaged crosswind wavenumber spectra at axial positions of 0.25 R, 0.75 R and 1.3 R. There are some disparities between phases, but less severe compared to the streamwise plots. Similar to Figure 4.11, large eddies and scales within the inertial subrange become more turbulent as the flow progresses deeper into the wake (i.e. spectral energy at $x/R = 0.75$ is greater than at $x/R = 0.25$). Moreover, the inertial subrange forms at all downwind locations, slightly expanding to smaller scales as the wake evolves.

Ensemble averaged plots in Figure 4.10 and Figure 4.11 respectively contain higher levels of spectral energy at low to middle wavenumbers than the phase averaged curves. This result is unsurprising because ensemble averaging includes vortices from all phases at each downwind position. Moreover, once the inertial subrange is established, the range of wavenumbers it covers is roughly the same in both averaging schemes.

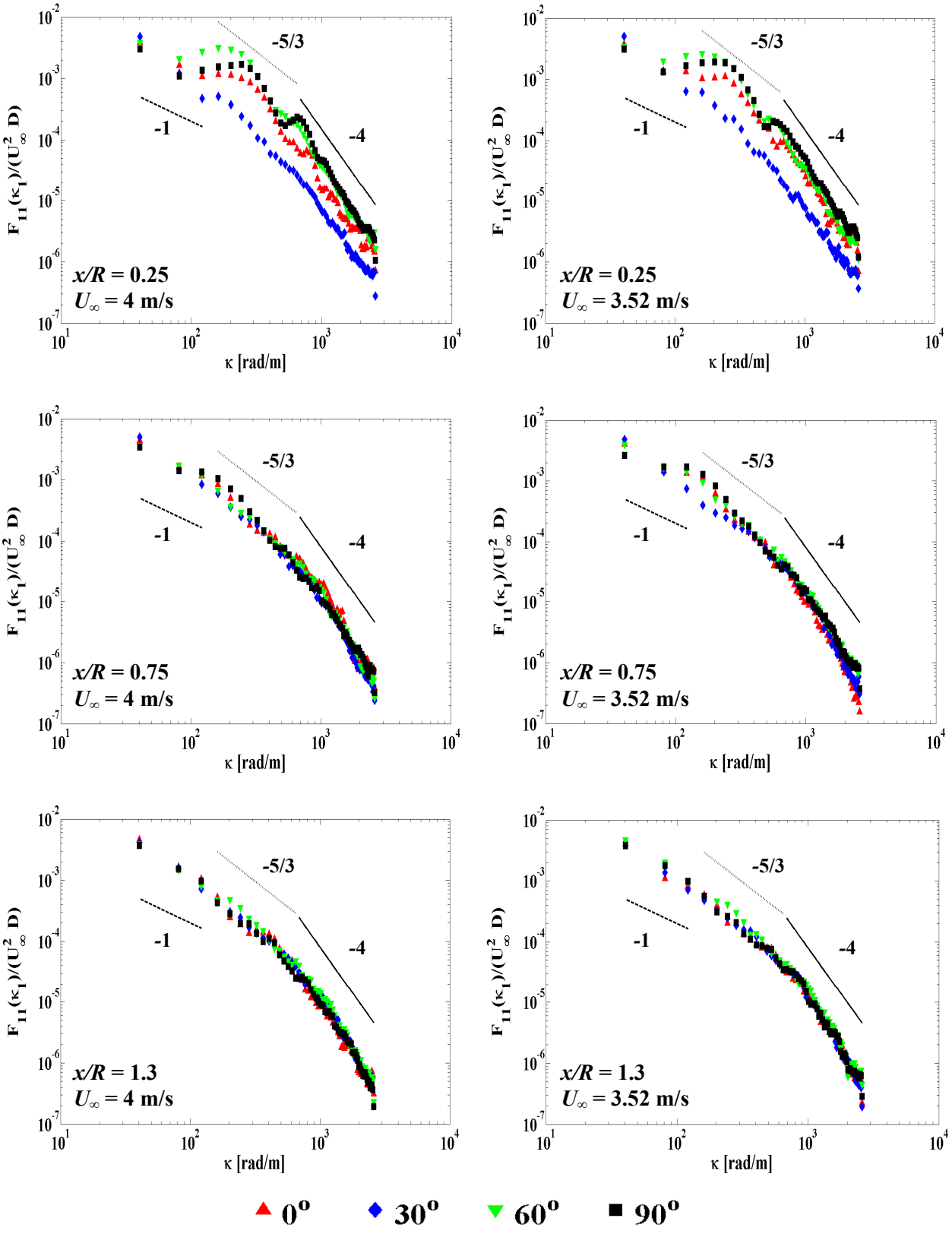

Figure 4.12: Phase averaged streamwise wavenumber spectra at axial locations of 0.25, 0.75, and 1.3 *R*.

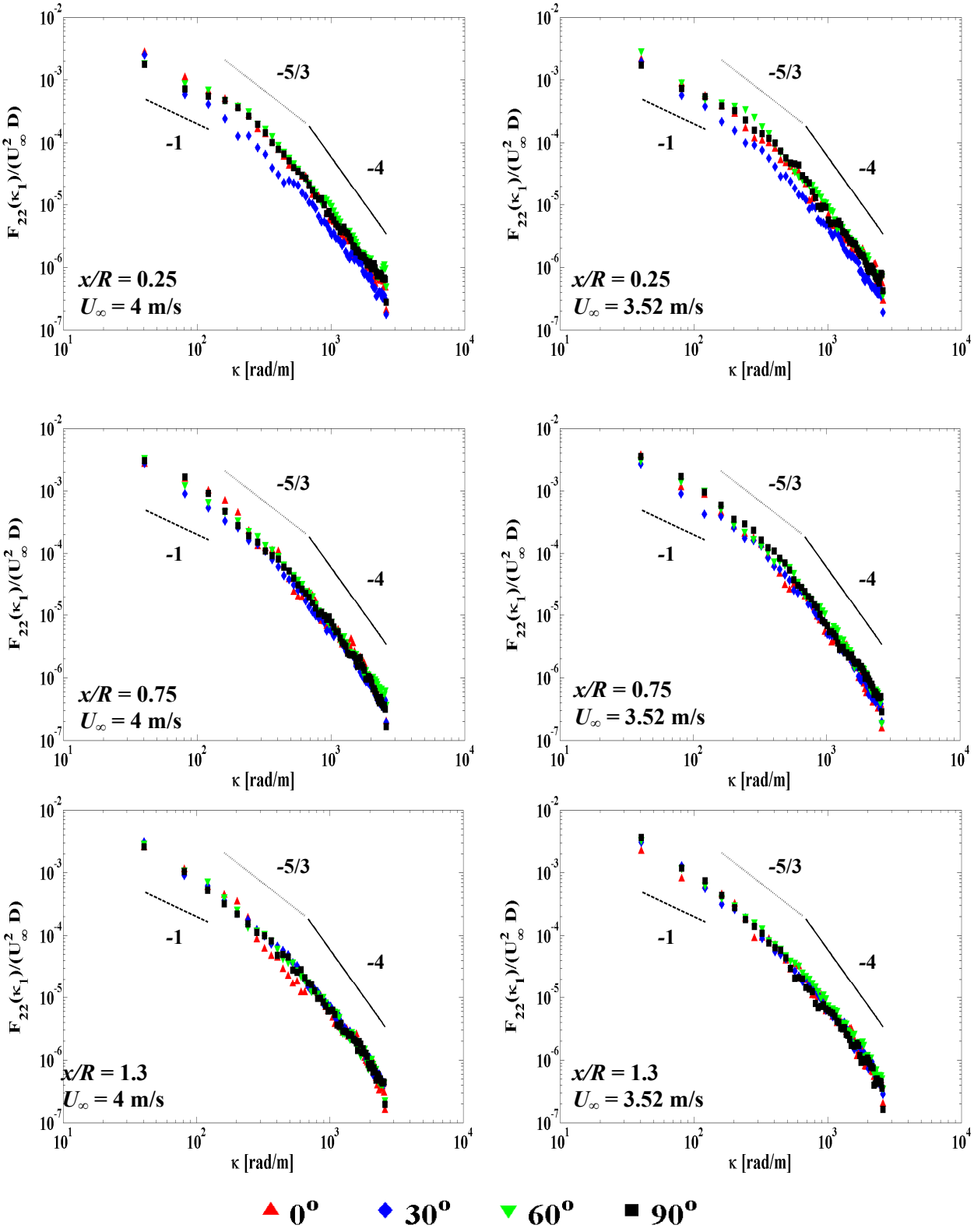

Figure 4.13: Phase averaged crosswind wavenumber spectra at axial locations of 0.25, 0.75, and 1.3 *R*.

4.2 Measurements at z = 0.135 m

4.2.1 Ensemble Averaged Turbulence Intensity

As mentioned earlier, the velocity field measured at this height captured the interaction of blades and support tower and the influence of this interaction on the near wake flow structure. The contours of the ensemble averaged streamwise and crosswind turbulent intensities at the wind speed of 4 m/s are presented in Figure 4.14. The plots show the effect of the support tower on ensemble averaged turbulence intensities in both the streamwise and crosswind directions. Centerline values of streamwise turbulence intensity barely increase beyond upstream percentages. The reason is that the cylinder acts to destroy generated vortices coming into direct contact. Away from the cylinder's vicinity, the induced flow from the rotor has strength comparable to that displayed in Figure 4.1. In regards to crosswind turbulence, the cylinder wake is more prevalent than the helical vortex sheet. Its strength and width (roughly 3 times the cylinder diameter) is uncompromised as the flow is advected downstream. Rotor effects, though less intense, still produces a noticeable, but unvarying degree of turbulence.

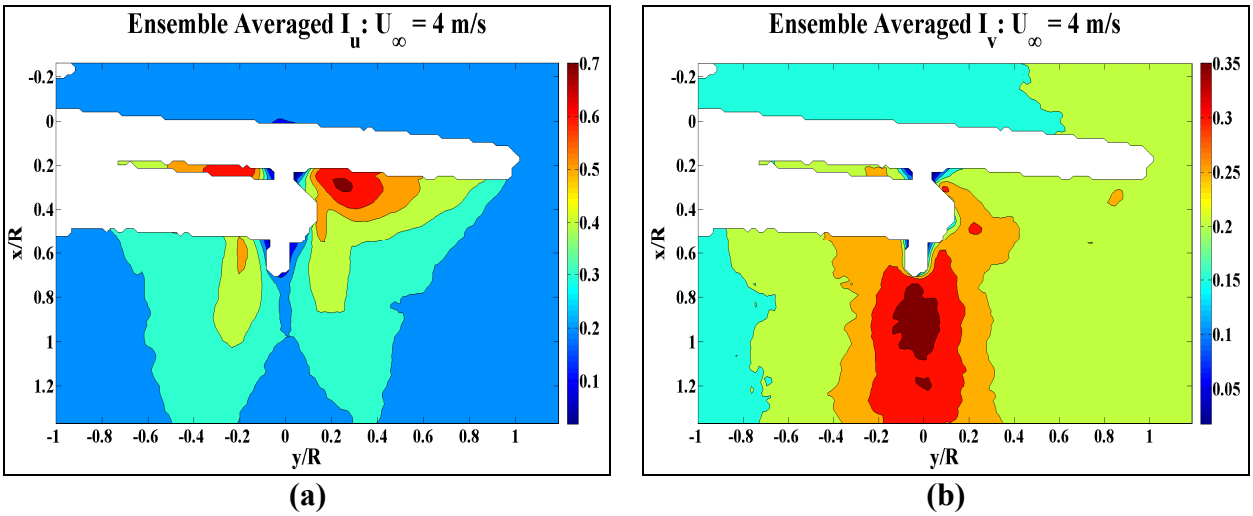

Figure 4.14: Ensemble averaged contour plots of turbulence intensity **(a)** Streamwise **(b)** Crosswind.

4.2.2 Phase Averaged Streamwise Turbulence Intensity

Phase averaged streamwise turbulence intensity contour plots are shown in Figure 4.15. Despite the shadow effect, the selected phases are exemplary in their portrayal of the flow: phases of 0 and 60 degrees are mirror images at this height. The separated flow from individual blades is the primary source of the strong turbulence. Flow separation from the rearward face of the cylinder can be observed at phases of 0 and 90 degrees, with intensity of approximately 40 to 45 percent. The assumption is that this secondary source of turbulence production coalesces with the rotor wake, where the combined flow ultimately dissipates.

Plots of phase averaged streamwise turbulence intensity at spanwise locations of 0 , 0.2 R and 0.6 R, at wind speeds of 4 and 3.22 m/s, are shown in Figure 4.16. The ensemble averaged profiles are also included for reference. The three respective locations depict turbulence in the cylinder wake, separated flow from its surface, and by the individual blades. At y/R = 0, the cylinder marginally enhances I_u at all phases. From Eq. 4.2, the maximum centerline added turbulence intensity is roughly 15 percent, with I_∞ estimated to be 26 percent.

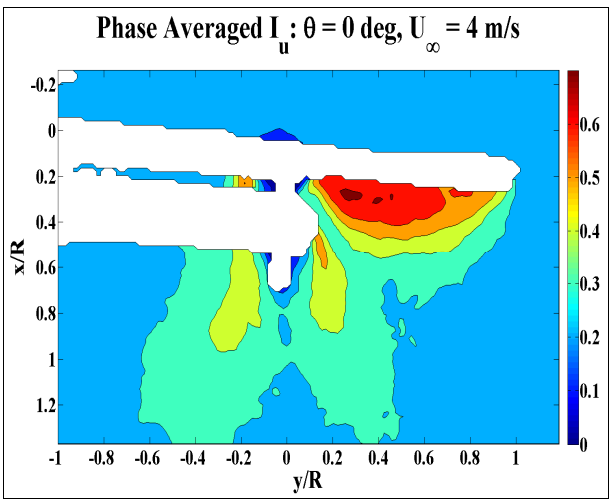

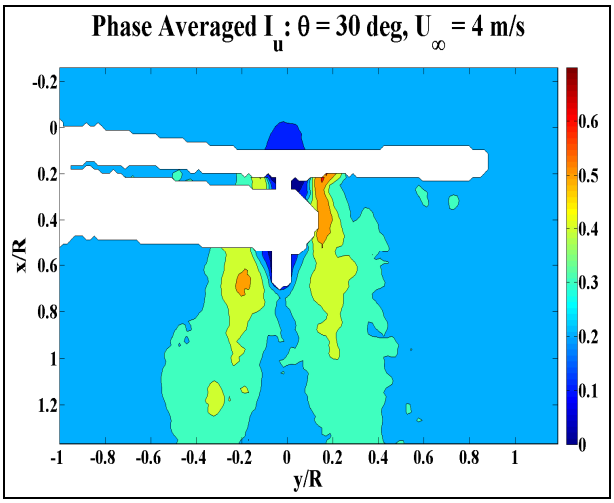

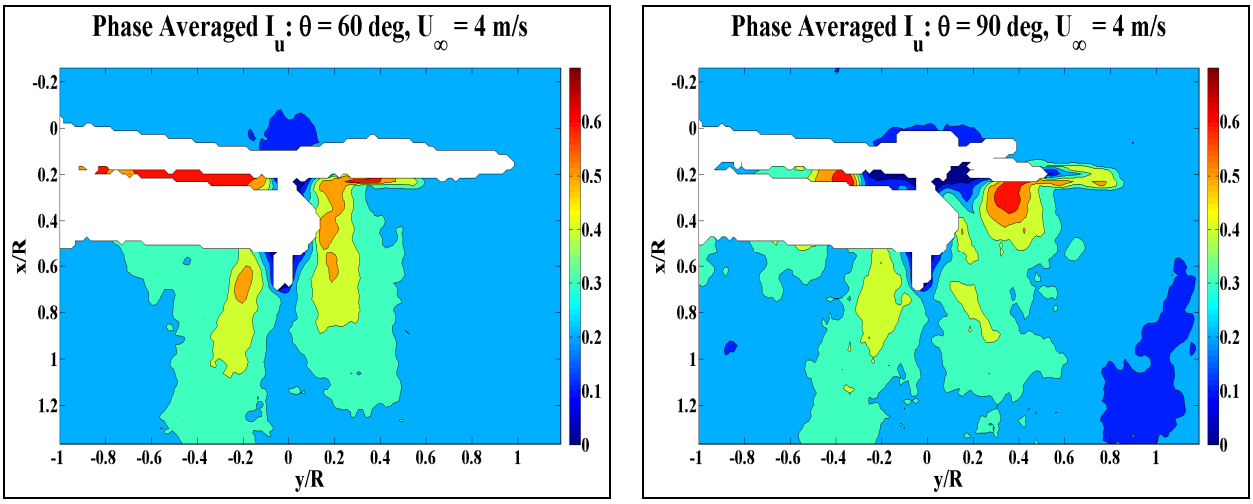

Figure 4.15: Phase averaged contour plots of streamwise turbulence intensity.

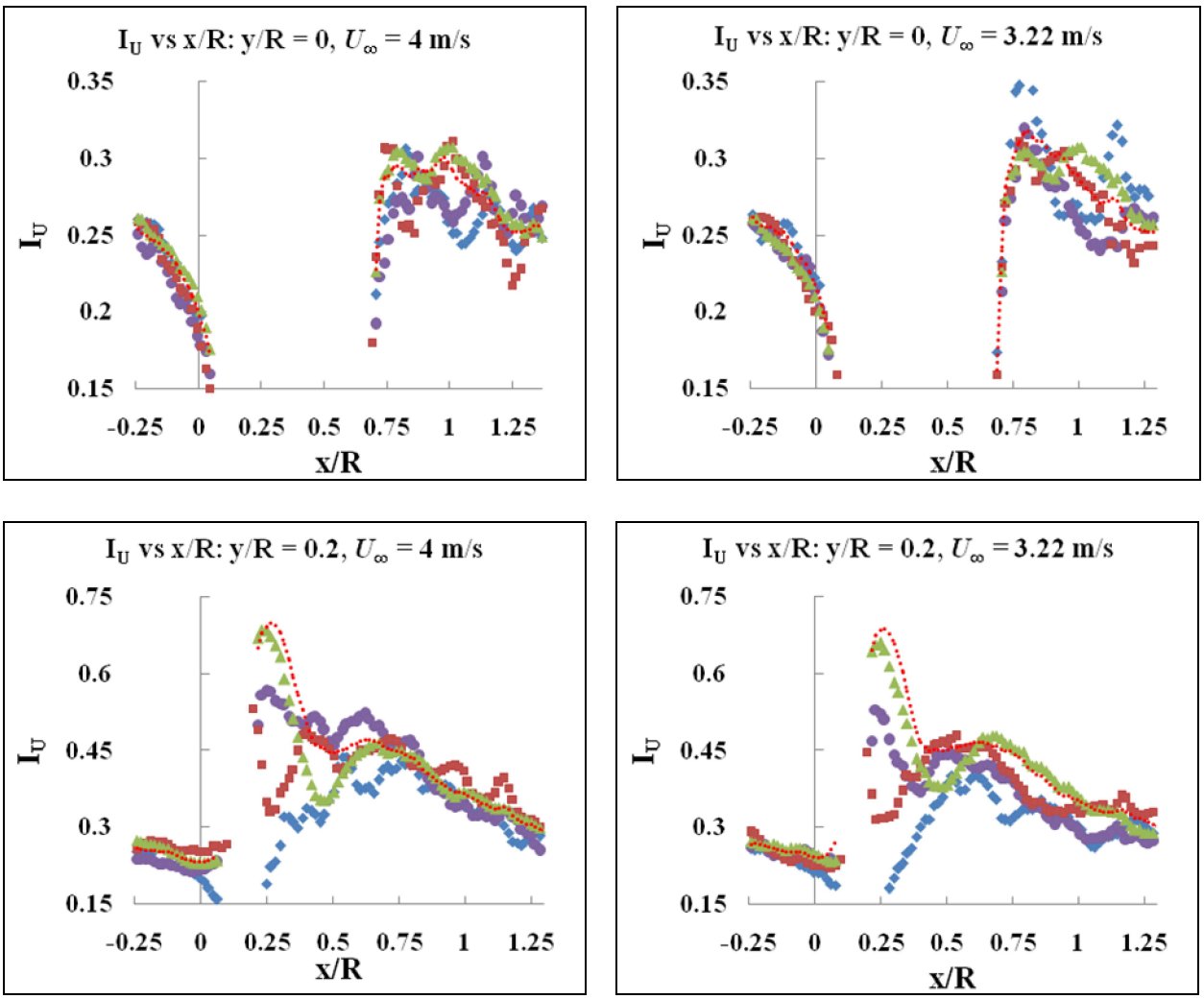

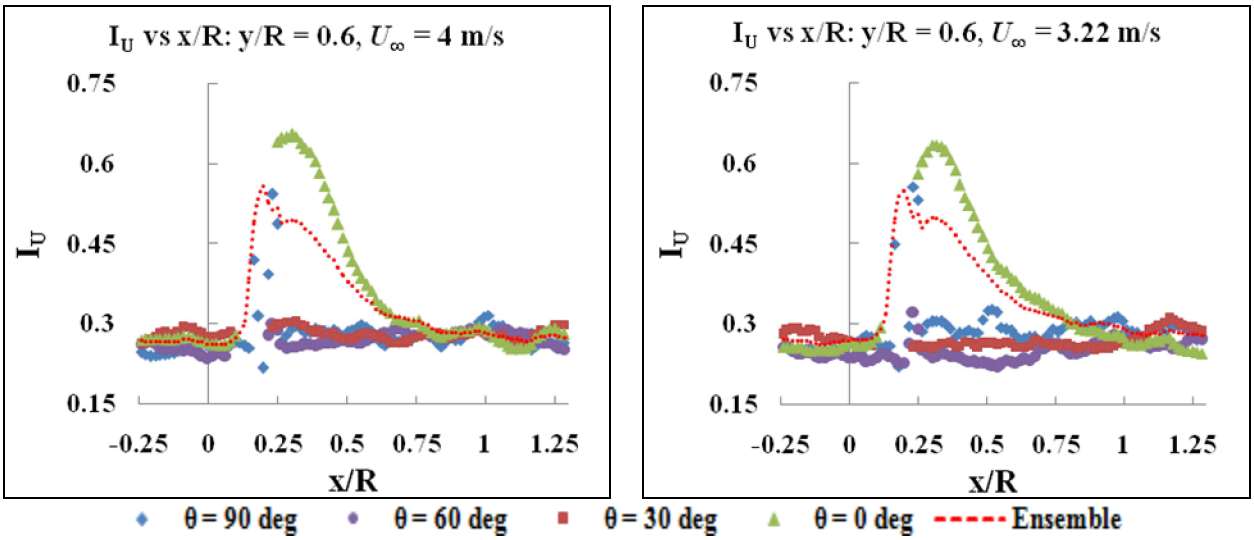

Figure 4.16: Phase averaged plots of streamwise turbulence intensity at spanwise locations of 0, 0.2 *R*, and 0.6 *R*

This maximum is notably lower than that in Figure 4.4 because the cylinder actively negates the shed vortices. For small downwind distances, some phases have greater and lower intensities than the ensemble averaged curve, emphasizing the unsteadiness of the wake and the spatial smoothing effect. At y/R = 0.2, the blade generated vorticity at 0, 30, and 60 degrees are allowed to develop with varying magnitudes up to x/R = 0.25. At this point in the wake, the blade induced flow mixes with the weaker vortex system of the cylinder. The turbulence intensity then jointly decays; it differs from the results in Figure 4.3 as the values remain above freestream for all curves. At y/R = 0.6, a reference blade at 0 degrees shows a higher level of turbulence than the ensemble averaged curve, while all other phases appear relatively constant with wake position. Minor discrepancies do appear between the wind speeds, but the overall behaviour of the phase averaged patterns are identical.

4.2.3 Phase Averaged Crosswind Turbulence Intensity

Figure 4.17 illustrates the influence of the tower on the crosswind turbulence intensity. All phases show that the enhancement effect, in relation to I_u, is much more significant relative to

freestream. The phenomenon giving rise to this increase in I_v must be caused by the standing vortices accompanying flow recirculation [61]. In addition, the turbulence does not appear to dissipate even at the downstream distance of 1.3 R. At a phase of 0 degrees, the tip vortices can be observed moving towards the larger fluid structure.

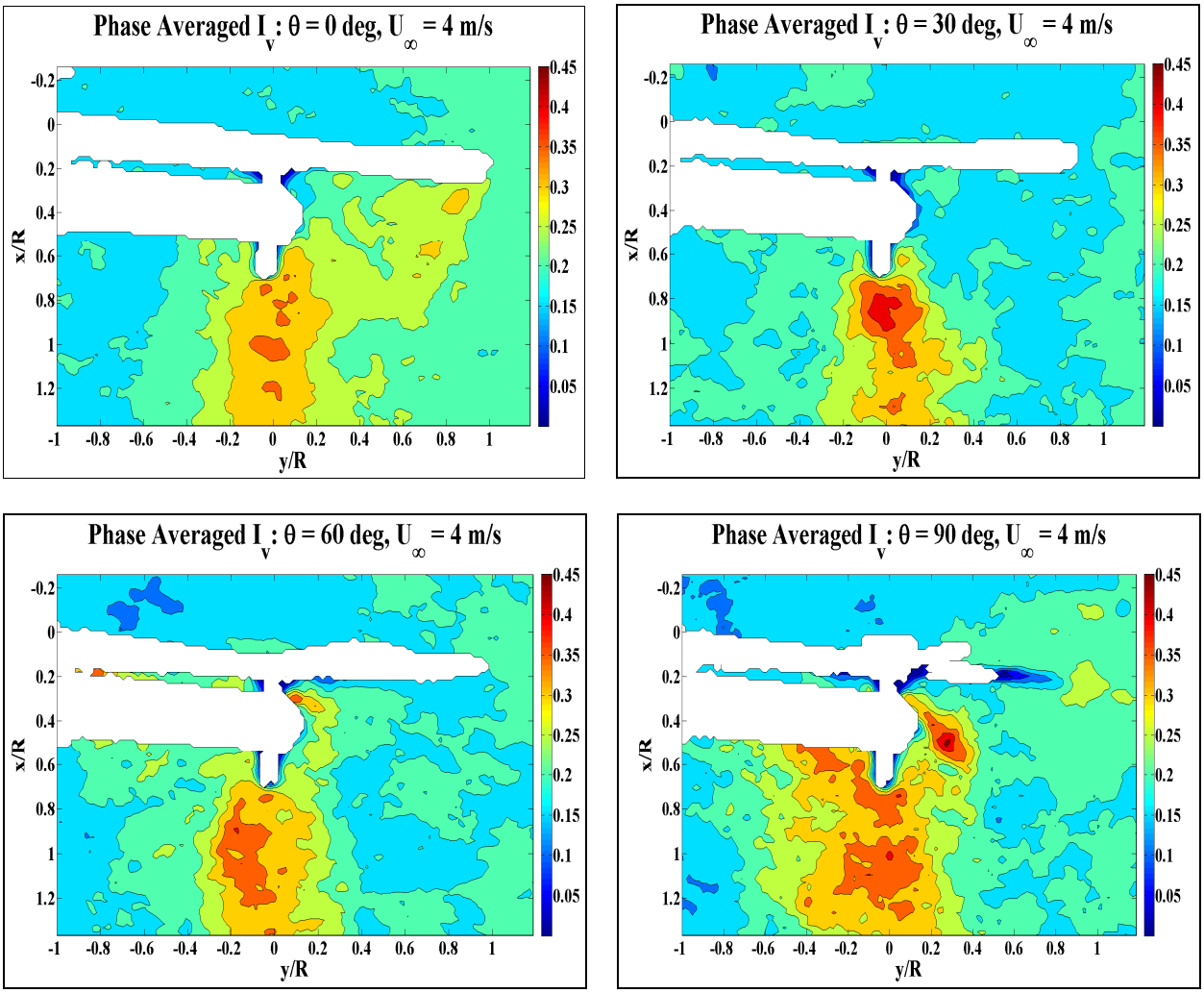

Figure 4.17: Phase averaged contour plots of crosswind turbulence intensity.

Crosswind turbulence intensity is examined more closely at centerline and at y/R = 0.8 in Figure 4.18 to acquire details of tower and blade effects, respectively. Each phase can be seen to have different contributions in added turbulence intensity from the tower. Although the tower is

rigid, the periodic nature of the rotor is the cause for the variation in strength about the ensemble averaged curve. Turbulence intensities around 35 to 40 percent are comparable to results in Figure 4.6, with the exception of a lack in decay. At the lower wind speed of 3.22 m/s, all phases show a decline in added turbulence intensity, with no prominent change to ensemble averages. Tip vortices induce a maximum crosswind turbulence intensity of 32 percent at x/R = 0.35, but decreases very quickly under the influence of freestream turbulence.

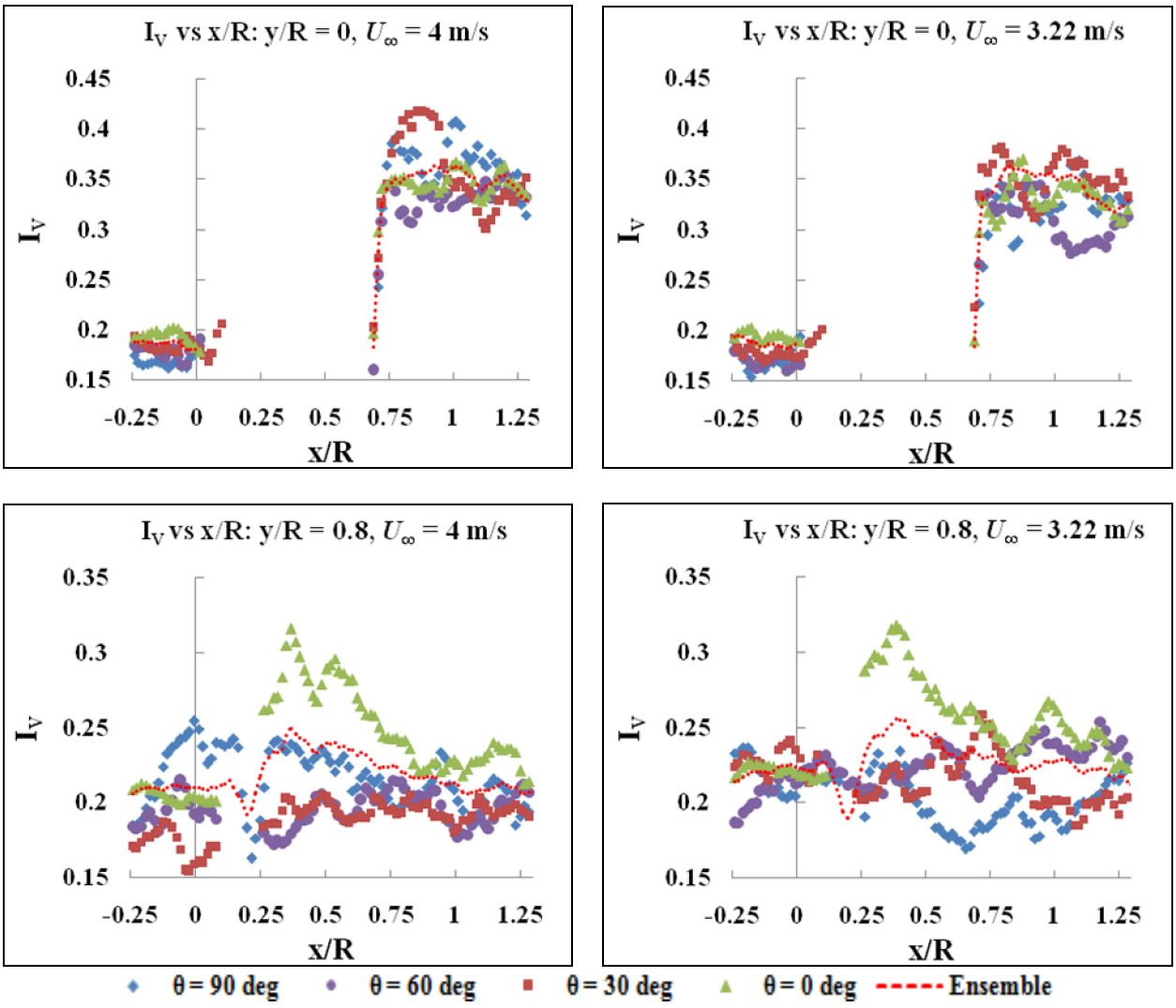

Figure 4.18: Phase averaged plots of crosswind turbulence intensity at spanwise locations of y/R = 0 and 0.8.

4.2.4 Reynolds Stress

Figure 4.19 shows ensemble averaged Reynolds stress normalized by the square of the freestream velocity. The Reynolds stress generated from the turbine and tower is of opposite signs, with higher amounts attributed to the rotor, while the magnitude at centerline is effectively zero. The peak Reynolds stress immediately behind the rotor is approximately a factor of 1.5 times higher than the peak Reynolds stress immediately behind the tower. Additionally, with respect to Figure 4.7 (b), the evident rise in the Reynolds stress from the rotor may be due to the blade root section. That is, the increase in production of TKE may be caused by the thicker blade cross section. The strength of the vortex system in the tower wake does not appear to dissipate much, which implies that turbulence production by tower vortex shedding is a continuous phenomenon. Figure 4.19 (b) also shows that the Reynolds stress returns to upstream levels beyond $y/R = \pm 0.6$.

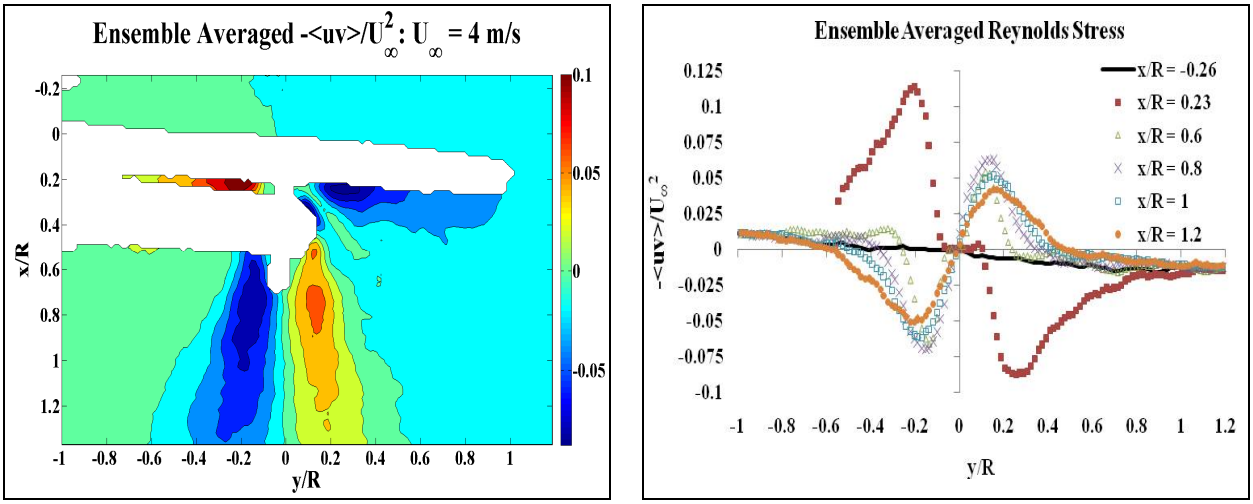

(a) **(b)**

Figure 4.19: Ensemble averaged Reynolds stress normalized by U_∞^2 **(a)** Contour plot **(b)** Spanwise distribution.

Figure 4.20 shows normalized phase averaged Reynolds stress plots; the spanwise distribution profiles display only the magnitudes. A phase of 60 degrees is omitted as the general features are

similar to those at 30 degrees. Individually, the blade effects are observed to be marginally weaker than in ensemble averaging, while the Reynolds stress from the cylinder is virtually the same: it is highly symmetric about the centerline. At a lower wind speed of 3.22 m/s, Figure 4.21 reveals a slight reduction in normalized Reynolds stress. This is likely caused by a lower tip speed ratio, and thus a smaller turbulent rotor wake. In both ensemble and phase averaging, the Reynolds stress produced by the cylinder and the subsequent slow decay, offer a reasonable explanation for the persistence in crosswind turbulence intensity.

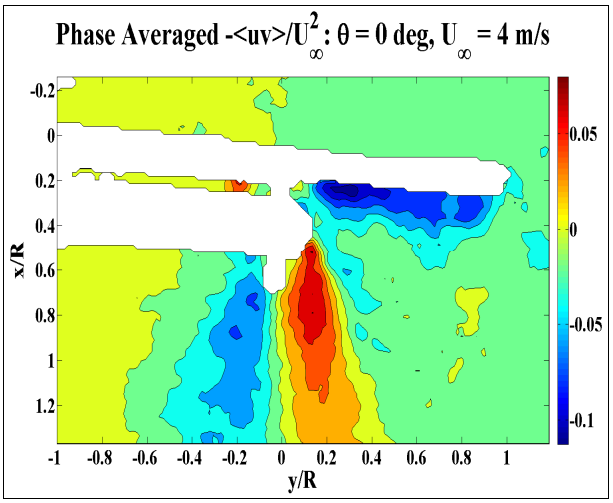

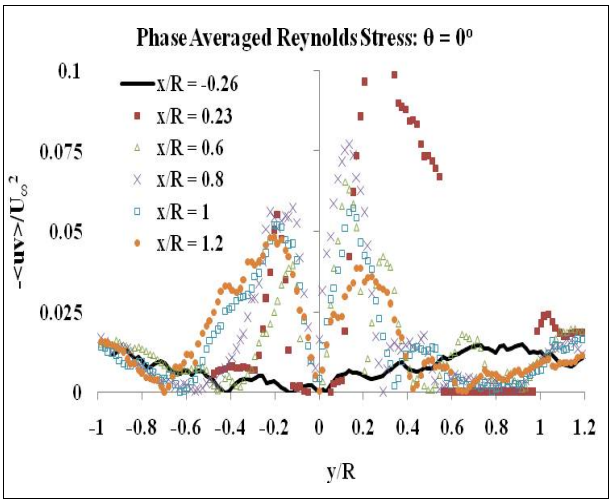

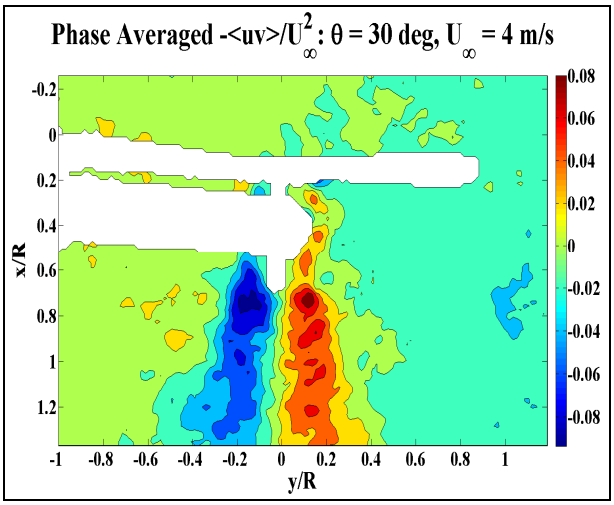

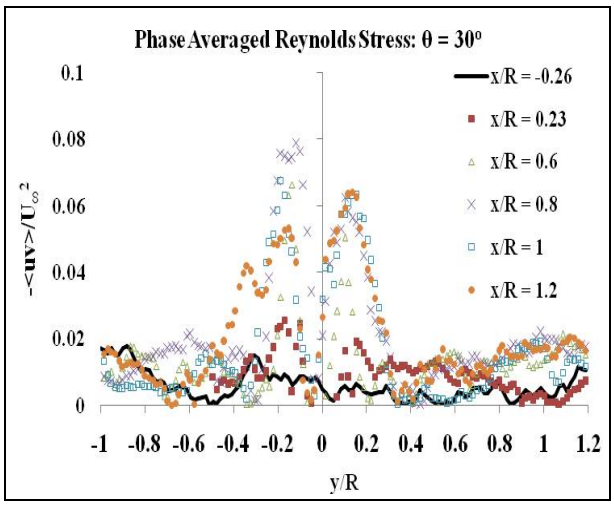

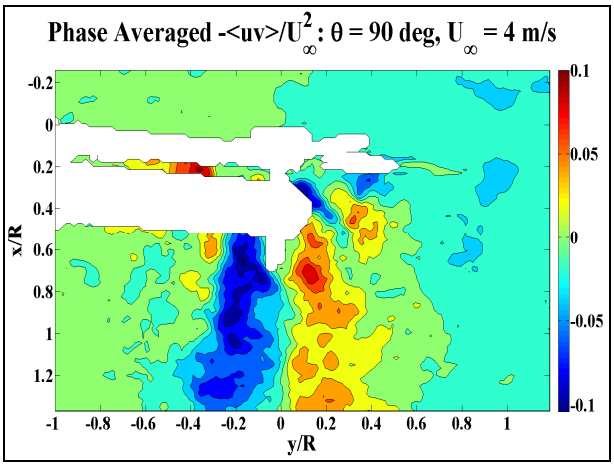

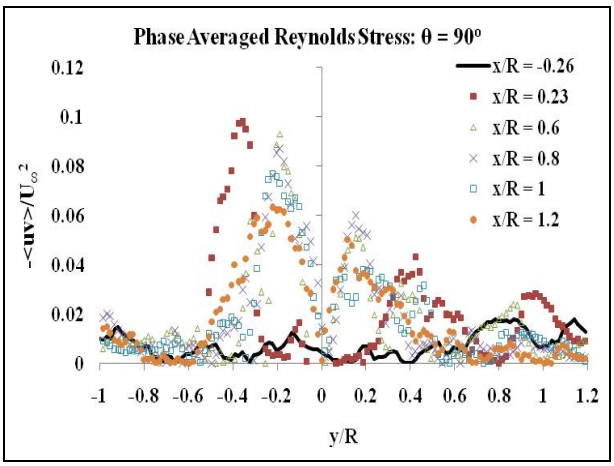

Figure 4.20: Phase averaged Reynolds stress normalized by U_∞^2 **(left)** Contour plots **(right)** Spanwise distribution of absolute values.

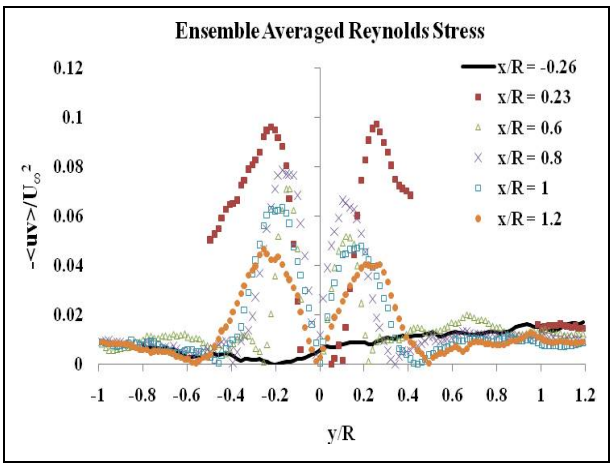

(a)

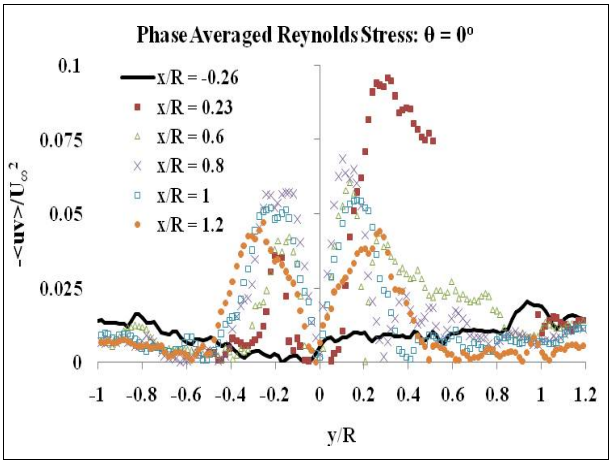

(b)

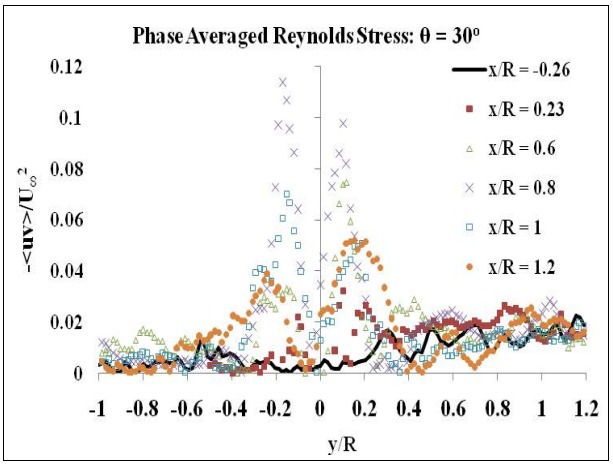

(c)

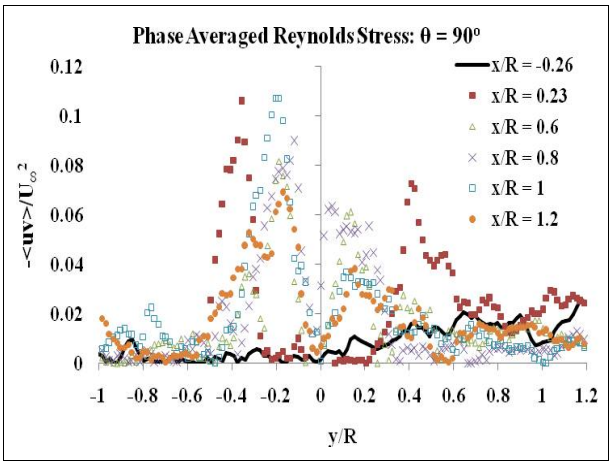

(d)

Figure 4.21: Normalized Reynolds stress at a wind speed of 3.22 m/s **(a)** Ensemble average **(b)** 0 degrees **(c)** 30 degrees **(d)** 90 degrees.

4.2.5 Spectral Analysis

The ensemble averaged streamwise wavenumber spectra at two wind speeds are presented in Figure 4.22 as a function of downstream position. Each spectrum resolved wavenumbers from about 38 rad/m to 2400 rad/m with a resolution of 37.5 rad/m. The corresponding length scales are from 167 mm to 2.6 mm. The minor difference in wavenumbers at this height, compared to 0.185 m, is due to the camera magnification factor. No bulge of energy input from the blades in the near-wake region, previously observed at 0.185 m, can be discerned in the spectra. However, the overall energy level at each downstream location is higher with respect to 0.185 m. This indicates that the tower redistributes the energy input from the blades (i.e. initially over a specific range of length scales) over a wider range of length scales. A small surge in spectral energy at $x/R = 0.59$ (immediately behind tower) is observed in the wavenumber region close to 500 rad/m which is on the order of the tower diameter, at both wind speeds. This corresponds to the energy added to the turbulent flow by the tower.

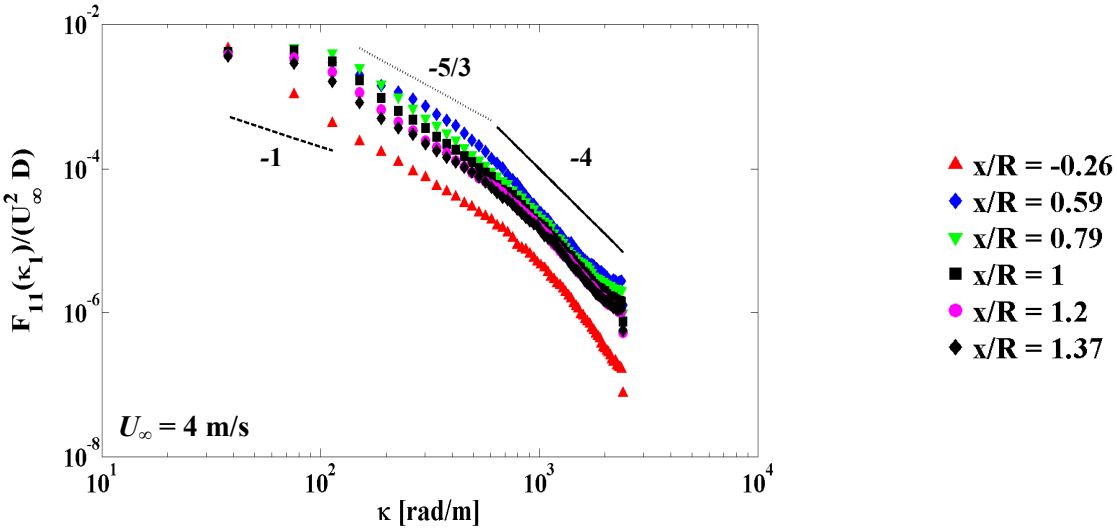

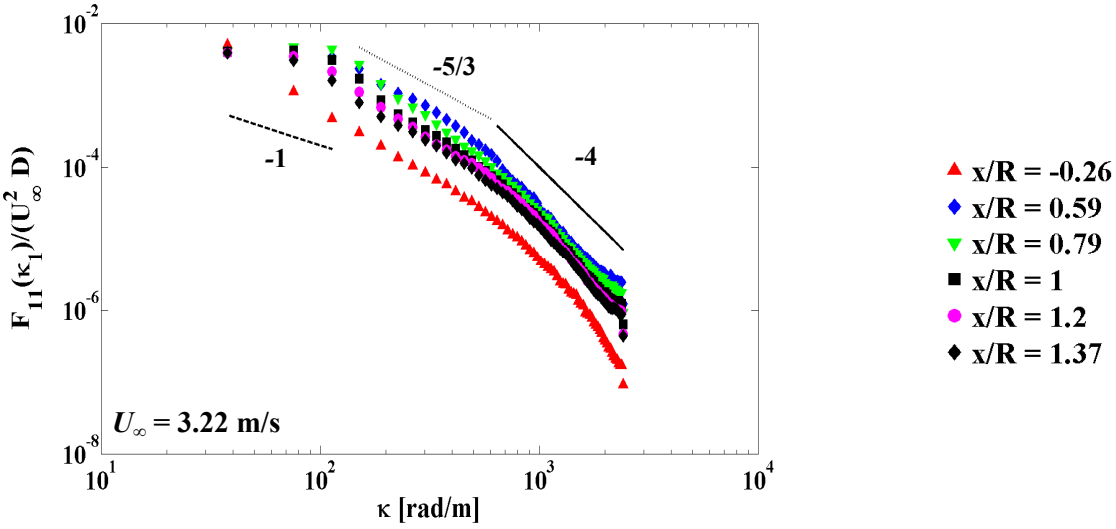

Figure 4.22: Ensemble averaged streamwise wavenumber spectra normalized by $U_\infty^2 D$ at wind speeds of 4 and 3.22 m/s.

The plots also show that the inertial subrange exists between 120 rad/m to 400 rad/m, which is similar to that at a height of 0.185 m. Furthermore, the inertial subrange grows steadily with downstream position, extending to 500 rad/m at x/R = 1.37.

The normalized ensemble averaged crosswind spectra at the two wind speeds are exhibited in Figure 4.23. Similar level of spectral energy is observed at different downstream locations over the entire spectrum except a small surge, which corresponds to the energy input due to the tower as discussed earlier. The inertial subrange extends from about 75 rad/m to 450 rad/m. Table 4.3 provides spectral energy ratios of the largest wave, corroborating results that detailed the pervasiveness of the crosswind turbulence intensity. Beyond one blade length downstream, vortices corresponding to a size of 0.16 m, or approximately the turbine diameter, contain crosswind turbulent kinetic energy that is much greater than the motions in the streamwise direction. This finding holds fundamental implications on dynamic structural loads of downwind turbines inside an array, and correct energy yield predictions. Thus, it would be a serious

mistake, in future studies, to neglect the support tower's impact on turbulent wake parameters below hub height.

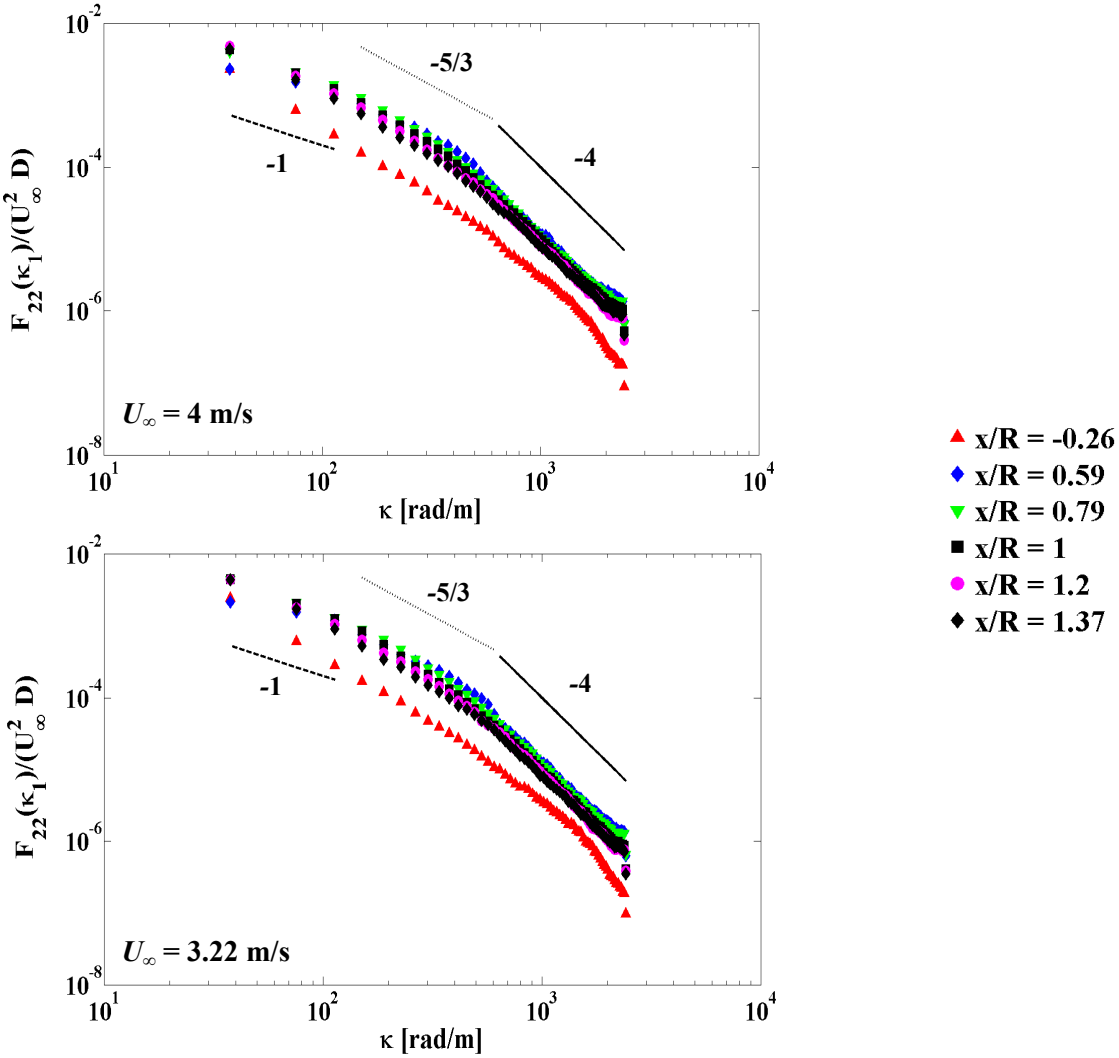

Figure 4.23: Ensemble averaged crosswind wavenumber spectra normalized by $U_\infty^2 D$ at wind speeds of 4 and 3.22 m/s.

Table 4.3: Ratio of spectra at lowest wavenumber for wind speeds of 4 m/s and 3.22 m/s

x/R	**-0.26**	**0.59**	**0.79**	**1**	**1.2**	**1.37**
$F_{11}(37.8)/F_{22}(37.8)$ U_∞ = 4 m/s	2.0	1.13	1.04	0.94	0.79	0.84
$F_{11}(37.8)/F_{22}(37.8)$ U_∞ = 3.22 m/s	2.07	1.08	1.03	0.90	0.89	0.88

Normalized phase averaged streamwise spectra are displayed in Figure 4.24 at axial positions of 0.7 *R, R*, and 1.37 *R.* At each axial location, the spectra show nearly identical profiles at all phases, signifying the scales at which energy is transmitted by the blades (previously noted at the height of 0.185 m, see Figure 4.12) are distorted by the tower. One interesting feature in the spectra at x/R = 0.7 and x/R = 1, is the spectral peak that occurs at about 80 rad/m, which corresponds to the energy containing eddies of length scale 75 mm, or equivalent to one blade length (half of the rotor diameter).

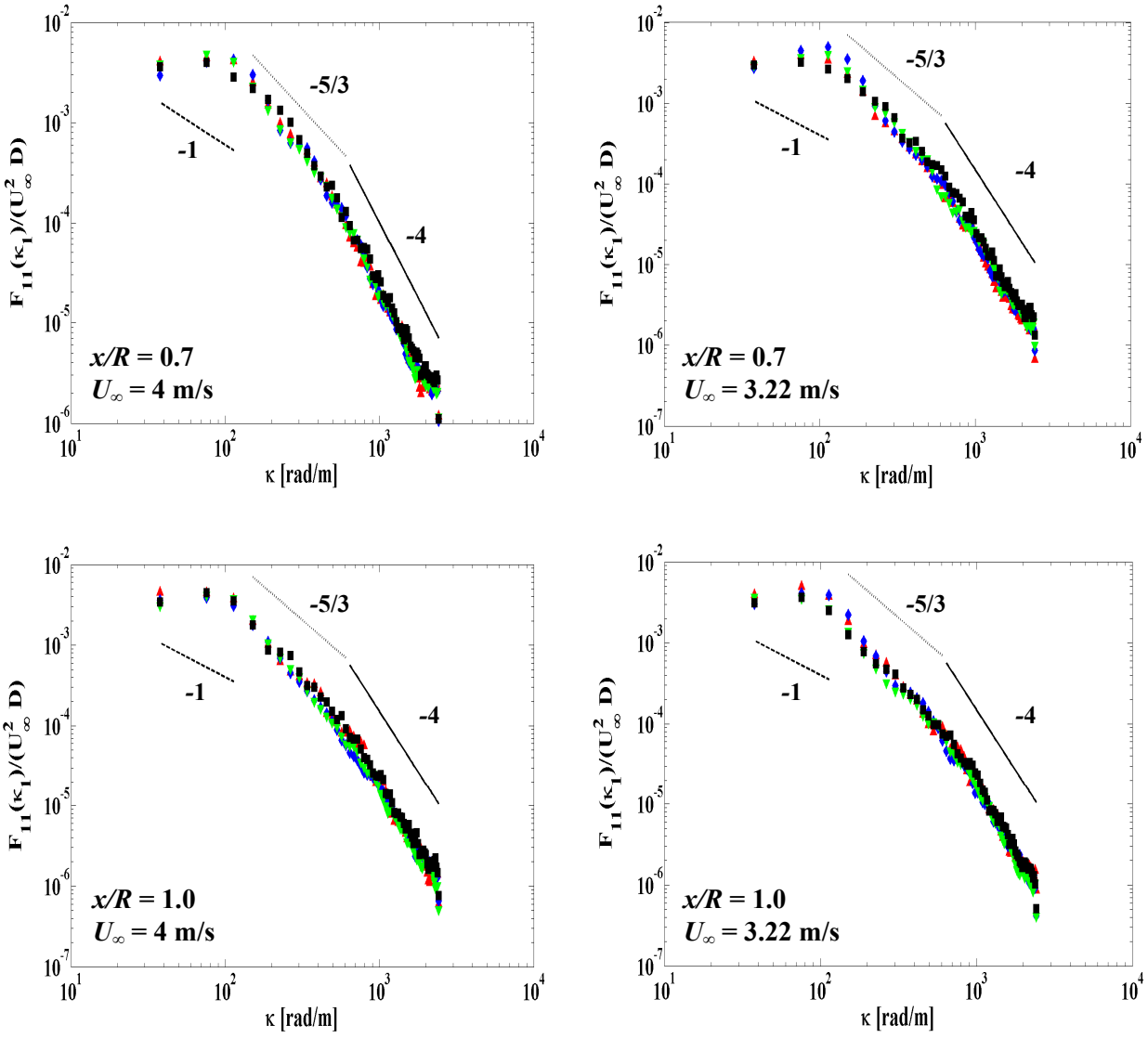

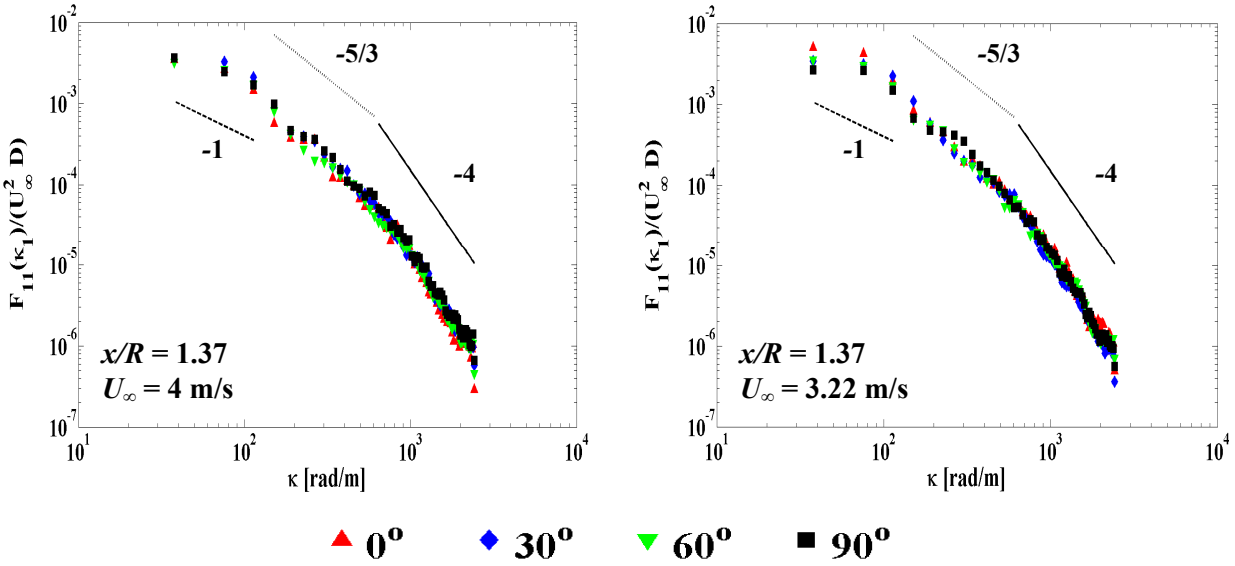

Figure 4.24: Phase averaged streamwise wavenumber spectra normalized by $U_\infty^2 D$ at wind speeds of 4 and 3.22 m/s.

The results in Figure 4.24 suggest that the tower breaks down the energy containing eddies into motions having dimensions comparable to half the rotor diameter. This result further highlights the role played by the tower in controlling the flow dynamics in the near-wake region. In addition, the plots show that the band of wavenumbers covered by the inertial subrange is relatively the same as in the previous cases.

Figure 4.25 depicts normalized phase averaged crosswind spectra at wind speeds of 4 m/s and 3.22 m/s, at axial distances of 0.7 *R, R*, and 1.37 *R*. In general, the spectra show similar trend at different phases. The energy containing eddies are not resolved and the inertial subrange extended up to the lowest wavenumber of 38 rad/m.

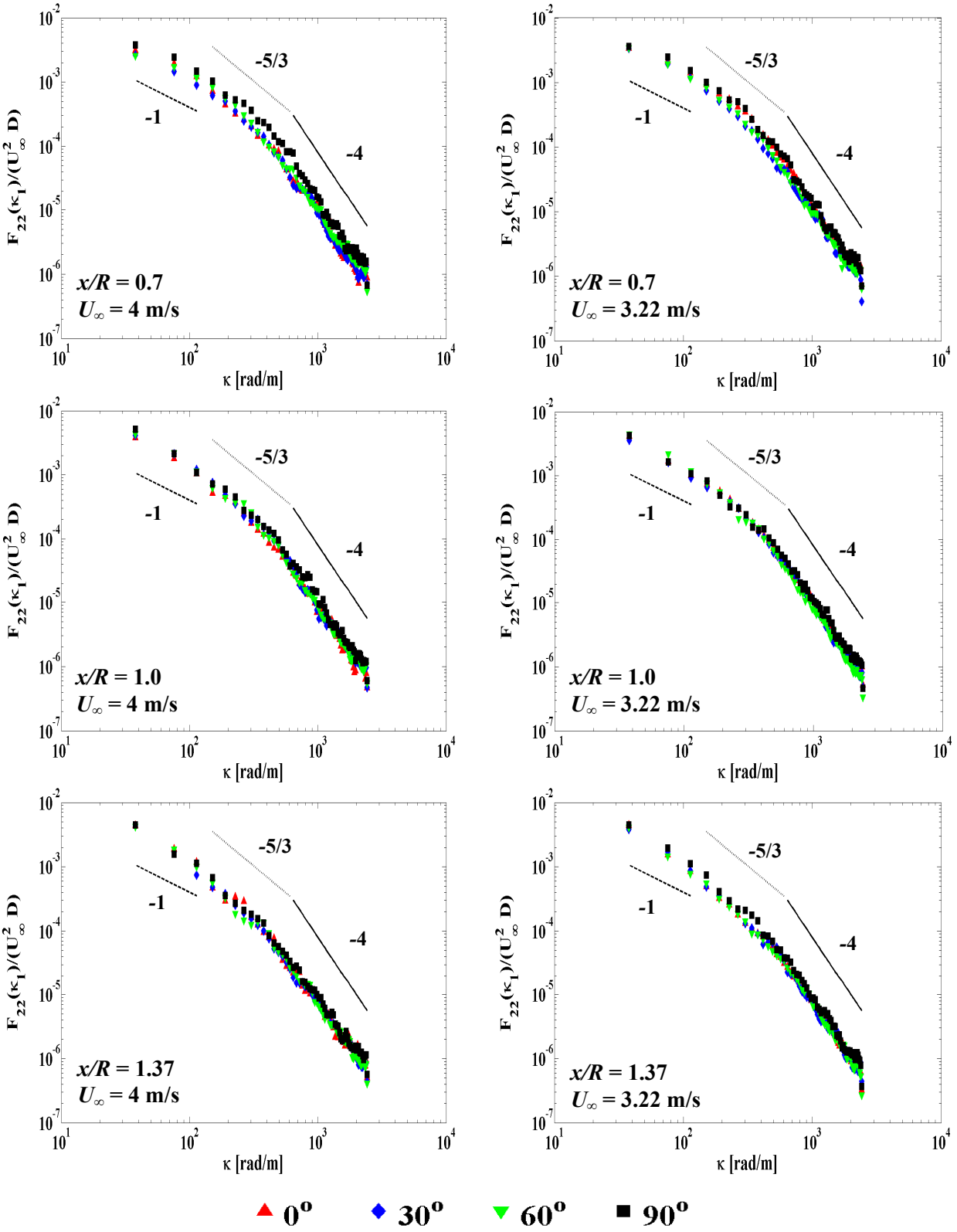

Figure 4.25: Phase averaged crosswind wavenumber spectra normalized by $U_\infty^2 D$ at wind speeds of 4 and 3.22 m/s.

4.3 Measurements at z = 0.05 m

As discussed previously in Chapter 3, the flow field at the height of 0.05 m is induced by the 3-D vortex system of the tower. The interest here is to understand its effect on turbulence intensity, Reynolds stress and turbulent length scales. Recall that as the measurement plane lies beneath the rotor, the latter properties are described by ensemble averaging. Furthermore, only observations at the highest wind speed of 4 m/s are discussed since the important flow features are indistinguishable at the lowest wind speed of 3.22 m/s.

4.3.1 Ensemble Averaged Turbulence Intensity

With the rotor wake absent, flow separation is better defined in Figure 4.26 (a) than in Figure 4.14 (a). Enhancement of the streamwise turbulence intensity is clearly caused by the tower's trailing vortices. In relation to the ensemble averaged crosswind turbulence intensity, presented in Figure 4.26 (b), the flow bounding the lateral surface of the tower is absent because the turbine interference is decoupled from it. An elevated level of I_v emerges within the core of the tower wake, developing into a shape similar to Figure 4.14(b), but with larger magnitudes.

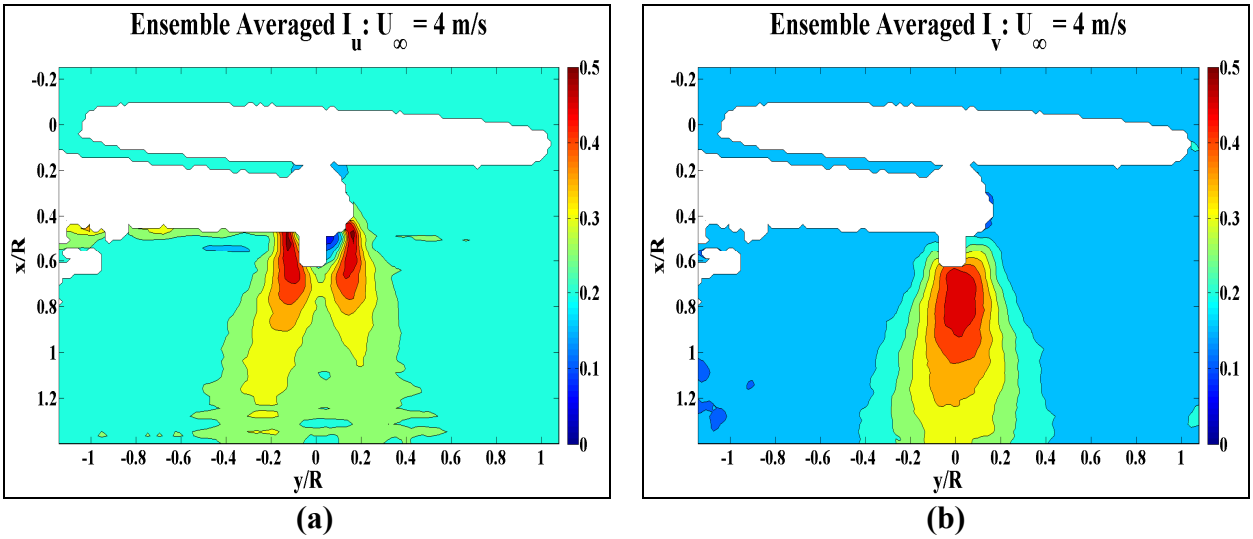

(a) **(b)**

Figure 4.26: Ensemble averaged turbulence intensity contour plots at $U_\infty = 4$ m/s **(a)** Streamwise **(b)** Crosswind

Figure 4.27 presents the spanwise variation of streamwise and crosswind turbulence intensities at 0.05 m for U_∞ = 4 m/s; data at 0.185 m and 0.135 m are also plotted for comparison. At x/R = 0.6, corresponding to a wake position immediately behind the tower, the centerline values of I_u and I_v exhibited in the isolated tower wake significantly exceeds those at the middle height. This implies that flow interaction between rotor and tower hinders the formation of the helical vortex sheet. Farther downstream, at x/R = 1.2, centerline I_u and I_v dissipate to values comparable to 0.135 m. This result strongly reflects the characteristic of increased momentum mixing associated with a higher degree of turbulence. Consequently, this explains why the centerline U/U_∞ recovered quicker at 0.05 m than at 0.135 m (see Figure 3.15).

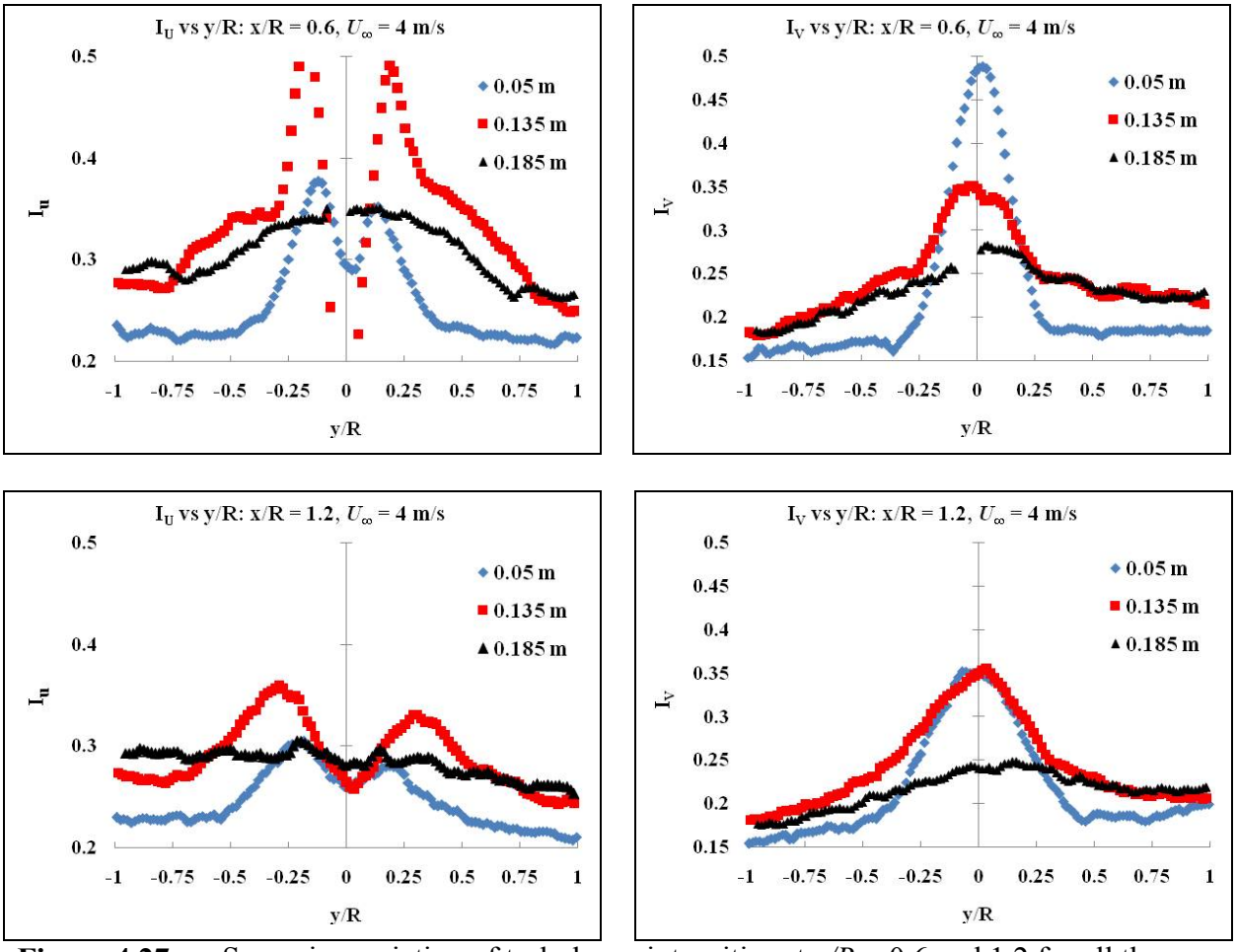

Figure 4.27: Spanwise variation of turbulence intensities at x/R = 0.6 and 1.2 for all three heights **(left)** Streamwise (**right)** Crosswind.

The twin peaks in the streamwise component of turbulence intensity, at x/R = 0.6 and 1.2, identify vortex shedding from the tower. Beginning about $y/R = \pm 0.4$, enhancement of both I_u and I_v is dictated by the rotor induced motions (i.e. helical vortex sheet), which is unsurprisingly absent in the lone tower wake.

4.3.2 Ensemble Averaged Reynolds Stress

The Reynolds stress generated about the tower is highly symmetric, and is illustrated in Figure 4.28. From the spanwise distributions, it is determined that the Reynolds stress increases relative to a height of 0.185 m and 0.135 m at identical streamwise positions. As the vortex flow weakens behind the tower with wake distance, the peaks in Reynolds stress decrease along with a broadening of the area of enhanced turbulence production. The influence of the rotor on turbulence production is observed for heights of 0.185 m and 0.135 m, in which the tail ends of their profiles are greater than the isolated tower. It can be deduced that the absence of opposing Reynolds stresses between rotor and tower is the probable cause of increased levels in both centerline values of I_u and I_v downstream the tower.

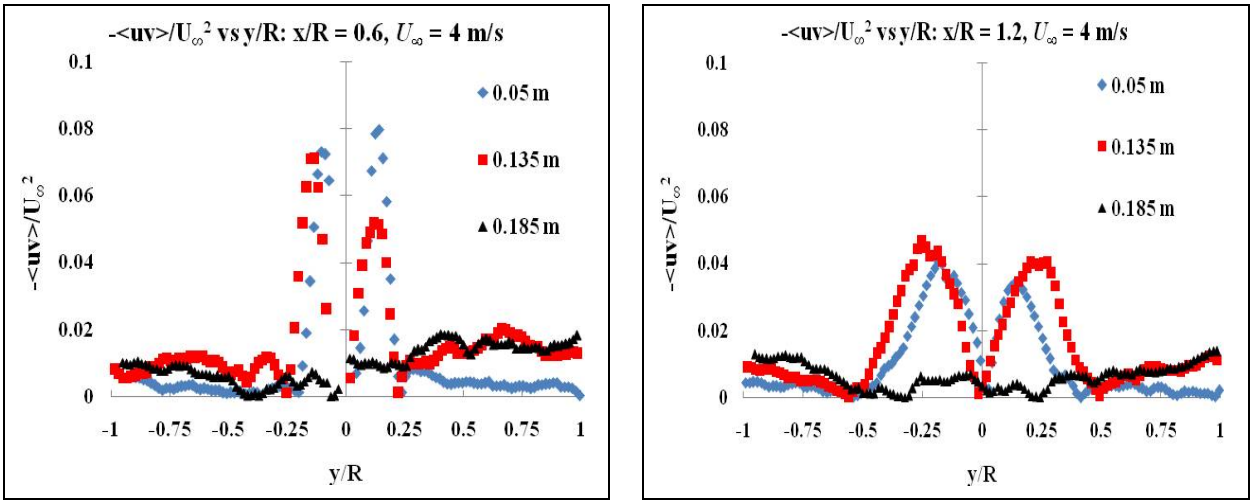

Figure 4.28: Spanwise distribution of absolute valued ensemble averaged Reynolds stress at all heights.

4.3.3 Spectral Analysis

The wavenumber spectra of the streamwise and crosswind components of turbulent velocity are presented in Figure 4.29 at x/R = 0.6. In order to identify the characteristics of turbulent scales at this height, ensemble averaged wavenumber spectra at the other two measurement planes are plotted, as well. The spectra of streamwise velocity in Figure 4.29 (a) show that their shape in the high wavenumber range are similar at all three hights, although the energy levels are different. At low wavenumbers with scales up to almost the blade length, the streamwise energy densities are higher at the height of 0.185 m, as the flow is governed by the rotor wake. As the wavenumber increases, spectral energy at the height of 0.185 m decreases relatively sharply and become lower than that at the heights of 0.135 m and 0.05 m, where the flow experiences tower inference. This indicates that the energy is contained at larger scales where the wake is not influenced by the tower, and as mentioned earlier, the tower tends to redistribute the turbulent energy over a wider range of scales. At a height of 0.05 m, a band of wavenumbers, demarcated by the dashed lines, forms a plateau coinciding to waves measuring 0.02 m to 0.012 m. This observation is interesting since the pole diameter lies within the range, and the occurence is not viewable at 0.135 m and 0.185 m. The crosswind component of turbulent velocity at a height of 0.05 m, see Figure 4.29 (b), is largest at the lower end of the spectrum. This supports the observation that crosswind turbulence intensity is most intense under the sole effect of the tower wake.

Farther downstream in the near wake at x/R = 1.3, shown in Figure 4.30, the uniformity in the spectral energy profiles at the three heights is evident. A severe decline, compared to Figure 4.29, of spectral energy is observed in the wavenumber range between 40 rad/m to 320 rad/m. This drop off in energy is probably associated with the breakdown of eddies stemming from both

the rotor and tower. In the wavenumber range 200 rad/m to 800 rad/m, the spectral energy is relatively higher at the height of 0.135 m, which is likely due to the effect of vortex interaction between the joint wakes.

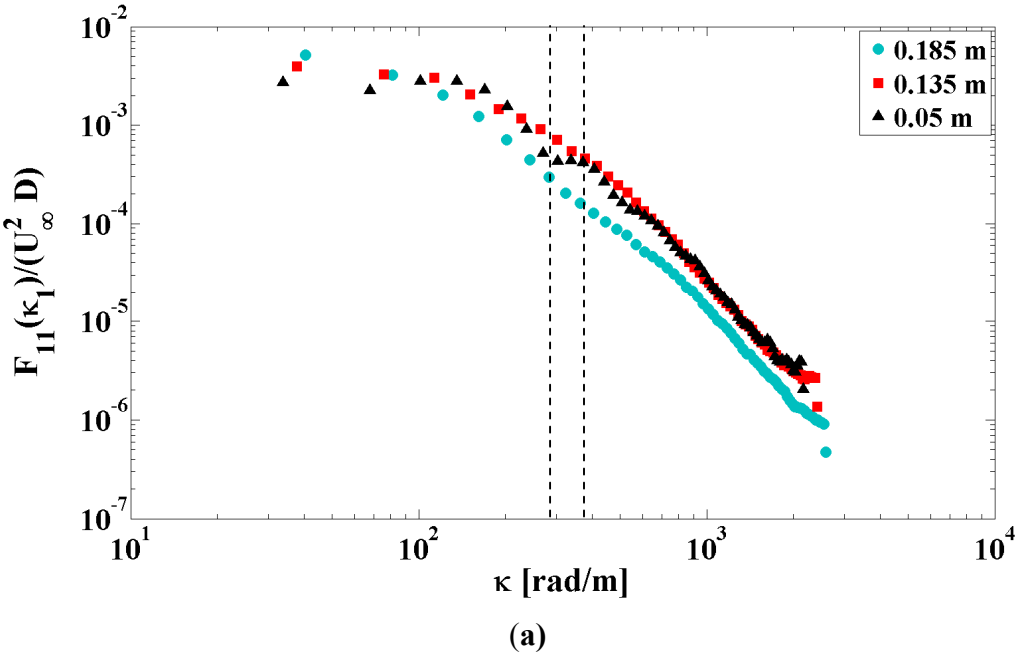

Figure 4.29: Ensemble averaged wavenumber spectra normalized by $U_\infty{}^2 D$ at x/R = 0.6 **(a)** Streamwise **(b)** Crosswind.

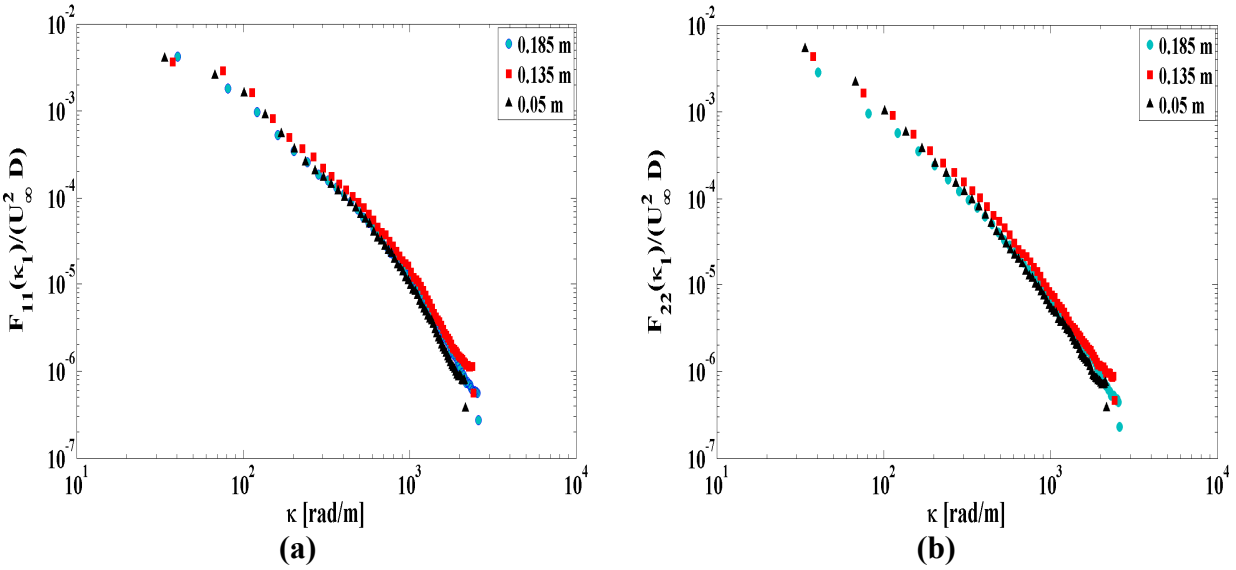

Figure 4.30: Ensemble averaged wavenumber spectra normalized by $U_\infty{}^2D$ at x/R = 1.3 **(a)** Streamwise **(b)** Crosswind.

4.4 Conclusion

Characterization of the turbulence in the rotor wake was conducted with ensemble and phase averaged analyses of the turbulence intensities, Reynolds stress, and wavenumber spectra at heights of 0.185 m, 0.135 m, and 0.05 m. The nature of the near wake field was observed to react quite differently under the induced turbine flow, wake mixing between the pole and rotor, and the pole in isolation.

4.4.1 Measurements at a Height of 0.185 m

When considering just the rotor wake, the profiles of ensemble averaged turbulence intensities demonstrated that the streamwise component weakened away from the wake center, whereas the crosswind fluctuations strengthened in a region self-described as the core. Both appeared to be quite axisymmetric. Cross referencing several studies with I_u^+, the added streamwise turbulence intensity, indicated that I_∞, the freestream turbulence intensity, should be incorporated as a more

critical factor for modelling the near wake decay of the fluctuations. Unsteadiness of the near wake flow was underlined by phase averaging. Each phase revealed that turbulence enhancement was localized behind the blade, and that the strength of the trailing vortex varied between rotor configurations.

Ensemble averaged Reynolds stress was observed to increase near the edge of the wake, as shear is mostly produced in the vicinity. Its profile varied linearly from positive to negative stress, and the sign convention was attributed to be a function of the crosswind velocity. The spanwise profiles of phase averaged Reynolds stress showed that the quantity of produced turbulence was at least two times larger than the ensemble averaged plot. Furthermore, the regions of amplified Reynolds stress conformed to the structure of the trailing vortex cores behind individual blades.

The study of wavenumber spectra focused on the relationship between production of turbulent kinetic energy, and the physical eddy scales related to these processes. The profiles of ensemble averaged wavenumber spectra confirmed the ubiquitous notion of the turbulent cascade. That is, spectral energy was shown to decay from low wavenumbers (production scales) to high wavenumbers (dissipation scales). The presence of a low wavenumber bump, equivalent to scales on the order of the blade length, in the spectra for the streamwise fluctuations indicated that TKE entered through this component of turbulence. Conversely, the absence of the bump in crosswind spectra meant that TKE was redistributed to other velocity components. Moreover, large scale motions were determined to be anisotropic at the beginning of the wake. The inertial subrange formed in an intermediate range of wavenumbers at axial locations farther away from the rotor. Phase averaged wavenumber spectra helped identify the non-uniformity in the vortex pair strength between phases, and clarified growth of the inertial subrange with wake position.

4.4.2 Measurements at a Height of 0.135 m

The dual wakes of the support tower and turbine exerted minor perturbations to the streamwise turbulence intensity at the centerline. The crosswind turbulence intensity, on the other hand, experienced significant augmentations. Phase averaged profiles of turbulence intensity emphasized that rotor shed vorticity was indeed stronger than those from the pole. However, the separated flow from the cylinder demonstrated greater resistance towards dissipation. As such, this raised concerns that non-axial components of the turbulent fluctuations be treated cautiously below hub height.

The Reynolds stress exhibited an improved symmetric profile, and larger magnitudes of ensemble averages in relation to those at a height of 0.185 m. Shear produced by the rotor wake was noted to be opposite in sign to the support tower, and had greater peak values to some extent. The sustained level of Reynolds stress in the tower wake, and thus turbulence production, may be correlated to the persistence in crosswind turbulence intensity.

The behaviour in wavenumber spectra appeared significantly more uniform throughout the near wake, particularly in the streamwise direction. This resulted in the appearance of an inertial subrange in all axial locations that were surveyed. As the level of spectral energy declined with downstream location, the inertial subrange extended to higher and lower wavenumbers. The tower was observed to spread the influx of spectral energy, from the rotor, to a wider range of scales. In addition, after a certain distance downstream, the largest scale in the flow contained higher spectral energy in the crosswind direction. Phase averaged results showed that the profiles all collapsed at a scale roughly measuring the size of the support tower diameter.

4.4.3 Measurements at a Height of 0.05 m

The tower wake in isolation provided a better defined structure in the ensemble averaged turbulence intensity contours. The streamwise fluctuations in the vortex flow had similar intensities to those at a height of 0.135. A drastic enhancement to the crosswind turbulence was noted behind the tower in the core region. This occurrence suggested that flow interaction between the tower and turbine, which increased the crosswind turbulence intensity at centerline too, paled in relation to the singular influence of the support tower. The aforementioned result was further supported by the ensemble averaged profiles of Reynolds stress, which revealed that the quantity of turbulence production was highest for the isolated tower. At equal distances from the rotor, ensemble averaged wavenumber spectra at this height demonstrated the following characteristics: contained the second highest streamwise energy density, had the largest crosswind spectral energy at lower wavenumbers, but decayed more quickly in the absence of the rotor wake.

Chapter 5: Conclusions

The present study focused on the investigation of flow behaviour in the near-wake region of a Horizontal Axis Wind Turbine (HAWT). State of the art PIV technique was used to measure the two-dimensional velocity field at three heights and at different freestream velocities. The tip speed ratio (λ) varied from 3.5 - 4.25 and chord Reynolds number varied between 1900 – 2500. The scale model HAWT consisted of a rotor with a diameter of 0.15 m, and a cylindrical tower with a diameter of 16 mm. The scarcity of data in the literature provided an enormous opportunity to develop an approach for the task of improving our understanding of this flow regime. Outlined in Chapter 1, the primary objective was to face the abovementioned challenge by investigating flow phenomena through two means: ensemble averaging, and more importantly, phase averaging. The two methods were extended to three heights, accounting for wake perturbations from the rotor (z = 0.185 m), cylindrical tower and rotor (z = 0.135 m), and the tower in isolation (z = 0.05 m).

An algorithm was developed to compute the phases corresponding to different blade positions from the PIV images. The velocity data were binned according to the phases and averaged to arrive at the phase-averaged flow properties. The main advantage achieved with phase averaging was the preservation of transience in the wake flow. This was best demonstrated when it validated the link between the law of mass conservation (Eq. 1.1) and the observed behaviour in streamwise velocity. Specifically, the reasoning behind the zones of flow acceleration at different phases was made clear. Furthermore, the advection of vorticity from individual blades was shown to relate strongly in shape to the streamwise turbulence, which was not perceptible with ensemble averaging.

Sanderse [64] reported that the rate of decay of velocity deficit was dependent on freestream and mechanical (turbine generated) turbulence. The present results of velocity deficit and turbulence intensity concurred, but elaborated on key ideas too. From the vertical distribution of data (i.e. three measurement planes), both streamwise and crosswind turbulence were non-uniform. The profiles of added streamwise turbulence intensity indicated that the ambient conditions had a major influence on the dissipation rate. The increase of crosswind turbulence in the separated flow behind the tower, decoupled from the rotor, translated into a quicker recovery of momentum in the streamwise direction. Thus, in wind farm modelling applications, concerns raised by the support tower regarding energy availability to downwind rotors must be carefully considered.

The profiles of Reynolds stress displayed significant enhancement immediately downstream of blades and tower indicating the enhanced production of turbulent kinetic energy (TKE). An enhancement of Reynolds stress by factors of 2 - 4 was observed behind the blades and the tower. Comparison of Reynolds stress magnitude generated by blades only, blades and tower, and tower only, showed significantly higher magnitudes of Reynolds stress due to the presence of the tower. This signifies that the tower has a significant influence on the turbulent flow structure in the near-wake region.

One of the main topics alluded to was the concept of the turbulent energy cascade. This was addressed through the spectral analysis. The wavenumber spectra were computed for both streamwise and crosswind velocity components in the crosswind direction at various axial locations. Since the important physical scales of turbulence in the wake were resolved, its subsequent analysis was relatively intuitive. The result provided the first quantitative estimate of the scales at which energy is injected into the turbulence by the blades and tower. It has been

shown that the overall influx of TKE occurred at a scale slightly larger than the turbine diameter, and progressively diminished at larger wavenumbers (smaller scales). The transfer of TKE into the velocity fluctuations was further highlighted by protrusions in the streamwise spectrum, at scales comparable to the blade length and tower diameter. Formation of vortices across the rotor and on the periphery of the tower added to the existing anisotropy of the incident flow, at scales equal to or larger than the blade length. However, a range of locally isotropic scales, of intermediate size, developed further downstream in the wake. Its growth was observed to depend on the various wake sources, but the present results indicated a wider locally isotropic band of scales behind the tower. Results of crosswind spectra below hub height deduced that the energy of the turbulent fluctuations surpassed those in the dominant flow direction, for eddies spanning the rotor diameter. Thus, it stipulates a strict specification of the 3-dimensional dynamic loads, below hub height, to avoid premature blade and tower fatigue for downwind turbines.

There are several options to advance the present work. Since only two of the three components of turbulent fluctuations were measured, it would be important to measure the velocity component in the z-direction by establishing vertical PIV measurement planes. The tower wake was shown to be quite persistent; obtaining more information about its evolution could be done by extending the field of view in the near wake. Field wind turbines are situated in a number of different environments, so a study of topographical elements (i.e. hills, trees, water, and residential homes) and their impact on the incident mean and turbulent flows would be highly appealing. Another ambitious approach would be to erect a second rotor downstream and investigate both the far-wake (of the first turbine) and the altered inflow conditions of the downwind turbine. Lastly, the environmental aspect of the large scale motions (i.e. tip vortices)

is their emission of low frequency noise. Conducting a noise impact assessment can help determine the factors that either attenuate or augment the sound pressure level [65].

5.1 Contribution to Knowledge

The method of phase averaging provided crucial observations on vortex shedding patterns and flow kinematics, which were not possible via ensemble averaging because of the smoothing effect. Consequently, the correlation between the structure of turbulence and vortex shedding was high. As fundamental characteristics in turbulent flows are the multitude of time and length scales involved, the current study took aim at a novel approach by studying wavenumber spectra in both ensemble and phase averaged forms. The results gathered from the spectra permitted a detailed understanding of how TKE, at various length scales, evolved in the near wake. Previous studies placed an emphasis on rotor geometry being the predominant factor in shaping the near wake. However, current results suggested that the freestream turbulence intensity had some influence on the dissipation rate of both streamwise and crosswind turbulence. Moreover, by investigating the tower effect, it was determined that the fluctuations in the non-axial direction were even more crucial. These findings may be implemented in wake farm modelling to better simulate energy yields.

References

1 Heier S. *Grid Integration of Wind Energy Conversion Systems 2nd ed.* Chichester: John Wiley & Sons, Ltd., 2006

2 Ackermann T., Soder L. "Wind Energy Technology and Current Status: A Review" Renewable & Sustainable Energy Reviews 4 (2000): 315-374

3 EWEA. "GWEC Press Release: Tables and Statistics – 2008" Statistics: Global Statistics 9 Feb. 2009. Accessed 1 Feb. 2010. <www.ewea.org/fileadmin/ewea_documents/documents/press_releases/2009/GWEC_Press_Release_-_tables_and_statistics_2008.pdf>

4 Crespo A., Hernandez J., Frandsen S. "Survey of Modelling Methods for Wind Turbine Farms" Wind Energy 2 (1999): 1-24

5 Snel H. "Review of Aerodynamics for Wind Turbines" Wind Energy 6 (2003): 203-211

6 Vermeer L.J, Sorensen J.N, Crespo A. "Wind Turbine Wake Aerodynamics" Progress in Aerospace Sciences 39 (2003): 467-510

7 Snel H. "Review of the Present Status of Rotor Aerodynamics" Wind Energy 1 (1998): 46-69

8 Tennekes H., Lumley J.L. *A First Course in Turbulence.* Cambridge: The MIT Press, 1972

9 Hansen, M.O.L. *Aerodynamics of Wind Turbines 2nd ed*. Sterling: Earthscan, 2008

10 Fox R.W., McDonald A.T., Pritchard P.J. *Introduction to Fluid Mechanics 6th ed.* New York: Wiley, 2003

11 Magnusson M., Smedman A.S. "Air Flow Behind Wind Turbines" Journal of Wind Engineering and Industrial Aerodynamics 80 (1999): 169-189

12 Buhl Jr. M.L. "A New Empirical Relationship Between Thrust Coefficient and Induction Factor for the Turbulent Windmill State" *NREL Report*, 2005

13 Anderson J.D. *Fundamentals of Aerodynamics 4th ed.* McGraw-Hill, 2007

14 Burton T., Sharpe D., Jenkins N., Bossanyi E. *Wind Energy Handbook.* Chichester: John Wiley & Sons, Ltd., 2001

15 Whale J., Anderson C.G., Bareiss R., Wagner S. "An Experimental and Numerical Study Of The Vortex Structure In The Wake Of A Wind Turbine" Journal of Wind Engineering and Industrial Aerodynamics 84 (2000): 1-21

16 Troldborg N., Sorensen J.N., Mikkelsen R. "Numerical Simulations of Wake Characteristics of a Wind Turbine in Uniform Inflow" Wind Energy 13 (2009): 86-99

17 Whale J., Anderson C.G. "The Application of Particle Image Velocimetry to Wind Turbine Wakes" *Laser Anemometry, Advances and Applications: Proceedings of the 5th International Conference, Koningshof, August 1993. Eds. J. Bessem et al. Bellingham: SPIE, 1993, 667-67*

18 Magnusson M. "Near-Wake Behaviour of Wind Turbines" Journal of Wind Engineering and Industrial Aerodynamics 80 (1999): 147-167

19 Ebert P.R., Wood D.H. "The Near Wake Of A Model Horizontal-Axis Wind Turbine-I. Experimental Arrangements and Initial Results" Renewable Energy 12 (1997): 225-243

20 Whale J., Papadopoulos H., Anderson C.G., Helmis C.G., Skyner D.J. "A Study of the Near Wake Structure of a Wind turbine Comparing Measurements From Laboratory and Full-Scale Experiments" Solar Energy 56 (1996): 621-633

21 Simoes F. J., Graham J.M.R. "Application of a Free Vortex Wake Model to a Horizontal Axis Wind Turbine" Journal of Wind Engineering and Industrial Aerodynamics 39 (1992): 129-138

22 Savino J.M., Nyland T.W. "Wind Turbine Flow Visualization Studies" *Proceedings of the Windpower '85 Conference. Washington, DC: AWEA, 559-564*

23 Whale J., Anderson C.G. "An Experimental Investigation of Wind Turbine Wakes Using Particle Image Velocimetry" *European Community Wind Energy Conference: Proceedings of the International Conference, Lübeck-Travemünde, March 1993.* Eds. A.D. Garrad, W. Palz, and S. Scheller. Bedford: 1993, 457-460

24 Grant I., Mo M., Pan X., Parkin P., Powell J., Reinecke H., Shuang K., Coton F., Lee D. "An Experimental and Numerical Study of the Vortex Filaments in the Wake of an Operational Horizontal-Axis Wind Turbine" Journal of Wind Energy and Industrial Aerodynamics 85 (2000): 177-189

25 Infield D.G., Grant I., Smith G., Wang X. "Development of Particle Image Velocimetry for Rotor Flow Measurement" *Wind Energy Conversion 1994: Proceedings of the 16th BWEA Conference, Stirling, September 1994.* Ed. G. Elliot. London: Mechanical Engineering Publications, 1994, 73-78

26 Grant I., Parkin P. "A DPIV Study of the Trailing Vortex Elements From the Blades of a Horizontal Axis Wind Turbine in Yaw" Experiments in Fluids 28 (2000): 368-376

27 Hossain M.Z., Hirahara H., Nonomura Y., Kawahashi M. "The wake structure in a 2D grid installation of the horizontal axis micro wind turbines" Renewable Energy 32 (2007): 2247-2267

28 Ebert P.R., Wood D.H. "The Near Wake of a Model Horizontal-Axis Wind Turbine. Part 3: Properties of the Tip and Hub Vortices" Renewable Energy 22 (2001): 461-472

29 Massouh F., Dobrev I. "Exploration of the Vortex Wake Behind of Wind Turbine Rotor" Journal of Physics: Conference Series 75 (2007): 1-9

30 Papaconstantinou A., Bergeles G. "Hot-Wire Measurements of the Flowfield in the Vicinity of a HAWG Rotor" Journal of Wind Engineering and Industrial Aerodynamics 31 (1988): 133-146

31 Helmis C.G., Papadopoulos K.H., Asimakopoulos D.N., Papageorgas P.G., Soilemes A.T. "An Experimental Study of the Near-Wake Structure of a Wind Turbine Operating Over Complex Terrain" Solar Energy 54 (1995): 413-428

32 Papadopoulos K.H., Helmis C.G., Soilemes A.T., Papageorgas P.G., Asimakopoulos D.N. "Study of the Turbulent Characteristics of the Near-Wake Field of a Medium-Sized Wind Turbine Operating in High Wind Conditions" Solar Energy 55 (1995): 61-72

33 Connell J.R. "The Spectrum of Wind Speed Fluctuations Encountered By a Rotating Blade of a Wind Energy Conversion System" Solar Energy 29 (1982): 363-375

34 Chamorro L.P., Porté-Agel F. "A Wind-Tunnel Investigation of Wind-Turbine Wakes: Boundary-Layer Turbulence Effects" Boundary-layer Meteorology 132 (2009): 129-149

35 Pope S.B. *Turbulent Flows.* Cambridge: Cambridge University Press, 2000

36 Mydlarski L. "Kolmogorov Hypotheses" Fundamentals of Turbulent Flow: Personal Notes (2008): 114-120

37 Crespo A., Hernández J., Fraga E., Andreu C. "Experimental Validation of the UPM Computer Code to Calculate Wind Turbine Wakes and Comparison With Other Models" Journal of Wind Engineering and Industrial Aerodynamics 27 (1988): 77-88

38 Leclerc C., Masson C., Parachiovoiu I. "Performance and Wake Predictions of HAWTS in Wind Farms" *WindPower '97: Annual Conference and Exhibition of the American Wind Energy Association.* 77-86

39 El Kasmi A., Masson C. "An Extended *k-ε* Model For Turbulent Flow Through Horizontal-Axis Wind Turbines" Journal of Wind Engineering and Industrial Aerodynamics 98 (2008): 103-122

40 Gómez-Elvira R., Crespo A., Migoya E., Manuel F., Hernández J. "Anisotropy of Turbulence in Wind Turbine Wakes" Journal of Wind Engineering and Industrial Aerodynamics 95 (2005): 797-814

41 Jimenez A., Crespo A., Migoya A., Garcia J. "Advances in Large-Eddy Simulation of a Wind Turbine Wake" Journal of Physics: Conference Series 75 (2007): 1-13

42 Hu D., Du Z. "Near Wake of a Model Horizontal Axis Wind Turbine" Journal of Hydrodynamics 21 (2009): 285-291

43 Sicot C., Devinant P., Laverne T., Loyer S., Hureau J. "Experimental Study of the Effects of Turbulence on Horizontal Axis Wind Turbine Aerodynamics" Wind Energy 11 (2008): 245-264

44 Piggott H. "Carving Wooden Blades" Scoraig Wind Electric. 15 Oct. 2004. Accessed 25 Jul. 2008. < http://www.scoraigwind.com/selfblade/index.htm>

45 Adrian R.J. "Particle-Imaging Techniques for Experimental Fluid Mechanics" Annual Review Fluid Mechanics 23 (1991): 261-304

46 Smith G.H., Grant I., Liu A., Infield D.G. "Diagnostics of Wind-Turbine Aerodynamics by Particle Image Velocimetry" *Wind Energy Conversion 1990: Proceedings of the 12th BWEA Conference, Norwich, March 1990.* Eds. Trevor Davies, Jim Halliday and J. Palutikof. London: 1990, 259-64.

47 Dobrev I., Maalouf B., Troldborg N., Massouh F. "Investigation of the Wind Turbine Vortex Structure" *14th International Symposium on Applications of Laser Techniques to Fluid Mechanics, Lisbon, July 2008*

48 Siddiqui K., Nabavi M. "Measurement of the Acoustic Velocity Characteristics in a Standing-Wave Tube Using Out of Phase PIV" Flow Measurement and Instrumentation 19 (2008): 364-369

49 Ramasamy M., Leishman J.G. "Benchmarking Particle Image Velocimetry With Laser Doppler Velocimetry for Rotor Wake Measurements" *24th Applied Aerodynamics Conference, San Francisco, June 2006*

50 Kadem L. "Particle Image Velocimetry for Fluid Dynamics Measurements" Particle Image Velocimetry. 15 Feb. 2008. Accessed 1 Dec. 2009. <http://users.encs.concordia.ca/~kadem/MECH691X/PIV.pdf>

51 Shaikh N. "An Experimental Investigation Of Near Surface Flow Structure Over Wind-Sheared Water Surface" Thesis. Concordia University, 2008

52 Rasouli A., Hangan H., Siddiqui S. "PIV Measurements for a Complex Topographic Terrain" Journal of Wind Engineering and Industrial Aerodynamics 97 (2009): 242-254

53 Siddiqui K.M.H., Loewen M.R., Richardson C., Asher W.E., Jessup A.T. "Simultaneous Particle Image Velcocimetry and Infrared Imagery of Microscale Breaking Waves" Physics of Fluids 13 (2001): 1891-1903

54 Cowen E.A., Monismith S.G. "A Hybrid Digital Particle Tracking Velocimetry Technique" Experiments in Fluids 22 (1997): 199-211

55 Prasad A.K., Adrian R.J., Landreth C.C., Offutt P.W. "Effect of Resolution on the Speed and Accuracy of Particle Image Velocimetry Interrogation" Experiments in Fluids 13 (1992): 105-116.

56 Snel H. "Review of Aerodynamics for Wind Turbines" Wind Energy 6 (2003): 203-211

57 Swift-Hook D.T., Højstrup J. "Nibe Wake Measurements Project In Denmark" *European Wind Energy Conference*, *Hamburg, October 1984*.

58 Ainslie J.F. "Calculating The Flowfield In The Wake of Wind Turbines" Journal of Wind Engineering and Industrial Aerodynamics 27 (1988): 213-224

59 Medici D., Alfredsson P.H. "Measurements on a Wind Turbine Wake: 3D Effects and Bluff Body Vortex Shedding" Wind Energy 9 (2006): 219-236

60 Hasegawa Y., Kikuyama K., Imamura H. "Application of Panel Method To Flow Around Horizontal Axis Wind Turbines" ASME: Numerical Simulations in Turbomachinery 227 (1995): 59-65

61 Palau-Salvador G., Stoesser T., Fröhlich J., Kappler M., Rodi W. "Large Eddy Simulations and Experiments of Flow Around Finite-Height Cylinders" Flow, Turbulence and Combustion 84 (2010): 239-275

62 Crespo A., Hernandez J. "Turbulence Characteristics in Wind Turbine Wakes" Journal of Wind Engineering and Industrial Aerodynamics 61 (1996): 71-85

63 Crespo A., Hernandez J. "Analytical Correlations For Turbulence Characteristics in the Wakes of Wind Turbines" *European Community Wind Energy Conference, 1993. Lubeck-Travemunde, Germany: 436-439*

64 Sanderse B. *Aerodynamics of Wind Turbine Wakes: Literature Review.* ECN Report 09-016 (2009)

65 van den Berg G.P. "Effects of the Wind Profile at Night on Wind Turbine Sound" Journal of Sound and Vibration 277 (2004): 955-970

Appendix A: Error Analysis of PIV Velocity Measurements

According to Cowen and Monismith [54], the total error in the PIV measurements is the sum of errors attributed to particle diameter, seeding density, out of plane motions, gradients, dynamic range, peak locking, and Adaptive Gaussian Window (AGW) interpolation. In the present study, the non-dimensionalized particle diameter for measurements at heights of 0.185 m, 0.135 m and 0.05 m are 0.01, 0.0092, and 0.0083 pixels per pixel, respectively. As particle diameters less than 1 pixel always occupy 1 full pixel area, two issues surface. Firstly, the exact location of a particle less than 1 pixel in diameter cannot be resolved. Secondly, the problem of peak locking increases, which is when the sub-pixel determination of the correlation peak location is rounded to the nearest integer. The latter can be minimized by using a three point Gaussian curve fitting scheme on the correlation plan [54].

The results of Cowen and Monismith [54] and Prasad *et al* [55] are used to estimate the total error in the present PIV data. The errors are computed for each of the three heights at a freestream velocity of 4 m/s, using the instantaneous velocity fields obtained after the removal of spurious velocity vectors and the interpolation of the velocity vectors onto the regular grid points. The in-depth procedure to estimate the total error at a height of 0.185 m is given below.

1. The mean and root mean square (rms) values of the velocity gradients in the streamwise and crosswind directions are computed. The largest rms velocity gradient, at all three measurement planes, was $\frac{\partial u}{\partial y}$ with a value of 0.0263 pixels/pixel, which was used to estimate the error.

2. Figure 5 (a) in Cowen and Monismith [54] gives the error for different particle diameters for a velocity gradient of 0.03 pixels/pixel. Since the velocity gradients in the present study are relatively close in magnitude, Figure 5 (a) was judged to be a good approximation. The smallest particle diameter in the plot was 1 pixel, giving an estimated total error, which is the sum of the mean and rms errors, to be,

$$E_u = 0.065\ pixels\ . \qquad \text{A.1}$$

3. In order to determine the errors due to a particle diameter of 0.01 pixels, the results in Figure 13 from Prasad *et al* [55] were used. The plot shows the profile of peak locking error as a function of particle diameter. The error corresponding to a particle diameter of 0.01 pixels was estimated to be 40 percent larger than that from a particle measuring 1 pixel. However, the authors in [55] employed a center of mass peak-fitting scheme, which is most susceptible to peak locking errors. Since the present study utilized the three-point Gaussian estimator scheme, the peak locking error is decreased. Thus, a more reasonable increase of 30 percent in error due to smaller particle diameters was assigned. That is, Eq. A.1 is multiplied by 1.3, giving a new error from particle diameter and velocity gradient as,

$$E_u = 0.0845\ pixels\ . \qquad \text{A.2}$$

4. Out of plane motions was estimated to be on the order of that for the transverse displacement (y-direction). The total displacement in the y-direction is the sum of the mean and standard deviation, given as,

$$\Delta y = \langle \Delta y \rangle + \sigma_{\Delta y} = 1.163\ pixels\ . \qquad \text{A.3}$$

This displacement corresponds to 0.12 mm. Since the laser sheet thickness was approximately 1 mm, errors due to out of plane motion were deemed to be insignificant.

5. The error due to AGW interpolation was obtained from Figure 5 (f) in Cowen and Monismith [54], and the value was 0.08 pixels. Therefore, the total error in the streamwise velocity was estimated from the sum of AGW interpolation error and Eq. A.2,

$$E_u = 0.0845 + 0.08 = 0.1645\ pixels\,. \qquad \text{A.4}$$

Error in the crosswind velocity was assumed to be identical to Eq. A.4, based on the reasoning that the largest velocity gradient would produce errors in both components of velocity. Thus, the error in the velocity magnitude, E_{u+v}, was estimated as,

$$E_{u+v} = \sqrt{2E_u^2} = 0.233\ pixels\,. \qquad \text{A.5}$$

To arrive at the uncertainty in velocity measurements, the value in Eq. A.5 was substituted into Eq. 2.3, then dividing the result with the freestream velocity. This procedure rendered an error of 5 %. Following the same procedure, the uncertainty in the velocity measurements at the heights of 0.135 m and 0.05 m was estimated to be 5.2 % and 6.4 %, respectively.

Appendix B: Computation of Wavenumber Spectrum

In the event of analyzing the energy content, or spectrum, of a random variable it is necessary to understand the parameters involved in its computation. Beginning with a definition of the two-point, one-time autocovariance [35],

$$R_{ij}(\vec{r},t) = \left\langle u_i(\vec{x},t)\; u_j(\vec{x}+\vec{r},t) \right\rangle, \tag{B.1}$$

where $\vec{r}$ is a displacement vector, such that $R_{ij}(0, 0)$ returns the specific Reynolds stress, $-\left\langle u_i u_j \right\rangle$. One should also be reminded that for statistically homogeneous turbulent flows, only relative displacements (given by $\vec{r}$) between two points matter, and not their absolute positions.

Turbulence, in its most correct form, is given a comprehensive explanation why it must be 3-D. From Eq. B.1, the 3-D wavenumber spectrum $\phi_{ij}(\boldsymbol{\kappa})$ and its Fourier Transform pair are expressed as,

$$\left.\begin{aligned} \phi_{ij}(\vec{\kappa}) &= \frac{1}{(2\pi)^3}\int_{-\infty}^{\infty}\int\int\int R_{ij}(\vec{r})e^{-i\vec{r}\cdot\vec{\kappa}}d\vec{r} \qquad \text{B.2} \\ R_{ij}(\vec{r}) &= \int_{-\infty}^{\infty}\int\int\int \phi_{ij}(\vec{\kappa})e^{-i\vec{r}\cdot\vec{\kappa}}d\vec{\kappa} \qquad \text{B.3} \end{aligned}\right\} \text{Fourier transform pair ,}$$

where $\left|\vec{\kappa}\right| = 2\pi/l$, and l being the characteristic length of eddies [8]. $\phi_{ij}(\boldsymbol{\kappa})$ represents the Reynolds stress density and may be viewed as the contribution, per unit volume in wavenumber space, from the Fourier modes, $e^{-i\vec{r}\cdot\vec{\kappa}}$.

Direct measurements of $R_{ij}(\boldsymbol{r})$ in experiments are rare due to instruments' limitations (i.e. difficult to obtain all three components of velocity, simultaneously). Instead, what is generally reported (which is the case in this thesis) are 1-D correlations, $R_{ii}(\mathrm{r_i}, 0)$, where the displacement

length is performed in a straight line. The 1-D spatial spectrum, F_{ii}, is a real and even function, related to R_{ii} by the following Fourier transform [8],

$$\left.\begin{aligned} F_{ii}(\kappa_1) &= \frac{2}{\pi}\int_0^\infty R_{ii}(r_1)\cos(\kappa_1 r_1)dr_1 \\ R_{ii}(r_1) &= \int_0^\infty F_{ii}(\kappa_1)\cos(\kappa_1 r_1)d\kappa_1 \end{aligned}\right\} \text{Fourier transform pair}, \qquad \text{B.4, B.5}$$

with κ_1 related to the frequency spectrum via $\kappa_1 = 2\pi f / \langle U \rangle$.

Recalling that turbulence is inherently 3-D and consisted of a continuous range of scales, 1-D spectra serve only as approximations to 3-D fields because they may suffer from aliasing [35]. However, if the turbulence is isotropic, meaning eddies are unaffected by rotations, then aliasing effects are not as drastic at the smallest scales (high wavenumbers).

B.1: Computing Wavenumber Spectra

The method employs MATLAB to output the wavenumber spectra, depicted in Figure B.1. The procedure begins by loading the turbulent velocities, *u* and *v*, of a particular data set. Within the nested for-loop, a row counter is increased by 1 in the outer loop before proceeding to the inner loop. Inside the second loop, velocities in the first row (which contains 130 vectors) are stored in a temporary variable. Each one is verified to be a real number before being subjected to a conditional statement: a row containing even 1 NaN is collectively ignored causing the loop to skip to the next image pair, while those without move on.

At this juncture, a FFT window size (2^n, a value of 128 utilized here) and overlap (generally ½ FFT window size) are introduced. Also, a data set counter is increased by 1 to keep track of the number of non-NaN rows. Next, the turbulent velocity vector is passed onto Welch's method,

an algorithm that computes the discrete Fourier transform of a signal. Format of the code is written as in Eq. B.6,

$$[F_{ii}(\kappa^*)\ \kappa^*] = \text{pwelch}(u_i, \text{FFT window size, overlap, \# of FFT points, 1}), \quad \text{B.6}$$

where the asterisks in the output vector imply dimensions of frequency. Vector u_i is split into a number of overlapped windows determined by 'FFT window size' and 'overlap', respectively. The last number specifies the sampling rate which at this stage is set to be unity and later corrected to the given wavenumber resolution. The output data are collected using the row counter as placeholders.

When all velocity fields have been sifted through for a particular row, the spectral densities are averaged across the data set. Finally, a conversion process is used to convert the spectral density into proper wavenumbers units,

$$F_{ii}(\kappa) = F_{ii}(\kappa^*)\Delta x / 2\pi \quad \text{B.7}$$

$$\kappa = 2\pi\kappa^* / \Delta x \quad \text{B.8}$$

where Δx is the distance between the two grid points.

B.2: Wavenumber Spectrum Ranges

Three zones or ranges typically cover the assortment of scales described by the wavenumber spectrum. Figure B.2 highlights these regions: the energy containing range, inertial subrange, and the viscous or dissipative subrange. The energy containing range spans the band of wavenumbers where TKE is predominantly produced. Corresponding size of the scales in the energy containing range are in the neighbourhood of the integral scale, L. To the right of the inertial subrange is the viscous subrange, which covers the smallest eddies in the flow (i.e. on the order of the Kolmogorov microscale, η). The dominating process of these scales is the dissipation of TKE; hence their motions are uniquely determined by both ε and v. In between, the

inertial subrange details a group of scales, l, such that $\eta \ll l \ll L$. The statistical motions are uniquely determined by ε (i.e. universally recognized by the -5/3 decay) independent of ν.

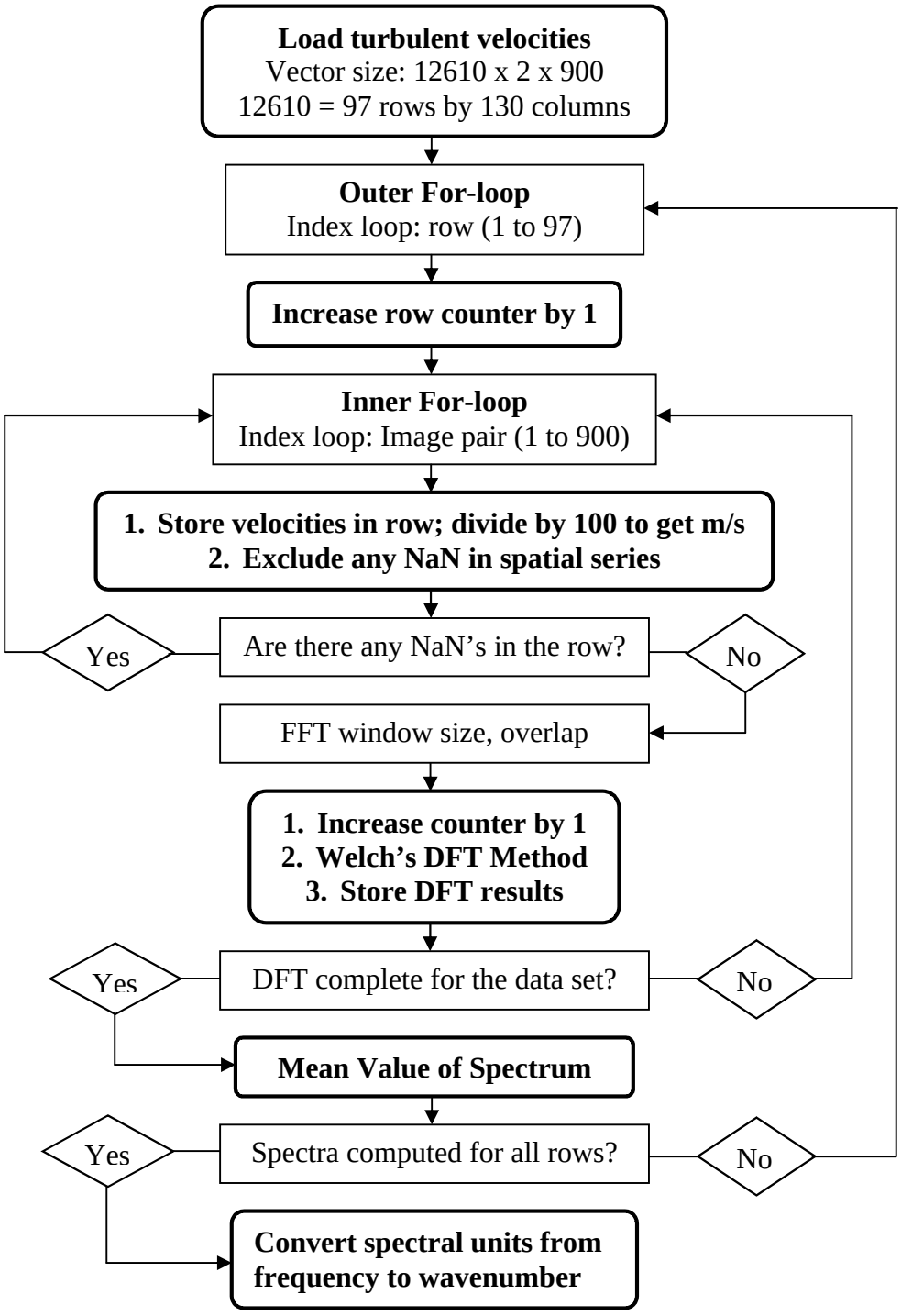

Figure B.1: Flow chart procedure of computing wavenumber spectra in MATLAB

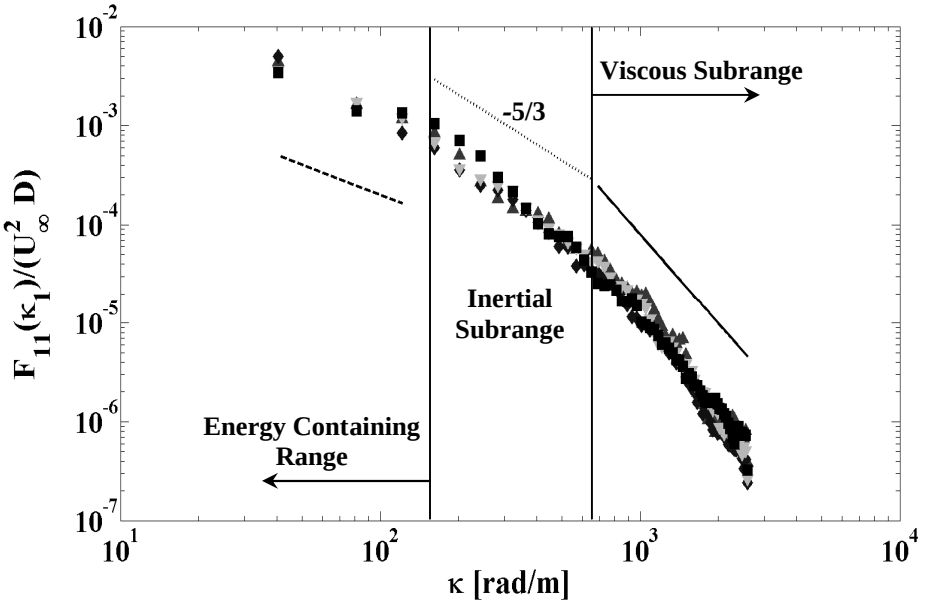

Figure B.2: Various ranges within wavenumber spectrum of the velocity fluctuations.